Norwegian Meteorological Institute

METreport

No. 14/2016
ISSN 2387-4201
Climate

seNorge v2.0, Temperature

An observational gridded dataset of temperature for Norway

Cristian Lussana, Ole Einar Tveito and Francesco Uboldi

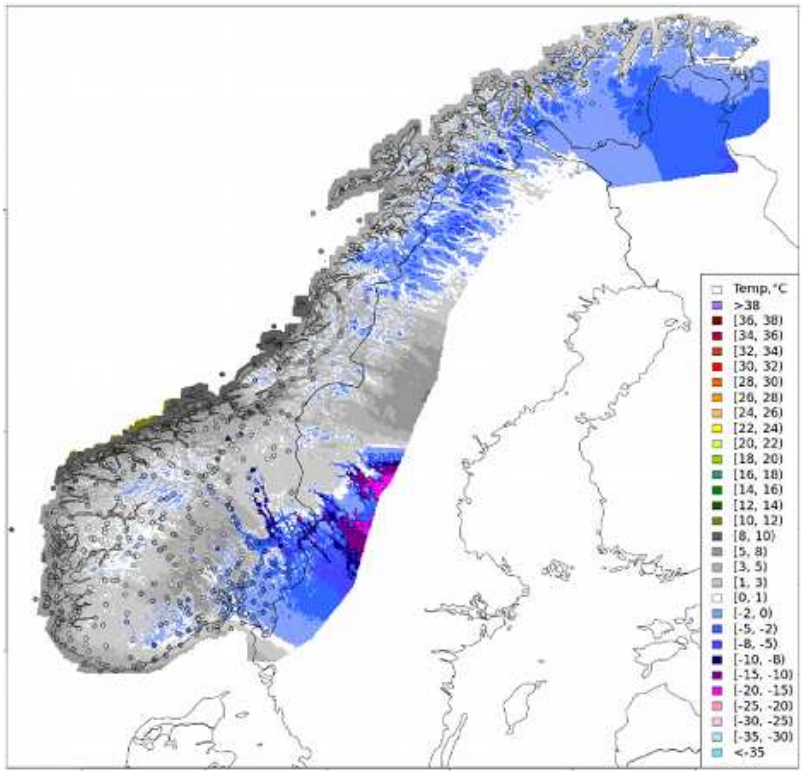

Norwegian Meteorological Institute

METreport

Title	Date
seNorge v2.0: an observational gridded dataset of temperature for Norway	October 21, 2016
Section	**Report no.**
Division for climate services	14/2016
Author(s)	**Classification**
Lussana Cristian, Ole Einar Tveito and Francesco Uboldi	● Free ○ Restricted
Client(s)	**Client's reference**
The Norwegian Water Resources and Energy Directorate	Tuomo Saloranta

Abstract

The seNorge version 2.0 , or *seNorge2*, observational gridded dataset of temperature for the Norwegian mainland has been released by The Norwegian Meteorological Institute. The two main products are: *TEMP1h*, *TEMP1d* for hourly- and daily mean- temperature, respectively. In addition, the experimental dataset of *TEMP1d24h* is available as an alternative product for the daily mean temperature, though for recent years only.

The *seNorge2* products are based on the Norwegian climate database of weather and climate stations. A portion of the data are quality controlled by The Norwegian Meteorological Institute and further tests have been included within the *seNorge2* production procedure. The *TEMP1h* dataset is available from 2010 onwards. The *TEMP1d* dataset is available from 1957 onwards. All the datasets are daily updated and they are available both on a high-resolution grid with $1\,\mathrm{Km}$-resolution and at station locations.

Keywords

observational gridded datasets, temperature, Bayesian spatial interpolation, spatial consistency test

Disciplinary signature	Responsible signature
Hans Olav Hygen	Cecilie Stenersen

Contents

1 Introduction **4**

2 Input data **6**

3 The Statistical Interpolation method **12**

3.1 Optimal Interpolation 14

3.2 The global pseudo-background field estimation 21

3.2.1 Blending of regional Pseudo-background fields 21

3.2.2 The regional pseudo-background field 23

3.3 Diagnostic of the Statistical Interpolation 25

3.3.1 Leave-one-out Cross-Validation (CV) 25

3.3.2 Integral Data Influence (IDI) 25

3.3.3 Maximum-likelihood estimation of the observation-error variance σ_o^2 27

3.4 Spatial Consistency Test 27

4 Test Case: 2015, January 1 **30**

5 Evaluation **46**

5.1 Density plots 48

5.2 Variations of accuracy and precision of the analysis in time 57

5.3 Typical year and seasonal variability 63

5.4 The effects of station density variations in time and space 70

5.5 Analysis increments 75

6 Conclusions **84**

A

Appendix: Examples of regional pseudo-background **87**

1 Introduction

The seNorge version 2.0 collection of observational gridded datasets for temperature and precipitation (in brief, *seNorge2*) has been released by The Norwegian Meteorological Institute (MET Norway) as an improvement of the previous seNorge version 1.1 (*Tveito and Førland*, 1999; *Tveito et al.*, 2000; *Mohr*, 2008).

The new version has been developed in collaboration with The Norwegian Water Resources and Energy Directorate (NVE) within the framework of the *Felles aktiviteter NVE-MET tilknyttet nasjonal flom- og skredvarslingstjeneste*.

The objective of this report is to describe the *seNorge2* two-meter gridded temperature datasets, which are based on the observations from the MET Norway's Climate database (*KlimaDataVareHuset* or KDVH).

The three temperature datasets, or products, developed in *seNorge2* are:

- *TEMP1h*. Hourly Air temperature at time of observation (hourly sampling rate). Input: variable *TA* (i.e. hourly Air temperature at time of observation) in KDVH. Time range: from 2010 to the present day;

- *TEMP1d*. Daily mean temperature in the time period 06-06 UTC. Input: *TAMRR* (i.e. daily mean temperature in the time period 06-06 UTC) in the KDVH. Time range: from 1957 to the present day;

- *TEMP1d24h*. Daily mean temperature as the arithmetic mean of 24 hourly values in the time period 06-06 UTC. Input: *TEMP1h* and *TAMRR*. Time range: from 2010 to the present day.

The observations are interpolated on an high-resolution regular grid. The grid spacing is 1 x 1 Km (in both northing and easting coordinates) and it covers the Norwegian mainland plus an adjacent strip of land along the Norwegian border, including parts of Finland, Sweden and Russia.

The gridded dataset is primarily intended to be used in climatological and hydrological applications. The grid spacing of 1 Km has been chosen as to properly represent the Norwegian drainage network.

The spatial interpolation is based on a Bayesian method. By using Optimal Interpolation (OI; *Gandin and Hardin* (1965)) the observations and the background (i.e. prior

information) are combined into the analysis field, which is made available to the users on grid points and at station locations.

In the case of *TEMP1h* and *TEMP1d*, the statistical interpolation procedure follows a scale-separation approach: the prior information or pseudo-background is estimated from the observations and it is meant to describe the effects of atmospheric dynamics on a coarse scale with a fine scale given by the local observation density as a reference length-scale.

The *TEMP1d24h* product refers to the same quantity as *TEMP1d*. In *TEMP1d* the background field is obtained from *TAMRR* data, whereas in *TEMP1d24h* the background field is obtained by averaging the corresponding 24 *TEMP1h* fields. As a consequence, the *TEMP1d24h* fields are available only from 2010 onwards, while *TEMP1d* data is available back to 1957. *TEMP1d24h* has been included in *seNorge2* to investigate the benefit of using an alternative background in our OI scheme. It is worth remarking that if the 24 *TA* observations are available in KDVH then the corresponding *TAMRR* observation is always present. However, the opposite is not true: for some stations only the daily averaged temperature *TAMRR* is available in KDVH, while the corresponding *TA* observations are not measured. As a result, one should expect significant differences between *TEMP1d24h* and *TEMP1d* fields in the surroundings of those stations where *TAMRR* is available but *TA* has not been measured.

The main products for this *seNorge2* release are: *TEMP1d* for the daily mean temperature and *TEMP1h* for the hourly temperature. In other words, our efforts on the optimization of the spatial interpolation method are aimed at achieving the better quality for these two products, while *TEMP1d24h* will be improved in the future *seNorge2* releases.

The work described in the present document further develop the OI scheme introduced by *Uboldi et al.* (2008). The current application implements that concept over a much wider spatial domain by introducing a global pseudo-background field, which is the blending of several regional pseudo-background fields. In addition, the computation of a single regional pseudo-background field has been modified by including a generalization of the function introduced in *Frei* (2014) to approximate the regional vertical temperature profile.

To prevent from entering the spatial interpolation procedure those observations affected by gross-measurement errors, we must use all the available quality information stored in the *KDVH*. Furthermore, the automatic Spatial Consistency Test described in *Lussana et al.* (2010) is included in the OI procedure.

Section 2 describes the observations used to establish *seNorge2*. In Section 3 the spatial interpolation method is described and in Section 4 its application is presented on a test case. Finally, in Section 5 a detailed evaluation of the datasets is reported.

2 Input data

The input data considered in this study are all the *TA* and *TAMRR* observations available in the MET Norway's Climate database (or KDVH).

The station network comprises manual and automatic weather stations managed by several different public institutions, such as: The Norwegian Meteorological Institute (MET Norway); The Norwegian Water Resources and Energy Directorate (NVE); The Norwegian Public Roads Administration (Statens Vegvesen); the Norwegian Institute of Bioeconomy research (NIBIO); the Swedish Meteorological and Hydrological Institute; the Finnish Meteorological Institute; among others.

The network covers a portion of Fennoscandia, with a focus on the Norwegian mainland. The station distribution is uneven for all the measured parameters with more stations in the Southern part of the domain and a sparser network in the North and in the mountains, as shown in Figs. (2) and (4) for *TA* and *TAMRR*, respectively. The consequences of such inhomogeneities in the station distribution on the statistical interpolation are discussed in Section 3 and evaluated in Section 5.

The data availability in time for *TA* and *TAMRR* is shown in Figs. (1) and (3), respectively. The number of stations is not constant in time, nonetheless the time series for *TAMRR* shows a reasonably stable behavior back to year 1957 with an increase in the number of available stations in recent years. In Figure (1), the evolution in time of the station network measuring *TA* is shown. For each hour from 1957 to 2010, Fig. (1) shows one red point marking the number of available observations. However, for years previous to 2010 it is possible to recognize three distinct "lines": every day at 6 UTC, 12 UTC and 18 UTC (i.e. the timing for the collection of synoptic observations) the number of *TA* observations shows its peaks (the "line" marking the daily maximum value); then for all the other hours of the day, the number of *TA* observations is significantly lower (for some hours of the day *TA* has not been observed until year 1975). After 2010, the three "lines" merge into a single "line", which give us the idea of a more uniform and stable behaviour for the whole *TA* station network.

We've decided to start our production of hourly temperature fields from the 1st of

January 2010.

The availability in time for stations outside Norway is shown in Fig. (5) and it is quite evident that MET started to import these stations in KDVH only for recent years: these stations would play an important role in reducing the border effects along the Norwegian mainland and it is planned to include more stations in future *seNorge2* releases.

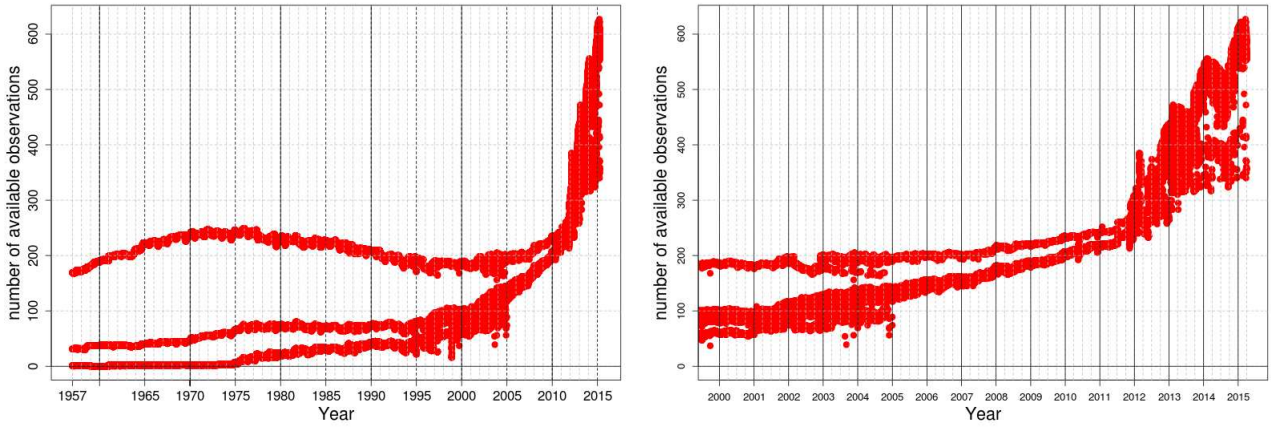

Figure 1: *TA*. Number of available observations *vs* time (1 point=1 hour), for the Norwegian stations. Time interval: (left) 1957-2015; (right) 2000-2015. Note that in the interval from 1957 to approximately 2010 the maximum number of observation is available at: 6 UTC, 12 UTC and 18 UTC.

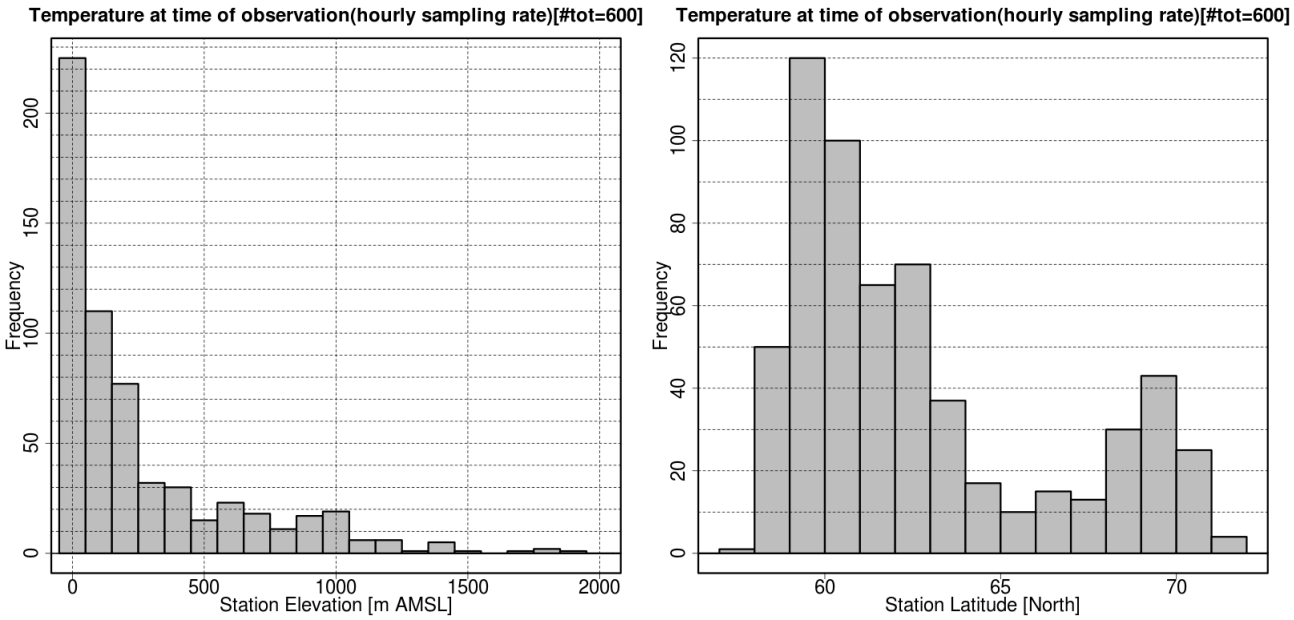

Figure 2: *TA* (status at 2014.11.01). Stations on the Norwegian mainland, distribution of: (left) station elevations; (right) station latitudes.

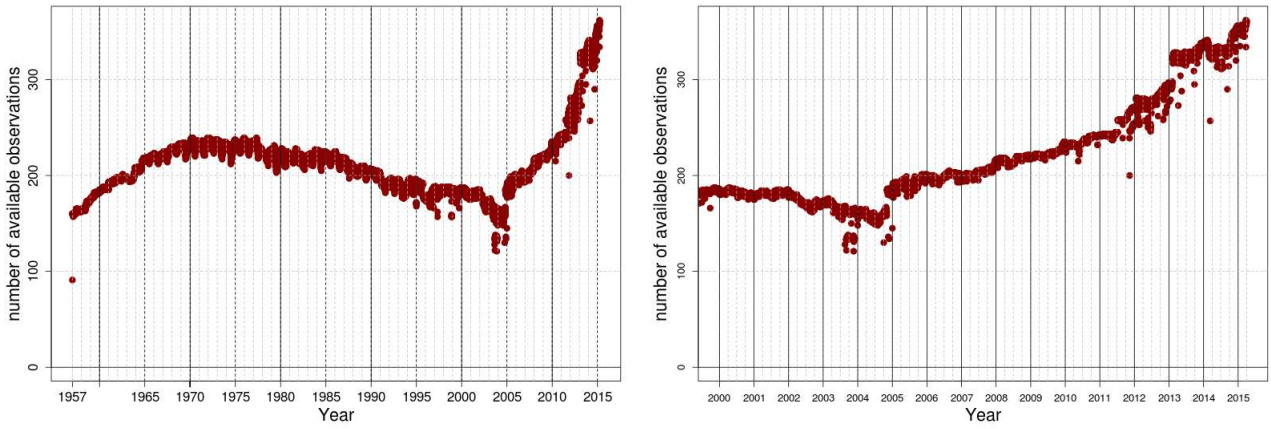

Figure 3: *TAMRR*. number of available observations *vs* time (1 point=1 day), for the Norwegian stations. Time interval: (left) 1957-2015; (right) 2000-2015.

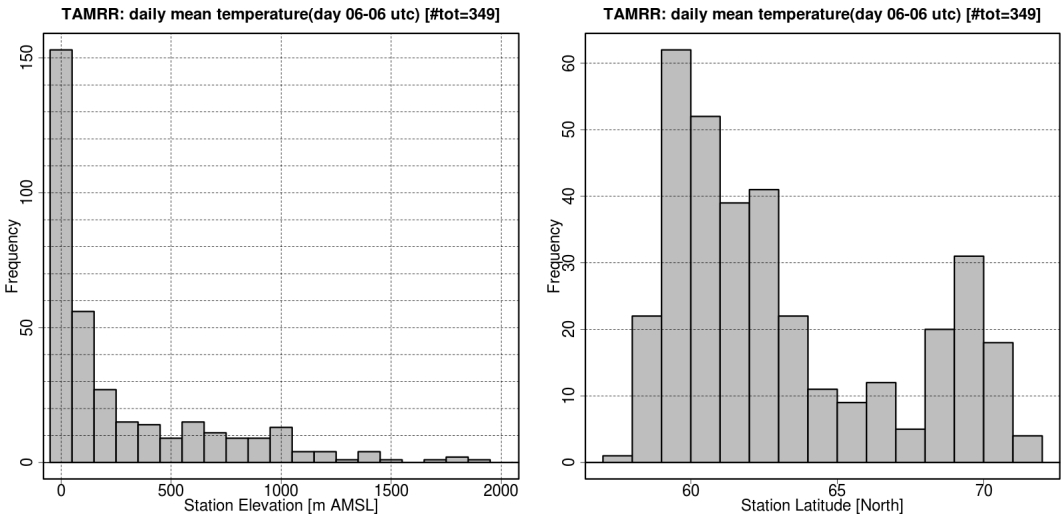

Figure 4: *TAMRR* (status at 2014.11.01). Stations on the Norwegian mainland, distribution of: (left) station elevations; (right) station latitudes.

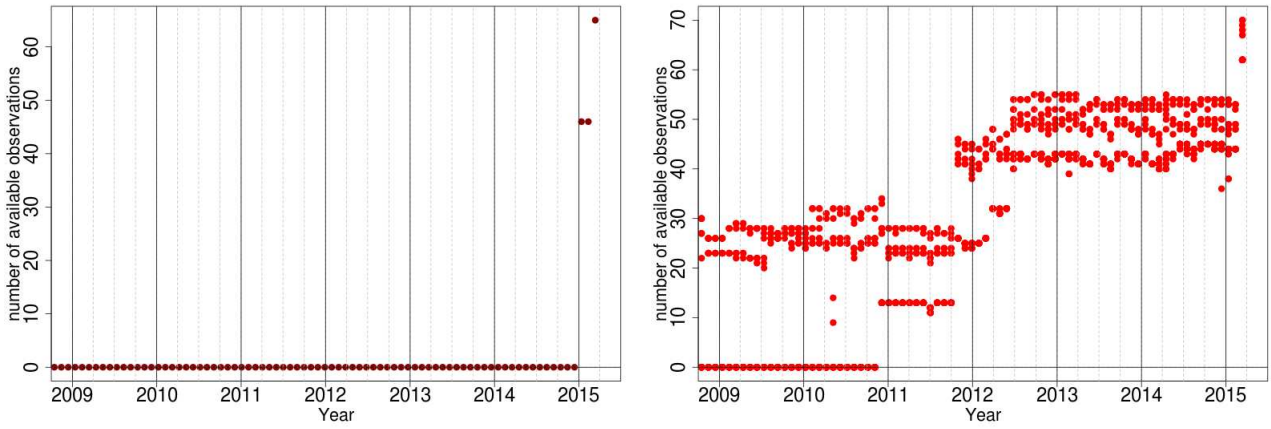

Figure 5: Number of available observations *vs* time for stations outside Norway, for years 2009-2015. Products: (left) *TAMRR*; (right) *TA*.

3 The Statistical Interpolation method

The filtering theory deals with the problem of estimating the unknown true state of the system from noisy observations (see *Jazwinski* (2007) for a review on filtering theory). In our case, the state is the surface (2-meter above the ground) temperature on the regular grid (or at station locations) and the observations are collected by a network of weather stations, as described in Section 2.

The conditional probability density function of the state given the observations is the complete solution of the filtering problem. A so-called Bayesian point of view is adopted here, in that a prior information (background) is taken into account. Because of the probability densities in our assumptions are Gaussian, we are within the linear estimation theory, and the conditional probability density function for the true state is Gaussian too. Note that Gaussian densities are totally characterized by their mean vectors and covariance matrices. As a consequence, the estimate of the true state of the system is the mean vector for the conditional probability density function of the state given the observations and considered the background. In fact, the choice of the best estimate for Gaussian densities is quite easy compared to the non-linear case because the mean, the mode (peak) and median are equivalent, moreover the maximum likelihood (Bayesian) estimate is the same as the minimum variance estimate. In our work, we've used Optimal Interpolation (OI) *Gandin and Hardin* (1965) to obtain the desired mean vector, which in this context is called *analysis* vector.

The OI scheme is described in detail in Section 3.1 and it has been applied for all the products: *TEMP1h*, *TEMP1d* and *TEMP1d24h*, although with some distinctions.

As mentioned in the *Introduction*, in the case of *TEMP1h* and *TEMP1d* our OI scheme differs from the classical OI because the prior distribution (i.e. our background) is estimated from the observations, such as in empirical Bayesian methods. In the following, we will refer to the background for *TEMP1d* and *TEMP1h* as pseudo-background to emphasize its link with the observations. The models chosen to represent the pseudo-background field and its error covariance matrix are both key elements in the determination of the final analysis quality. Two issues related to the introduction of the pseudo-background in our OI scheme need to be discussed. First, as in classical OI formulation we still rely on the assumption that observation and pseudo-background errors are uncorrelated random variables. The validity of this assumption, which is clearly an approximation, is discussed in *Uboldi et al.* (2008) and *Parrish and Derber* (1992). Second, in the calculation of our pseudo-background several parameters need to be estimated (see Section 3.2). Our optimization procedure focus on the determination of their expected values, without considering the associated uncertainties. In other words, the pseudo-background field is implicitly assumed to have always the same quality, although we expect it to constitute a better representation of the actual atmospheric configuration for some cases than in others. As a consequence of the aforementioned two issues, the analysis error covariance matrix derived directly from the classical OI formulation may be regarded as a questionable estimate for the actual analysis error covariance matrix. For this reason, to evaluate the analysis uncertainty several diagnostic variables are introduced in Section 3.3.

In the case of *TEMP1d24h*, the background is obtained by averaging the corresponding 24 *TEMP1h* fields. However, it is possible that some of the *TA* hourly temperature observations used in the *TEMP1h* OI procedure could have been used to obtain the corresponding *TAMRR* value, then also for *TEMP1d24h* the background should not be considered independent from the observations.

The Spatial Consistency Test implemented in the statistical interpolation is described in Section 3.4.

The notation of *Ide et al.* (1997) is used whenever possible. The state vectors $\mathbf{x}$ have dimension n (i.e. number of grid points). The $\mathbf{y}$-vectors at time t_i have dimension p_i (i.e. number of observations or station points or station locations) and, typically, $p_i \ll n$. Matrices are specified through bold upper-case Roman letters (i.e. $\mathbf{K}$ is the Kalman gain matrix). The operator $[\ldots]_j$ will specify the j-th vector component and similarly the

operator $[\ldots]_{ij}$ will specify the matrix components (i-th row, j-th column). A vector will always be a column vector. Superscript T denotes the vector (matrix) transpose. The three dimensional spatial coordinates associated with a generic point in the space $\mathbf{r}$ are specified as triplets (x,y,z). It is implicitly assumed that the i-th grid point has coordinates (x_i,y_i,z_i) and the j-th station point has coordinate $\left(x_j,y_j,z_j\right)$. For station locations, the vertical coordinate z is the real station elevation stored as a metadata in KDVH, while the elevation for grid points is obtained from an high-resolution digital elevation model.

3.1 Optimal Interpolation

Consider the background, i.e. a priori information, available both at the n grid points and at p_i station locations:

$$\mathbf{x}^{\mathrm{b}} = \mathbf{x}^{\mathrm{t}} + \eta^{\mathrm{b}} \tag{1}$$

$$\mathbf{y}^{\mathrm{b}} = \mathbf{y}^{\mathrm{t}} + \varepsilon^{\mathrm{b}} \tag{2}$$

where: $\mathbf{x}^{\mathrm{b}}$ is the background at grid points; $\mathbf{x}^{\mathrm{t}}$ is the unknown true atmospheric state; $\eta^{\mathrm{b}} \sim N(\mathbf{0},\mathbf{B})$ is the background error, which is assumed Gaussian (the mean vector is assumed to be $\mathbf{0}$, that is the background is an unbiased estimate of the true state; $\mathbf{B}$ is the covariance matrix, $[\mathbf{B}]_{ij}$ being the background error covariance between a pair of grid points).

Similarly, $\mathbf{y}^{\mathrm{b}}$ is the background at the station locations; $\mathbf{y}^{\mathrm{t}}$ is the unknown true temperature state at station locations; $\varepsilon^{\mathrm{b}} \sim N(\mathbf{0},\mathbf{S})$ is the background error, which is assumed Gaussian (each component of the $p_i \times p_i$ matrix $\mathbf{S}$ is the background error covariance between a pair of station points).

Let the p_i-vector observations $\mathbf{y}^{\mathrm{o}}$ be given by:

$$\mathbf{y}^{\mathrm{o}} = \mathbf{y}^{\mathrm{t}} + \varepsilon^{\mathrm{o}} \tag{3}$$

where the non-linear observation operator is implicit and $\varepsilon^{\mathrm{o}} \sim N(\mathbf{0},\mathbf{R})$ is the observation error, a p_i-vector, which is assumed Gaussian and its covariance matrix is denoted by $\mathbf{R}$.

The discrete filtering problem consists of computing an estimate $\mathbf{x}^{\mathrm{a}}$ for the true state $\mathbf{x}^{\mathrm{t}}$ based on $\mathbf{y}^{\mathrm{o}}$. The OI scheme assumes a linear relation between the analysis increment $\mathbf{x}^{\mathrm{a}} - \mathbf{x}^{\mathrm{b}}$ and the innovation $\mathbf{y}^{\mathrm{o}} - \mathbf{y}^{\mathrm{b}}$:

$$\mathbf{x}^{\mathrm{a}} = \mathbf{x}^{\mathrm{b}} + \mathbf{K}\left(\mathbf{y}^{\mathrm{o}} - \mathbf{y}^{\mathrm{b}}\right) \tag{4}$$

Where $\mathbf{K}$ is the $n \times p_i$ (suboptimal) gain matrix. Then, by minimizing the variance of the analysis error $\eta^{\mathrm{a}} \equiv \mathbf{x}^{\mathrm{a}} - \mathbf{x}^{\mathrm{t}}$ with the implicit assumption of independence between observation and background errors, the OI expression becomes:

$$\mathbf{x}^{\mathrm{a}} = \mathbf{x}^{\mathrm{b}} + \mathbf{G}\left(\mathbf{S} + \mathbf{R}\right)^{-1}\left(\mathbf{y}^{\mathrm{o}} - \mathbf{y}^{\mathrm{b}}\right) \tag{5}$$

Where the gain matrix $\mathbf{K} = \mathbf{G}\left(\mathbf{S} + \mathbf{R}\right)^{-1}$ is expressed by means of the error covariance matrices:

$$\mathbf{G} = \left\langle \left(\mathbf{x}^{\mathrm{b}} - \mathbf{x}^{\mathrm{t}}\right)\left(\mathbf{y}^{\mathrm{b}} - \mathbf{y}^{\mathrm{t}}\right)^{\mathrm{T}} \right\rangle = \left\langle \eta^{\mathrm{b}}\left(\varepsilon^{\mathrm{b}}\right)^{\mathrm{T}} \right\rangle \tag{6}$$

$$\mathbf{S} = \left\langle \left(\mathbf{y}^{\mathrm{b}} - \mathbf{y}^{\mathrm{t}}\right)\left(\mathbf{y}^{\mathrm{b}} - \mathbf{y}^{\mathrm{t}}\right)^{\mathrm{T}} \right\rangle = \left\langle \varepsilon^{\mathrm{b}}\left(\varepsilon^{\mathrm{b}}\right)^{\mathrm{T}} \right\rangle \tag{7}$$

$$\mathbf{R} = \left\langle \left(\mathbf{y}^{\mathrm{o}} - \mathbf{y}^{\mathrm{t}}\right)\left(\mathbf{y}^{\mathrm{o}} - \mathbf{y}^{\mathrm{t}}\right)^{\mathrm{T}} \right\rangle = \left\langle \varepsilon^{\mathrm{o}}\left(\varepsilon^{\mathrm{o}}\right)^{\mathrm{T}} \right\rangle \tag{8}$$

the angular brackets represent the expectation value with respect to an appropriately defined statistical ensemble. Each component of the $n \times p_i$ matrix $\mathbf{G}$ is the covariance between the background error at a grid point and the background error at a station point. The true state is unknown and so are the covariance matrices. The estimates of these matrices, which are specified by means of analytical correlation functions, determine the characteristics of the analysis field.

The OI analysis on station points is:

$$\mathbf{y}^{\mathrm{a}} = \mathbf{y}^{\mathrm{b}} + \mathbf{W}\left(\mathbf{y}^{\mathrm{o}} - \mathbf{y}^{\mathrm{b}}\right) \tag{9}$$

Where $\mathbf{W}$ is the $p_i \times p_i$ influence matrix. Once again, by minimizing the variance of the analysis error $\varepsilon^{\mathrm{a}} \equiv \mathbf{y}^{\mathrm{a}} - \mathbf{y}^{\mathrm{t}}$, the OI expression becomes:

$$\mathbf{y}^{\mathrm{a}} = \mathbf{y}^{\mathrm{b}} + \mathbf{S}\left(\mathbf{S} + \mathbf{R}\right)^{-1}\left(\mathbf{y}^{\mathrm{o}} - \mathbf{y}^{\mathrm{b}}\right) \tag{10}$$

We assume the observation error covariance matrix $\mathbf{R}$ to be diagonal and all the observation errors have the same variance σ_{o}^2 (it is a quantity characterizing the network globally rather than each single station):

$$\mathbf{R} = \sigma_{\mathrm{o}}^2 \mathbf{I} \tag{11}$$

The function of horizontal and vertical distances that is used to estimate the background error correlation between the two generic points $\mathbf{r}_i = (x_i, y_i, z_i)$ and $\mathbf{r}_j = (x_j, y_j, z_j)$ in the three-dimensional space is:

$$\gamma\left(\mathbf{r}_i, \mathbf{r}_j; D^h, D^z\right) = \exp\left\{ -\frac{1}{2}\left[\left(\frac{d\left(\mathbf{r}_i, \mathbf{r}_j\right)}{D^h} \right)^2 + \left(\frac{\Delta z\left(\mathbf{r}_i, \mathbf{r}_j\right)}{D^z} \right)^2 \right] \right\} \tag{12}$$

Where $d\left(\mathbf{r}_i, \mathbf{r}_j\right)$ is the horizontal distance between the two points, and $\Delta z\left(\mathbf{r}_i, \mathbf{r}_j\right)$ is the difference between their elevations above sea level. D^h and D^z are the de-correlation distances in the horizontal and vertical directions, respectively.

The effect of different choices of D^h and D^z in defining the values of the station-gridpoint correlations (see Eq. (12)) is shown in Figs. (6)-(8) for 3 stations.

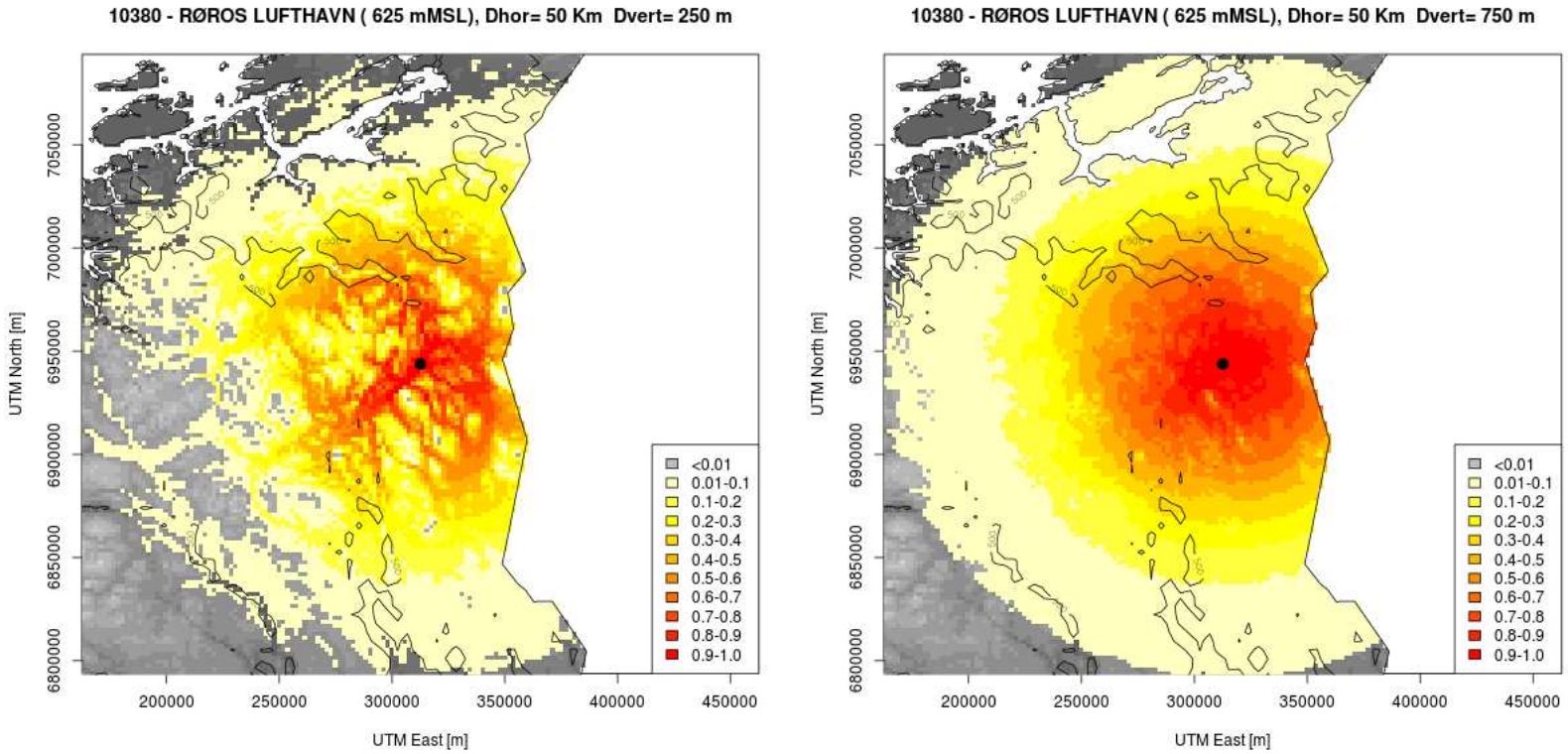

Figure 6: Station-gridpoints correlation values for station 10380. Left panel: $D^h = 50\,\text{Km}$ and $D^z = 250\,\text{m}$. Right panel: $D^h = 50\,\text{Km}$ and $D^z = 750\,\text{m}$.

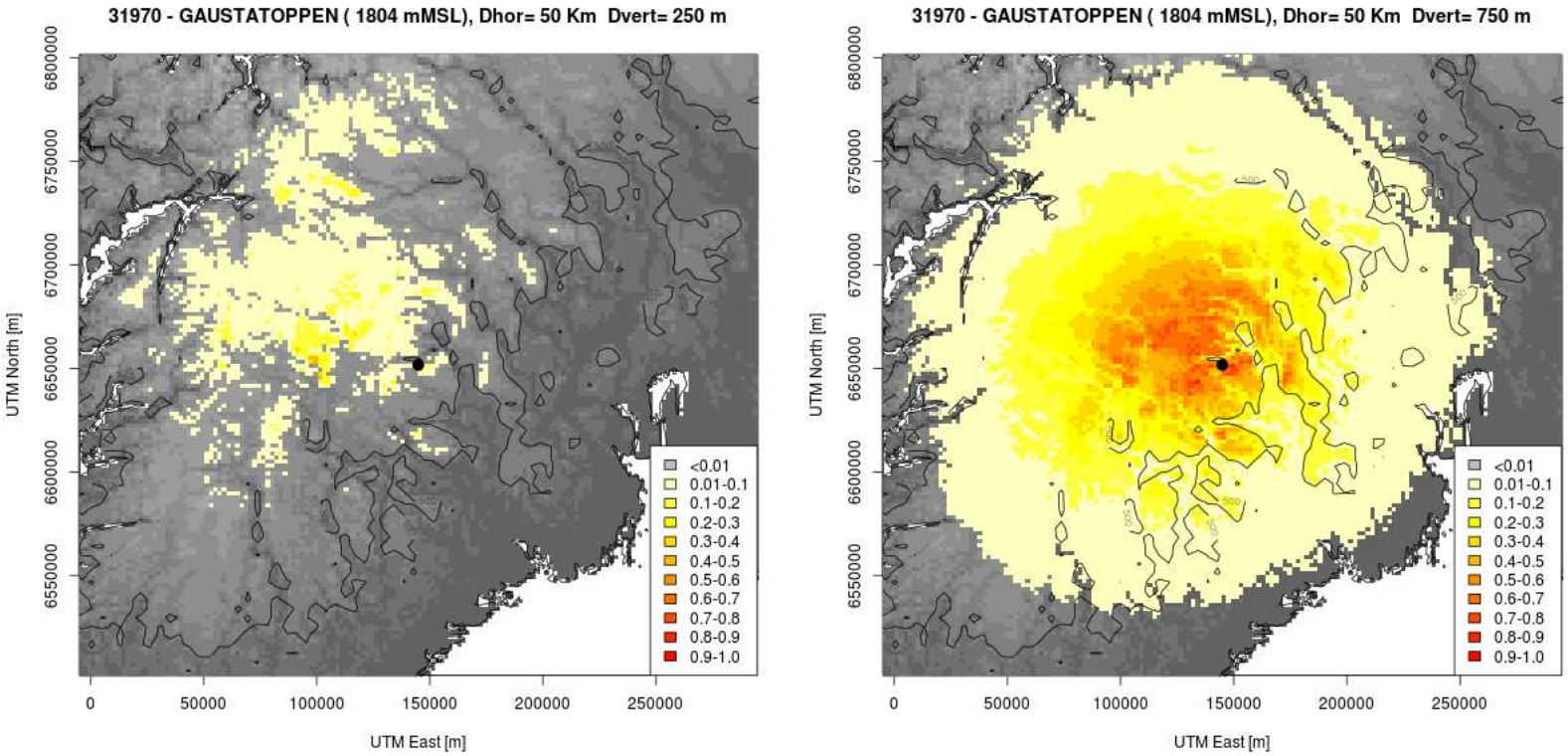

Figure 7: Station-gridpoints correlation values for station 31970. Left panel: $D^h = 50\,\text{Km}$ and $D^z = 250\,\text{m}$. Right panel: $D^h = 50\,\text{Km}$ and $D^z = 750\,\text{m}$.

If the background error variance σ_b^2 is assumed to be uniform, then the background error correlation matrices $\tilde{\mathbf{G}}$ and $\tilde{\mathbf{S}}$ can be written as $\mathbf{G} \equiv \sigma_b^2 \tilde{\mathbf{G}}$ and $\mathbf{S} \equiv \sigma_b^2 \tilde{\mathbf{S}}$. The analysis on the grid points is then obtained from Eq. (5) as:

$$\mathbf{x}^a = \mathbf{x}^b + \tilde{\mathbf{G}} \left(\tilde{\mathbf{S}} + \varepsilon^2 \mathbf{I} \right)^{-1} \left(\mathbf{y}^o - \mathbf{y}^b \right) \tag{13}$$

Where the scalar $\varepsilon^2 \equiv \sigma_o^2 / \sigma_b^2$ is the ratio between the background and the observation error variances. In this way the components of the gain matrix, $\mathbf{K} = \tilde{\mathbf{G}} \left(\tilde{\mathbf{S}} + \varepsilon^2 \mathbf{I} \right)^{-1}$, only depend on the three parameters: D^h, D^z, and ε^2.

From the definition of ε^2, it is clear that $\varepsilon^2 = 0$ implies assuming perfect observations, hence exact interpolation. On the other hand, setting $\varepsilon^2 > 1$ implies a greater confidence in the background field rather than in the observations.

The OI analysis on station points is obtained from Eq. (10):

$$\mathbf{y}^a = \mathbf{y}^b + \tilde{\mathbf{S}} \left(\tilde{\mathbf{S}} + \varepsilon^2 \mathbf{I} \right)^{-1} \left(\mathbf{y}^o - \mathbf{y}^b \right) \tag{14}$$

OI parameter values. In the remaining of this Section, our choices for the OI parameter are described.

For the three products *TEMP1h*, *TEMP1d* and *TEMP1d24h*, the values of the OI parameters are exactly the same:

- $D^h = 60\,\mathrm{Km}$
- $D^z = 600\,\mathrm{m}$
- $\varepsilon^2 \equiv \sigma_o^2 / \sigma_b^2 = 0.5$

Furthermore, these values are fixed for the entire time period. The main motivation for using the same values for all the three variables and for keeping fixed values in time, is that an important application of *seNorge2* products would be the derivation of temporal trends for temperature -and its derived indexes- and the inter-comparison of these trends across Norway. As a matter of fact, our choice would simplify the inter-comparison of the analysis results in time and space, and even between the different products, because the presence of any difference in the temperature statistics in time and/or space should be attributed either to the climate or to a significant variation in the MET Norway's observational network but it can't be the result of a variation in the OI configuration.

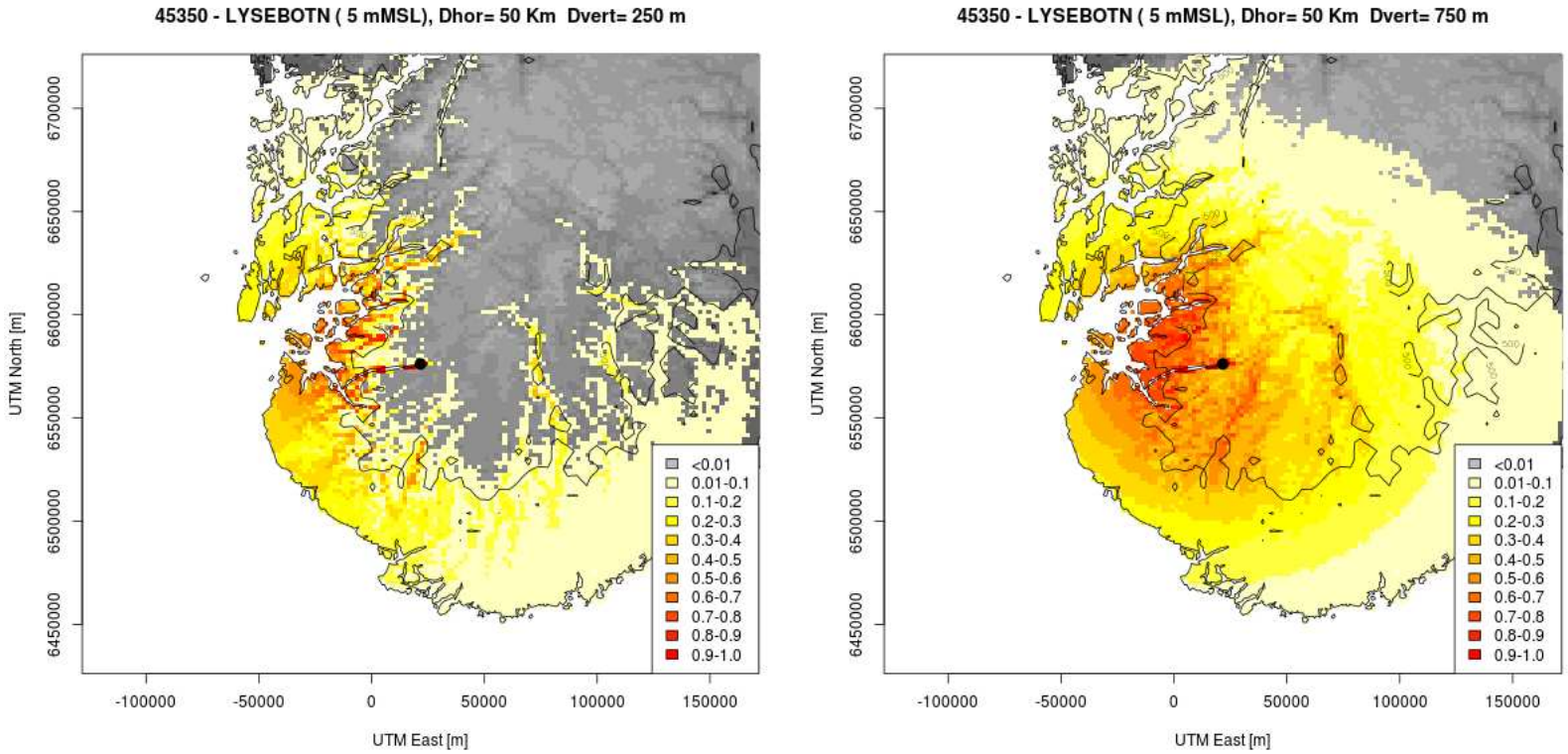

Figure 8: Station-gridpoints correlation values for station 45350. Left panel: $D^h = 50\,\text{Km}$ and $D^z = 250\,\text{m}$. Right panel: $D^h = 50\,\text{Km}$ and $D^z = 750\,\text{m}$.

In practice, the OI parameter values have been chosen by running the spatial interpolation procedure with a reasonable selection of: D^h, D^z and ε^2 values. The heuristic procedure adopted has been aimed at achieving an OI configuration resulting in a reasonable quality of the final products: our OI should correct the background values by means of the available observations for most of the grid points even when and where the station network is sparse, such that possible inhomogeneities existing in the data distribution only marginally affects the OI filter.

The drawback of this choice is that we limit the levels of accuracy and precision potentially achievable for the analysis for those cases in which a dense station network is available.

The impact on the analysis quality of our choices for the OI parameters is discussed in Section 5.

3.2 The global pseudo-background field estimation

The global (i.e. valid for the whole domain) large-scale trend, which is used in the statistical interpolation of *TEMP1d* and *TEMP1h*, is obtained by blending several regional trends through a weighted mean.

In fact, abrupt variations in the global blended pseudo-background field are avoided, or at least strongly attenuated, by means of weights based on the Integral Data Influence concept (IDI, see Section 3.3).

The main idea is that the spatial domain is divided in several overlapping sub-domains; each of them ranging from a few tens to a few hundreds of kilometers in both zonal and meridional directions. In our interpolation scheme, the temperature field is regarded as a composition of coarse scale and fine scale effects within a so-called scale-separation approach. The local station density plays a key role in the distinction between coarse and fine scales. The pseudo-background field is meant to describe the temperature spatial trend due to the coarse scale effects.

In this Section, the computational steps involved in the procedure are described in detail. In Section 4 an example is presented.

3.2.1 Blending of regional Pseudo-background fields

1. The spatial domain is divided in D overlapping sub-domains (or regions), each containing approximately 10% of the available stations and having an extension

dependent on the station density (i.e. sparse observation areas will result in larger sub-domains). The maximum number of stations included in a sub-domain is set to 50. The minimum number of stations allowed to define a sub-domain is set to 5. A single station may be part of more than one sub-domain. The sub-domain extension has a predefined limit: the distance between each station and a reference station located at the center of the sub-domain must be less than 200 Km. Let Y_d be the set of stations included in the d-th sub-domain, then the associated regional pseudo-background field is obtained as described in 3.2.2. The corresponding IDI-vector $\mathbf{x}^{Y_d,\mathrm{IDI}}$ is computed as in Eq. (20) for all of the n grid points (both inside and outside the d-th sub-domain). The parameter values used to compute $\mathbf{x}^{Y_d,\mathrm{IDI}}$ are: $D^h = 70\mathrm{Km}$; $D^z = 1000\mathrm{m}$; $\varepsilon^2 = 0.5$.

2. For the Norwegian mainland, an ensemble of D pseudo-background fields $\left\{\mathbf{x}_d^{\mathrm{b}}\right\}_{d=1,\ldots,D}$ together with a set of pseudo-background values at station locations $\left\{\mathbf{y}_d^{\mathrm{b}}\right\}_{d=1,\ldots,D}$ are computed. The generic $\mathbf{x}_d^{\mathrm{b}}$ is an n-vector and $\mathbf{y}_d^{\mathrm{b}}$ is a p_i-vector, both are obtained using only the observations collected by stations included in Y_d. Elaboration over different sub-domains are performed independently.

3. The final pseudo-background field $\mathbf{x}^{\mathrm{b}}$ is a linear combination of the D pseudo-background fields weighted by the corresponding IDI fields, thus its i-th component $\left[\mathbf{x}^{\mathrm{b}}\right]_i$ is given by:

$$\left[\mathbf{x}^{\mathrm{b}}\right]_i = \frac{\sum_{d=1}^{D}\left[\mathbf{x}_d^{\mathrm{b}}\left(\mathbf{x}^{Y_d,\mathrm{IDI}}\right)^{\mathrm{T}}\right]_{ii}}{\sum_{d=1}^{D}\left[\mathbf{x}^{Y_d,\mathrm{IDI}}\right]_i} \tag{15}$$

Analogously, the j-th component of the final pseudo-background vector $\left[\mathbf{y}^{\mathrm{b}}\right]_j$ is:

$$\left[\mathbf{y}^{\mathrm{b}}\right]_j = \frac{\sum_{d=1}^{D}\left[\mathbf{y}_d^{\mathrm{b}}\left(\mathbf{y}^{Y_d,\mathrm{IDI}}\right)^{\mathrm{T}}\right]_{jj}}{\sum_{d=1}^{D}\left[\mathbf{y}^{Y_d,\mathrm{IDI}}\right]_j} \tag{16}$$

Suppose the i-th grid point is far away from all the stations Y_d defining the d-th sub-domain, then $\left[\mathbf{x}^{Y_d,\mathrm{IDI}}\right]_i$ shall be close to zero and the d-th pseudo-background field will have a very low influence on the final $\left[\mathbf{x}^{\mathrm{b}}\right]_i$ value, as desired. On the other hand, if the i-th grid point is in the middle of an overlapping area between several sub-domains then the IDI-weighted mean would generate a smooth transition between neighboring local trends, depending on the station distribution.

3.2.2 The regional pseudo-background field

Consider the generic d-th sub-domain (or region), the trend is determined by fitting a parametric function of the spatial coordinates to the set of observations Y_d making up the d-th sub-domain. Three different parametric functions are considered as plausible pseudo-background models, thus three possible pseudo-background p_i-vectors are obtained: $\mathbf{y}_d^{\mathrm{b}0}$, $\mathbf{y}_d^{\mathrm{b}1}$ and $\mathbf{y}_d^{\mathrm{b}2}$. The best estimate should have the property of producing small errors, then the pseudo-background model which minimizes the root mean square error (i.e. best fitting the observations belonging to Y_d) is chosen to generate the pseudo-background field associated with the d-th sub-domain, $\mathbf{x}_d^{\mathrm{b}}$, given the grid points coordinates and elevations.

The three parametric functions of the spatial coordinates used as plausible pseudo-background models are:

- $\mathbf{y}_d^{\mathrm{b}0}$. Linear parametric function of the spatial coordinates:

$$\left[\mathbf{y}_d^{\mathrm{b}0}\right]_j = T_{const} + \alpha\left(x_j - \bar{x}\right) + \beta\left(y_j - \bar{y}\right) + \gamma z_j$$

  Where the parameters: T_{const}, α, β and γ are computed by using a least-square based minimization procedure; $\bar{x}$ and $\bar{y}$ are the arithmetic means of x and y spatial coordinates considering only stations in Y_d.

  Constraints:

  - $|\alpha| < 8 \cdot 10^{-5}\,^{\circ}\mathrm{C/m} = 8\,^{\circ}\mathrm{C}/100\mathrm{Km}$ and $|\beta| < 8 \cdot 10^{-5}\,^{\circ}\mathrm{C/m}$
  - $-0.008^{\circ}\mathrm{C/m} \leq \gamma \leq -0.001^{\circ}\mathrm{C/m}$, the default value is $\gamma = -0.006^{\circ}\mathrm{C/m}$

- $\mathbf{y}_d^{\mathrm{b}1}$. The background value at the j-th station location is obtained by the composition of two distinct linear regressions, thus allowing for a ground-based temperature inversion in the vertical at elevation z_{inv} (*Uboldi et al.* (2008)):

$$\left[\mathbf{y}_d^{\mathrm{b}1}\right]_j = \begin{cases} y^{\mathrm{above}} \equiv T_{inv} + \alpha_a\left(x_j - \bar{x}\right) + \beta_a\left(y_j - \bar{y}\right) + \gamma_a\left(z_j - z_{inv}\right) & , z_j > (z_{inv} + \Delta z) \\ \left\{y^{\mathrm{above}}\left[z_j - (z_{inv} - \Delta z)\right] + y^{\mathrm{below}}\left[(z_{inv} + \Delta z) - z_j\right]\right\} / (2\Delta z) & , (z_{inv} - \Delta z) < z_j \leq (z_{inv} + \Delta z) \\ y^{\mathrm{below}} \equiv T_{inv} + \alpha_b\left(x_j - \bar{x}\right) + \beta_b\left(y_j - \bar{y}\right) + \gamma_b\left(z_j - z_{inv}\right) & , z_j \leq (z_{inv} - \Delta z) \end{cases}$$

  Where the parameters: T_{inv} (temperature at elevation z_{inv}), z_{inv}, α_a, β_a, γ_a, α_b, β_b, γ_b and Δz, are computed by using a least-square based minimization procedure; $\bar{x}$ and $\bar{y}$ are the arithmetic means of x and y spatial coordinates considering only stations in Y_d.

  Constraints:

- $\text{quantile}_{0.20}\left\{z_j\right\}_{j\in Y_d} \leq z_{inv} \leq \text{quantile}_{0.80}\left\{z_j\right\}_{j\in Y_d}$
- $|\alpha_a| \leq 0.00008\,^\circ\text{C/m}$ $(8\,^\circ\text{C/100km})$ and $|\alpha_b| \leq 0.00008\,^\circ\text{C/m}$ $(8\,^\circ\text{C/100km})$
- $-0.012\,^\circ\text{C/m} \leq \gamma_a \leq -0.0001\,^\circ\text{C/m}$ and $-0.012\,^\circ\text{C/m} \leq \gamma_b \leq 0.010\,^\circ\text{C/m}$
- $40\text{m} \leq \Delta z \leq 60\text{m}$

- $\mathbf{y}_d^{\text{b2}}$. The background value at the j-th station location is obtained also in this case by the composition of two distinct regressions, allowing for a temperature inversion (ground-based or not) in the vertical between elevation h_0 and h_1 (as described in *Frei* (2014), with the inclusion of x and y dependency):

$$\left[\mathbf{y}_d^{\text{b2}}\right]_j = \begin{cases} T_0 + \alpha_a\left(x_j-\bar{x}\right) + \beta_a\left(y_j-\bar{y}\right) + \gamma z_j & ,z_j \geq h_1 \\ T_0 + \gamma z_j - \frac{a}{2}\left[1+\cos\left(\pi\frac{z_j-h_0}{h_1-h_0}\right)\right] + \dots & \\ \left[\alpha_a\left(x_j-\bar{x}\right) + \beta_a\left(y_j-\bar{y}\right)\right]\frac{z_j-h_0}{h_1-h_0} + \left[\alpha_b\left(x_j-\bar{x}\right) + \beta_b\left(y_j-\bar{y}\right)\right]\frac{h_1-z_j}{h_1-h_0} & ,h_0 < z_j < h_1 \\ T_0 + \alpha_b\left(x_j-\bar{x}\right) + \beta_b\left(y_j-\bar{y}\right) + \gamma z_j - a & ,z_j \leq h_0 \end{cases}$$

  Where the parameters: T_0 (temperature at $z=0$), h_0, h_1, α_a, β_a, α_b, β_b, γ and a (the two sections, above h_1 and below h_0, are shifted against each other by a temperature contrast a), are computed by using a least-square based minimization procedure; $\bar{x}$ and $\bar{y}$ are the arithmetic means of x and y spatial coordinates considering only stations in Y_d.

  Constraints:

  - $\text{quantile}_{0.20}\left\{z_j\right\}_{j\in Y_d} \leq h_0 \leq \text{quantile}_{0.80}\left\{z_j\right\}_{j\in Y_d}$
  - $|\alpha_a| \leq 0.00008\,^\circ\text{C/m}$ $(8\,^\circ\text{C/100km})$ and $|\alpha_b| \leq 0.00008\,^\circ\text{C/m}$ $(8\,^\circ\text{C/100km})$
  - $-0.012\,^\circ\text{C/m} \leq \gamma \leq -0.0001\,^\circ\text{C/m}$
  - $50\text{m} \leq (h_1 - h_0) \leq 300\text{m}$
  - $-10\,^\circ\text{C} \leq a \leq 10\,^\circ\text{C}$

  In addition to the previous conditions, $\mathbf{y}_d^{\text{b1}}$ and $\mathbf{y}_d^{\text{b2}}$ are considered only if:

- the number of observations in the d-th sub-domain is not less than 20.
- $\text{quantile}_{0.90}\left\{z_j\right\}_{j\in Y_d} - \text{quantile}_{0.10}\left\{z_j\right\}_{j\in Y_d} \geq 50\,\text{m}$

These two further constraints are imposed so to achieve a robust (i.e. stable with respect to outliers) procedure in the calculation of complex vertical profile of temperature. If these two conditions are not simultaneously valid then $\mathbf{y}_d^{\text{b0}}$ is the only admissible solution.

3.3 Diagnostic of the Statistical Interpolation

3.3.1 Leave-one-out Cross-Validation (CV)

Given the j-th station, the corresponding leave-one-out Cross-Validated (CV) analysis $[\check{\mathbf{y}}^{\mathrm{a}}]_j$ is defined as the analysis estimate obtained for the j-th observation by using all the other observations, but without using the j-th observation itself. The CV analysis can be written as (*Uboldi et al.* (2008)):

$$[\check{\mathbf{y}}^{\mathrm{a}}]_j = [\mathbf{y}^{\mathrm{o}}]_j + \frac{1}{1-[\mathbf{W}]_{jj}} \left([\mathbf{y}^{\mathrm{a}}]_j - [\mathbf{y}^{\mathrm{o}}]_j \right) \tag{17}$$

The CV analysis vector $\check{\mathbf{y}}^{\mathrm{a}}$ is the p_i-vector having the CV analysis as components.

Fixed a time-stamp, The CV-score is defined as the root mean squared difference:

$$CV_{\mathrm{score}} = \sqrt{\frac{1}{p_i} \sum_{j=1}^{p_i} \left([\check{\mathbf{y}}^{\mathrm{a}}]_j - [\mathbf{y}^{\mathrm{o}}]_j \right)^2} \tag{18}$$

The CV score represents an estimate of the analysis error based on the idea that each observation is used as an independent verification of the analysis field. The error estimate is conservative because in its calculation we're not considering all the available information, thus performing an implicit degradation of the local resolution of the observational network. The CV analysis is also useful for data quality control purposes (see Section 3.4).

3.3.2 Integral Data Influence (IDI)

The Integral Data Influence (IDI) of the subset of station points $Y = \{(x_k, y_k, z_k)\}_{k=1,\ldots,K}$ on the j-th station location is $\left[\mathbf{y}^{Y,\mathrm{IDI}}\right]_j$ and it is written as:

$$\left[\mathbf{y}^{Y,\mathrm{IDI}}\right]_j = \sum_{k=1}^{K} \frac{\partial [\mathbf{y}^{\mathrm{a}}]_j}{\partial [\mathbf{y}^{\mathrm{o}}]_k} = \sum_{k=1}^{K} [\mathbf{W}]_{jk} \tag{19}$$

The IDI indicates the sensitivity of the analysis in a point to variations in the observed values measured at the stations belonging to Y. The IDI value depends both on the station distribution and on the error covariance models assumed within the OI but it is independent of the actual observed values.

The IDI vector $\mathbf{y}^{Y,\mathrm{IDI}}$ is the p_i-vector having components $\left[\mathbf{y}^{Y,\mathrm{IDI}}\right]_j$ with $j = 1, \ldots, p_i$.

Similarly, $\left[\mathbf{x}^{Y,\mathrm{IDI}}\right]_i$ is the IDI of the subset of station points $Y = \{(x_k, y_k, z_k)\}_{k=1,\ldots,K}$ on the i-th grid point and it is written as:

$$\left[\mathbf{x}^{Y,\mathrm{IDI}}\right]_i = \sum_{k=1}^{K} \frac{\partial \left[\mathbf{x}^{\mathrm{a}}\right]_i}{\partial \left[\mathbf{y}^{\mathrm{o}}\right]_k} = \sum_{k=1}^{K} \left[\mathbf{K}\right]_{ik} \tag{20}$$

The IDI vector $\mathbf{x}^{Y,\mathrm{IDI}}$ is the n-vector having $\left[\mathbf{x}^{Y,\mathrm{IDI}}\right]_i$ as components, with $i = 1,\ldots,n$. Note that the IDI field corresponds to the analysis field obtained when all observed values are set to 1 and all background values are set to 0 (see Eqs. (5) and (9)). If the i-th grid point is in a dense station area (given the set of stations Y) we would have $\left[\mathbf{x}^{Y,\mathrm{IDI}}\right]_i$ close to 1. On the other hand, grid points located in sparse station areas would result in having an IDI value close to 0. In region of sharp transition between very different station densities it may be possible to have IDI values greater than 1. Note that for a completely isolated observation the IDI value is $\left[\mathbf{y}^{Y,\mathrm{IDI}}\right]_j = 1/\left(1+\varepsilon^2\right)$ (see *Lussana et al.* (2010), Eq. (23)) and not 0 as for a completely isolated grid point.

The combination of leave-one-out cross-validation and IDI concepts lead to $\left[\check{\mathbf{y}}^{Y,\mathrm{IDI}}\right]_j$ which is the Cross-Validated IDI (CV-IDI) of the subset of station points $Y = \{(x_k, y_k, z_k)\}_{k=1,\ldots,K}$ on the j-th station location and it is written as:

$$\left[\check{\mathbf{y}}^{Y,\mathrm{IDI}}\right]_j = \sum_{k=1}^{K} \frac{\partial \left[\check{\mathbf{y}}^{\mathrm{a}}\right]_j}{\partial \left[\mathbf{y}^{\mathrm{o}}\right]_k} = 1 + \frac{1}{1-\left[\mathbf{W}\right]_{jj}} \left(\left[\mathbf{y}^{Y,\mathrm{IDI}}\right]_j - 1 \right) \tag{21}$$

The CV-IDI vector $\check{\mathbf{y}}^{Y,\mathrm{IDI}}$ is the p_i-vector having $\left[\check{\mathbf{y}}^{Y,\mathrm{IDI}}\right]_j$ as components. The CV-IDI interpretation is similar to the IDI one, except that in the case of an isolated station point the corresponding component of the $\check{\mathbf{y}}^{Y,\mathrm{IDI}}$ would be close to 0 instead of a variable critical threshold, depending on the scalar $\varepsilon^2 \equiv \sigma_{\mathrm{o}}^2/\sigma_{\mathrm{b}}^2$, as in the case of IDI.

Fixed a time-stamp, in the following we will use as a measure of the overall data influence for the entire domain the average of the $\check{\mathbf{y}}^{Y,\mathrm{IDI}}$ vector components, where Y coincides with all the stations providing valid observations for that time-stamp:

$$\overline{CVIDI} = \frac{1}{p_i} \sum_{j=1}^{p_i} \left[\check{\mathbf{y}}^{Y,\mathrm{IDI}}\right]_j \tag{22}$$

The closer the value of $\overline{CVIDI}$ to 1 the larger the average area in the analysis field sensitive to differences between observations and background. The closer the value of $\overline{CVIDI}$ to 0 the larger the spatial portion of the analysis field that would be equal to the background (i.e. the larger the number of stations that may be considered as isolated stations). Note that $\overline{CVIDI}$ is not a direct measure of the analysis quality, rather it might be used to interpret analysis characteristics.

3.3.3 Maximum-likelihood estimation of the observation-error variance σ_o^2

Given a sequence of time steps $\{t_i\}_{i=1,\ldots,N}$, the maximum-likelihood estimate of σ_o^2 constrained by the assumptions made in the OI scheme on the error-covariance matrices can be written as (*Lussana et al.* (2010)):

$$\sigma_o^2 = \frac{\sum_{i=1}^{N} \left[(\mathbf{y}^o - \mathbf{y}^a)_{t_i}^T \left(\mathbf{y}^o - \mathbf{y}^b \right)_{t_i} \right]}{\sum_{i=1}^{N} p_i} \tag{23}$$

It is possible to rewrite this expression as $\sigma_o^2 = \sum_j \left(\sigma_o^2\right)_j$, where $\left(\sigma_o^2\right)_j$ can be interpreted as the σ_o^2 estimate for the j-th station location and can be written as:

$$\left(\sigma_o^2\right)_j = \frac{\sum_{i=1}^{N_j} \left\{ \left[(\mathbf{y}^o - \mathbf{y}^a)_{t_i} \right]_{j'} \left[\left(\mathbf{y}^o - \mathbf{y}^b \right)_{t_i} \right]_{j'} \right\}}{N_j} \tag{24}$$

Where $N_j \leq N$ denotes the number of available values for the j-th observation.

3.4 Spatial Consistency Test

A spatial consistency test (SCT) is applied to the temperature observations as described in *Lussana et al.* (2010). The SCT's purpose is twofold: preventing gross errors (GEs) from entering automatic numerical elaboration and returning a quality flag to an external quality control system. The algorithm is based on Bayesian concepts and exploits the existing objective analysis scheme by comparing each observed value with the corresponding leave-one-out cross-validated analysis value (see Paragraph 3.3). Local data density is automatically taken into account to allow a less restrictive test for isolated stations that provide precious information on poorly observed areas. In this first implementation, thresholds and parameters are estimated through a subjective ad hoc tuning.

Consider the p_i observations available at time t_i, the SCT implementation for the j-th observed value can be written as:

$$\left([\mathbf{y}^o]_j - [\check{\mathbf{y}}^a]_j \right)^2 \geq T^2 \left(\sigma_{o,j}^2 + \check{\sigma}_{a,j}^2 \right) \tag{25}$$

Or given our assumptions on OI (see Sec. 3.1):

$$\left([\mathbf{y}^o]_j - [\check{\mathbf{y}}^a]_j \right) \left([\mathbf{y}^o]_j - [\mathbf{y}^a]_j \right) \geq T^2 \sigma_o^2 \tag{26}$$

Where the observation error variance is set to $\sigma_o^2 = 3\,^\circ\mathrm{C}^2$ and $T^2 = 20$. Each observation affects the CV analysis at nearby stations (see Eq. (17)). As a consequence, if more

than one observation simultaneously fails the SCT then only the one having the largest square residual (left-hand side of Eq. (26)) is flagged. All the CV analysis are then recomputed without using the flagged observation and the SCT is repeated until no observation fails the test.

Note that our OI scheme assumes implicit knowledge of the observation-error variance, σ_o^2, as only the ratio between observation- and background-error variances actually enters the interpolation scheme. For the SCT, as stated in Eq. (26), the value of σ_o^2 must instead be explicitly estimated and it can be done as described in Sec. (3.3.3).

In Figs. (9) and (10) the distributions of observed minus CV analysis values $[\mathbf{y}^{\mathrm{o}}]_j - [\check{\mathbf{y}}^{\mathrm{a}}]_j$ are shown for *TEMP1h* and *TEMP1d*, respectively. We point out that *TAMRR* observations undergo a manual data quality control procedure before entering the spatial interpolation procedure and for this reason the SCT flags very few observations as being affected by GEs. In the case of *TA*, due to the high frequency of GEs occurrence, shown in Fig. (9), the presence of a SCT is of fundamental importance both to deliver real time products and to facilitate the historical data quality control. Note that the bell-shaped tail of SCT-rejected observations shown in Fig. (9) is due to observations collected by a few stations belonging to the same sub-network, which is the one managed by The Norwegian Public Roads Administration-Statens Vegvesen.

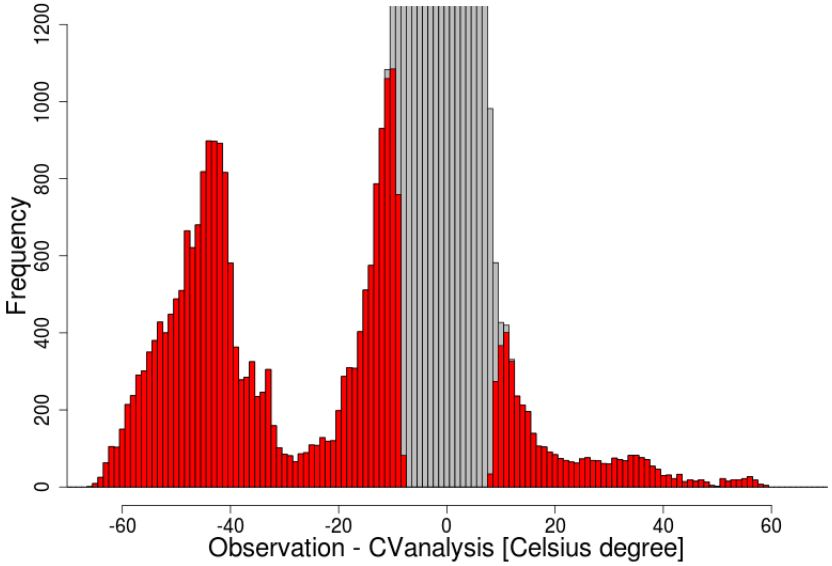

Figure 9: *TA*. Spatial Consistency Test results. Distribution of $[\mathbf{y}^{o}]_j - [\check{\mathbf{y}}^{a}]_j$ values. Gray: all observations. Red: observations flagged as affected by gross measurement errors (GEs). Statistics based on 1 year of data, from 2013.09.01 to 2014.08.31, for the Norwegian mainland. Number of observations used: 4.219.230; number of observations rejected as probably affected by GEs: 26.182 (6.2‰).

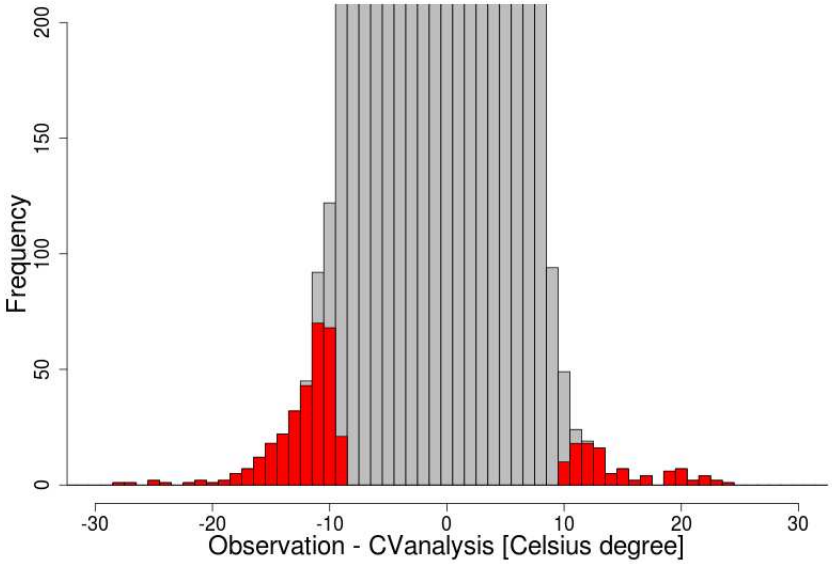

Figure 10: Spatial Consistency Test results for *TAMRR*. Distribution of $[\mathbf{y}^{\mathrm{o}}]_j - [\check{\mathbf{y}}^{\mathrm{a}}]_j$ values. Gray: all observations. Red: observations flagged as affected by gross measurement errors (GEs). Statistics based on 11 years of data, from 2003.09.01 to 2014.08.31, for the Norwegian mainland. Number of observations used: 932.239; number of observations rejected as probably affected by GEs: 413 $(0.044‰)$.

4 Test Case: 2015, January 1

A challenging situation has been chosen as a test case for the spatial interpolation scheme: the first of January 2015, characterized by a significant temperature inversion (i.e. an increase in temperature with height) in Southern Norway. In the daily mean temperature, the temperature inversion is evident both for *TEMP1d* in Fig. (11) and for *TEMP1d24h* in Fig. (12). Note that *TEMP1d24h* benefits from the inclusion of observations outside Norway, which are not included in *TEMP1d*, as it is shown in the corresponding IDI Fig. (13) ($100 * IDI$ is actually shown). In the case of hourly temperature *TEMP1h*, the analyses are shown in Figs. (14)-(16) at a 3-hourly step. The local temperature inversions in the valleys of Eastern Norway last for the whole 24h period. The corresponding IDI fields are shown in Figs. (17)-(19). The Figs. (20)-(70) refer to the construction of the blended pseudo-background field for *TEMP1d*. In particular, Figs. (20)-(22) show all the regions (42 in this case) where regional pseudo-background fields are computed independently,

together with the weight each regional pseudo-background field has in the total blended pseudo-background field. The Figs. (23)-(25) show the vertical profile of temperature for a selection of regional domains. Each of the three Figures shows an example of the three different formulations for the regional pseudo-background field (see Sec. 3.2.2). By comparing the central panel of each Figure with the corresponding right panel, it is possible to have an idea of the effect the blending has on the computation of the final pseudo-background field (see Sec. 3.2). In Fig. (23) an example of a regional pseudo-background field computed as a linear parametric function of the spatial coordinates (i.e. $\mathbf{y}_d^{b0}$) is shown. Note that this formulation has been often applied in Northern Norway, where the station network is sparser. In Fig. (24) an example of a regional pseudo-background field obtained as the composition of two distinct linear regressions as in *Uboldi et al.* (2008) is shown (i.e. $\mathbf{y}_d^{b1}$). In Fig. (25) an example of a regional pseudo-background field obtained as the composition of two distinct linear regressions as in *Frei* (2014) is shown (i.e. $\mathbf{y}_d^{b2}$). In the case of these two last formulations, the spatial trend in the horizontal allows the vertical temperature profile to be adapt locally within different areas of the sub-domain under consideration. Further examples of the vertical profile of temperature for a selection of regional domains are reported in Appendix A.

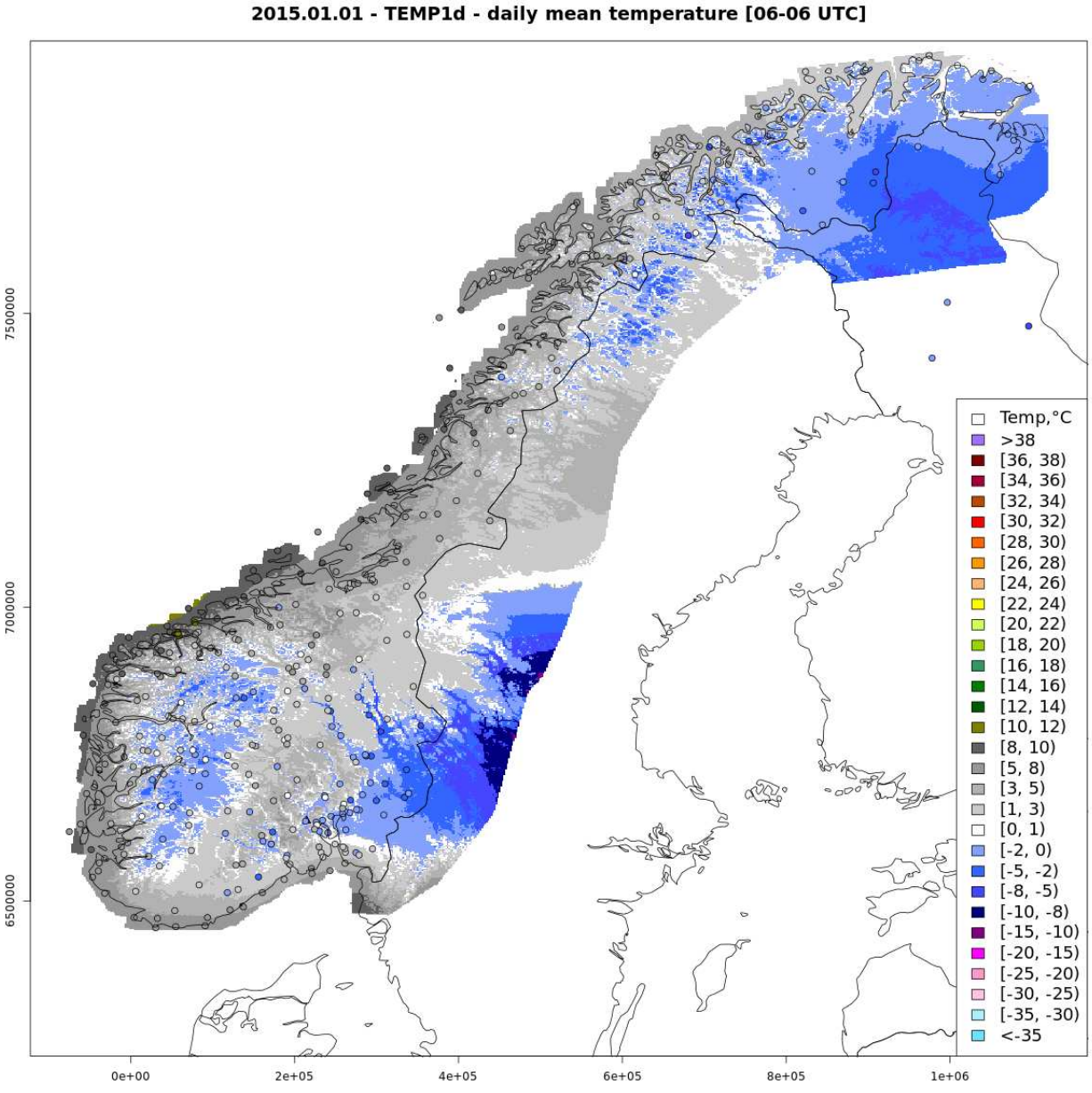

Figure 11: *TEMP1d* Analysis field for the day 2015/01/01.

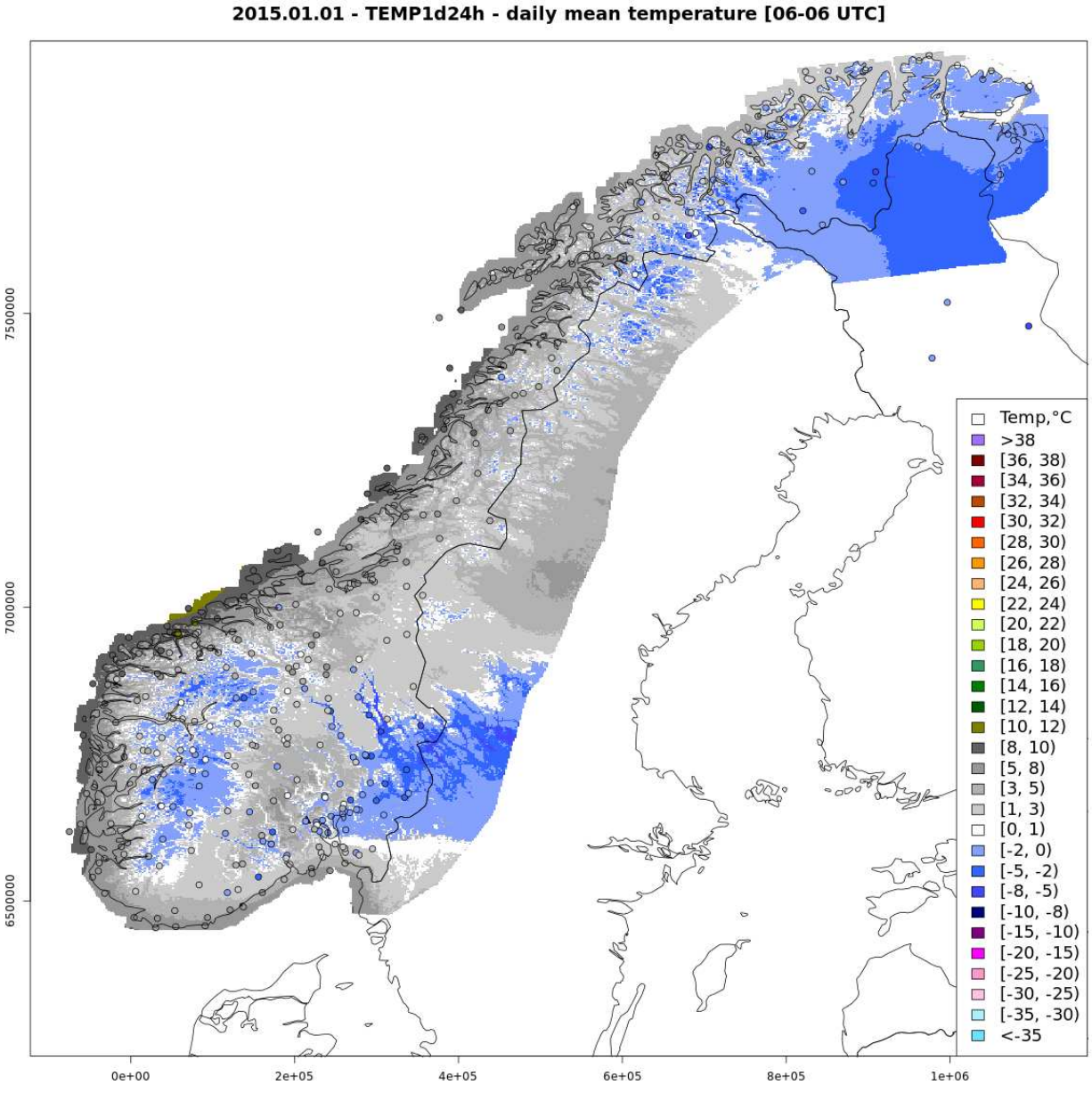

Figure 12: *TEMP1d24h* Analysis field for the day 2015/01/01.

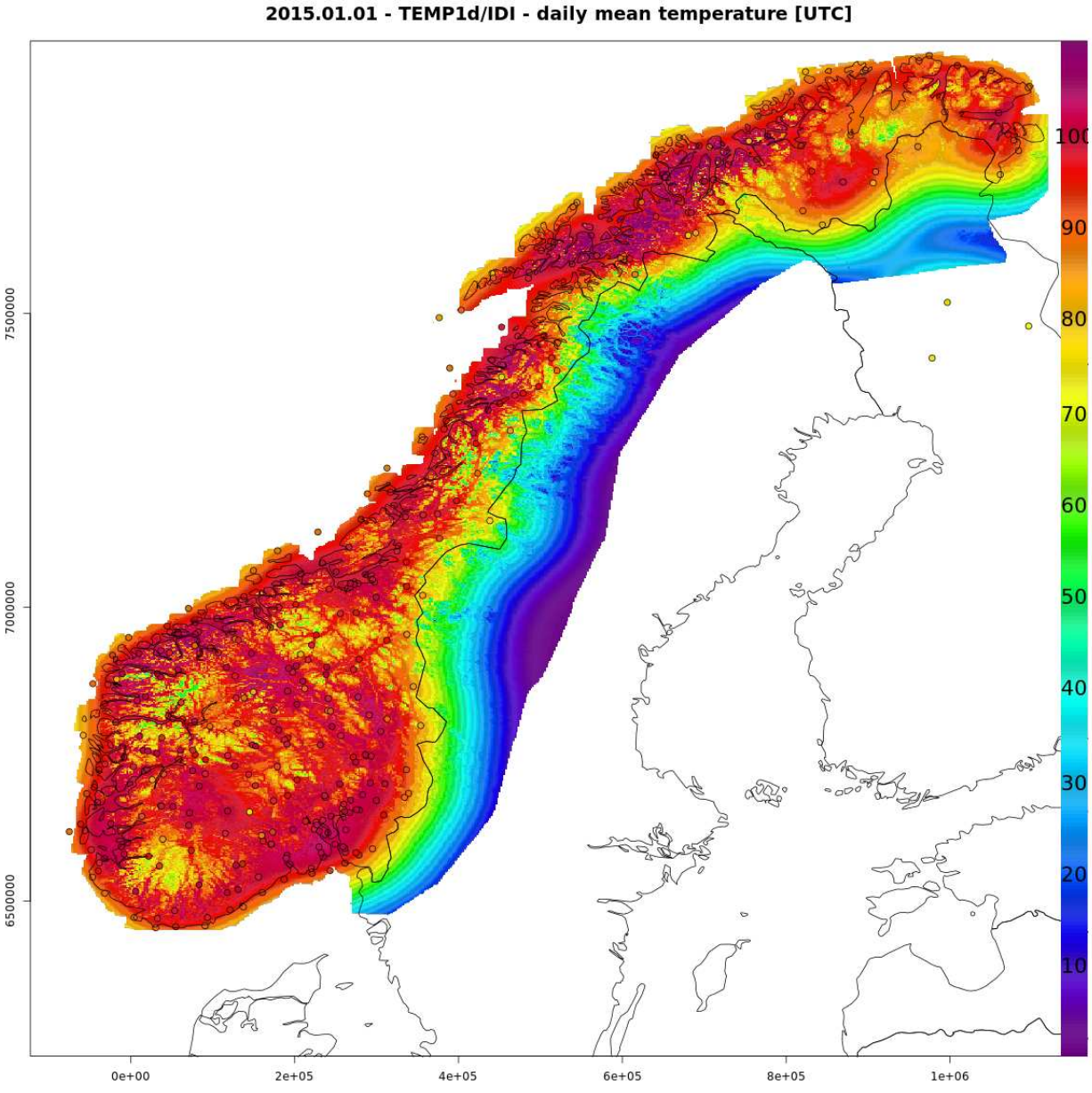

Figure 13: *TEMP1d* IDI field for the day 2015/01/01.

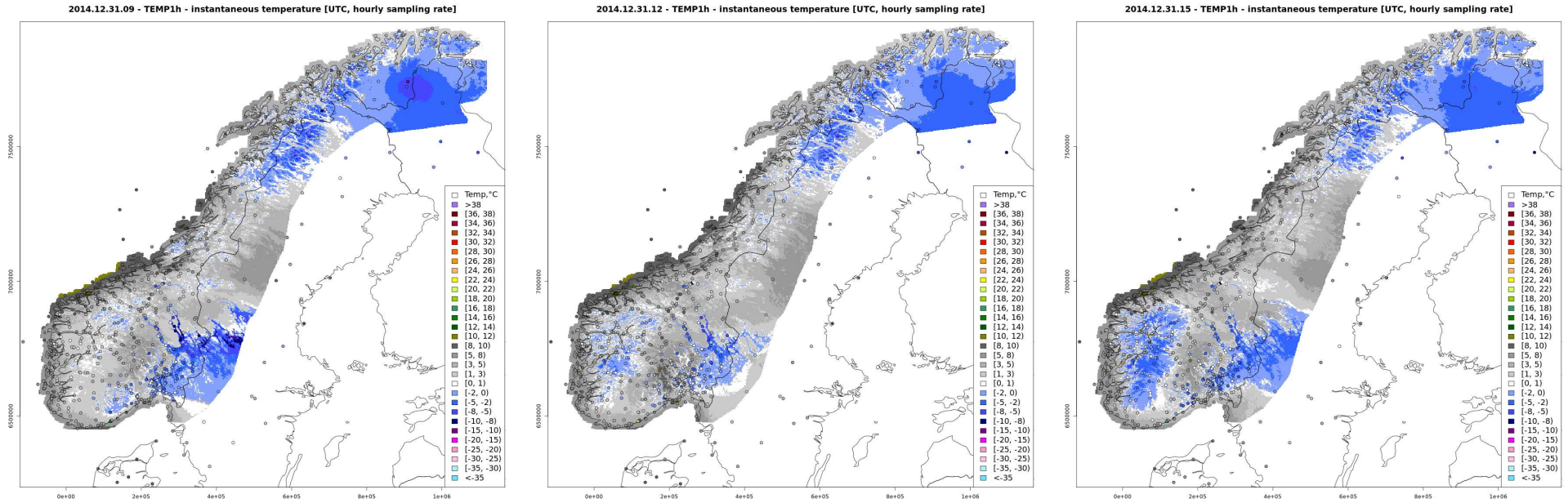

Figure 14: *TEMP1h* Analysis field for the day 2014/12/31. Left panel: 09 UTC. Central panel: 12 UTC. Right panel: 15 UTC.

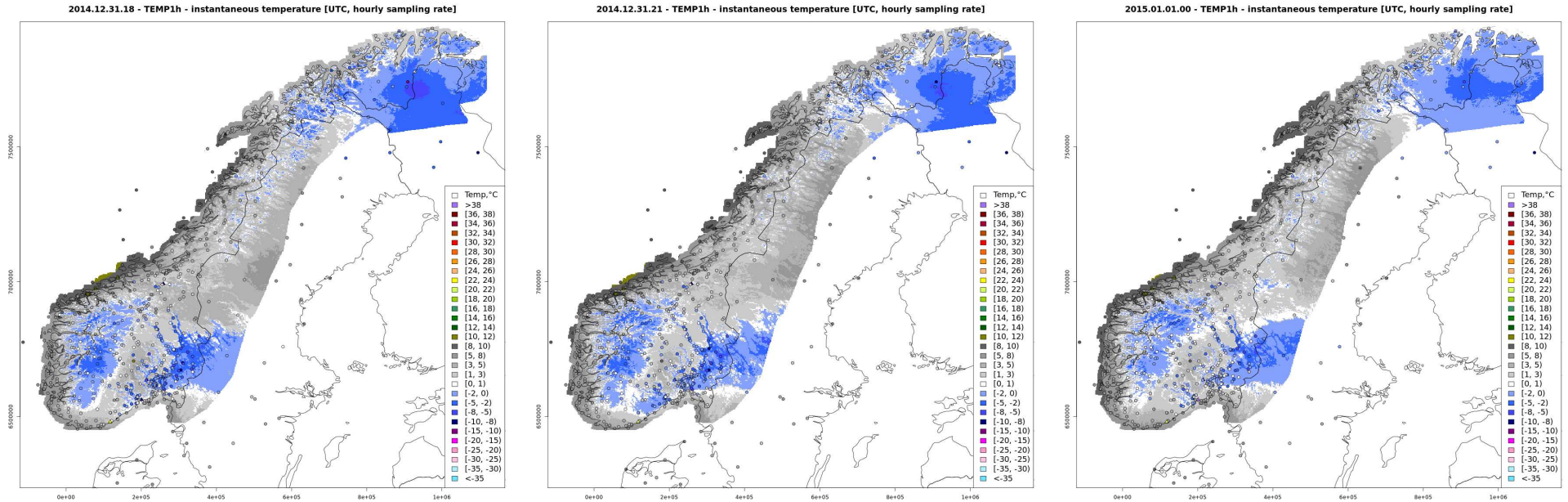

Figure 15: *TEMP1h* Analysis field. Left panel: 2014/12/31 18 UTC. Central panel: 2014/12/31 21 UTC. Right panel: 2015/01/01 00 UTC.

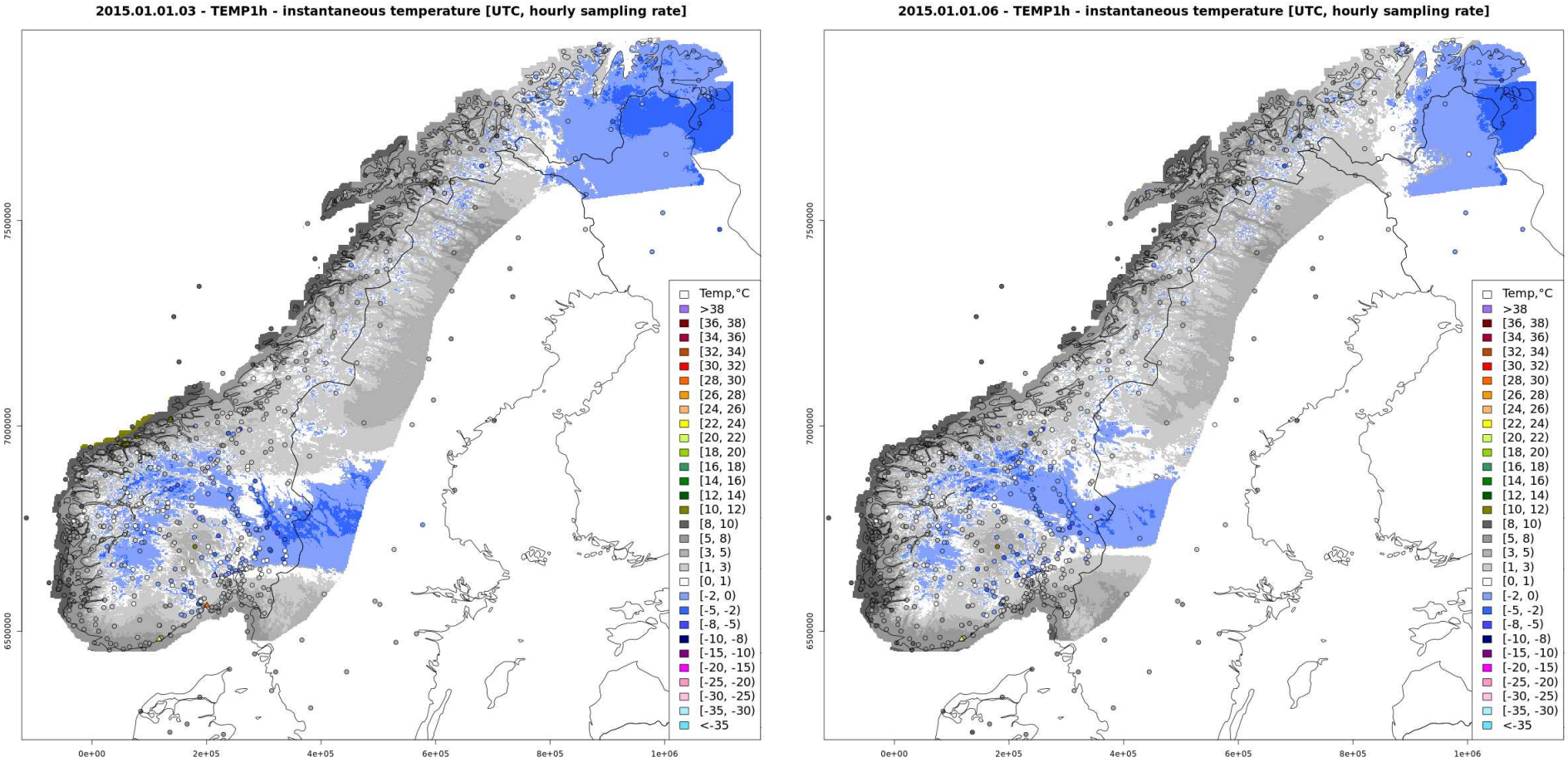

Figure 16: *TEMP1h* Analysis field for the day 2015/01/01. Left panel: 03 UTC. Right panel: 06 UTC.

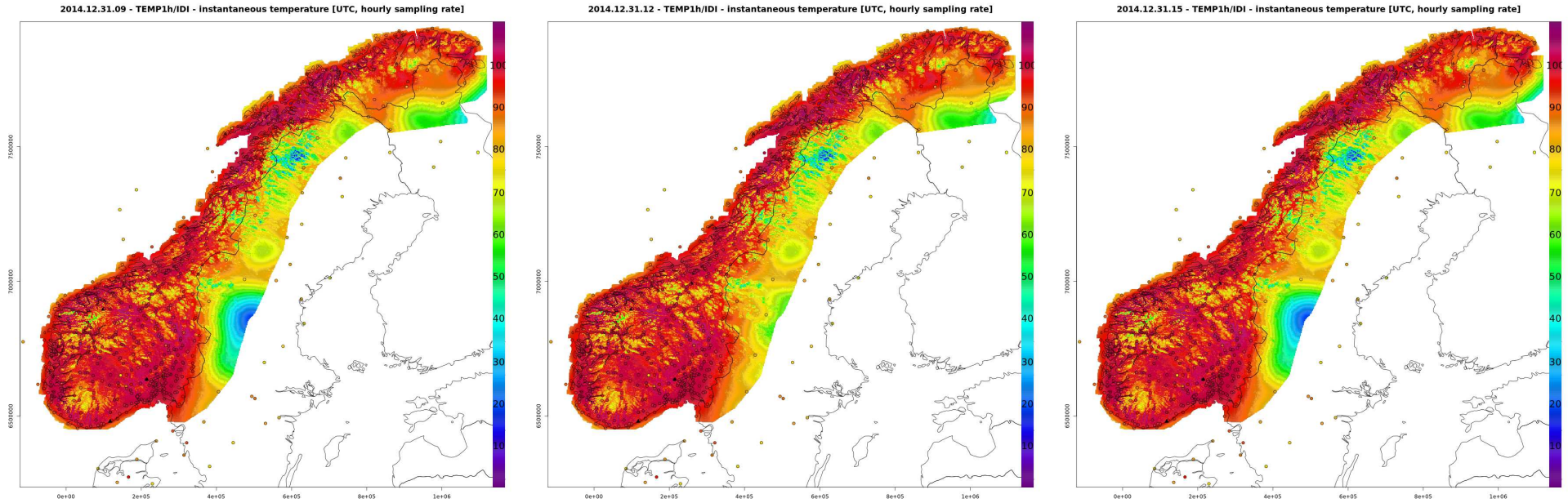

Figure 17: *TEMP1h* IDI field for the day 2014/12/31. Left panel: 09 UTC. Central panel: 12 UTC. Right panel: 15 UTC.

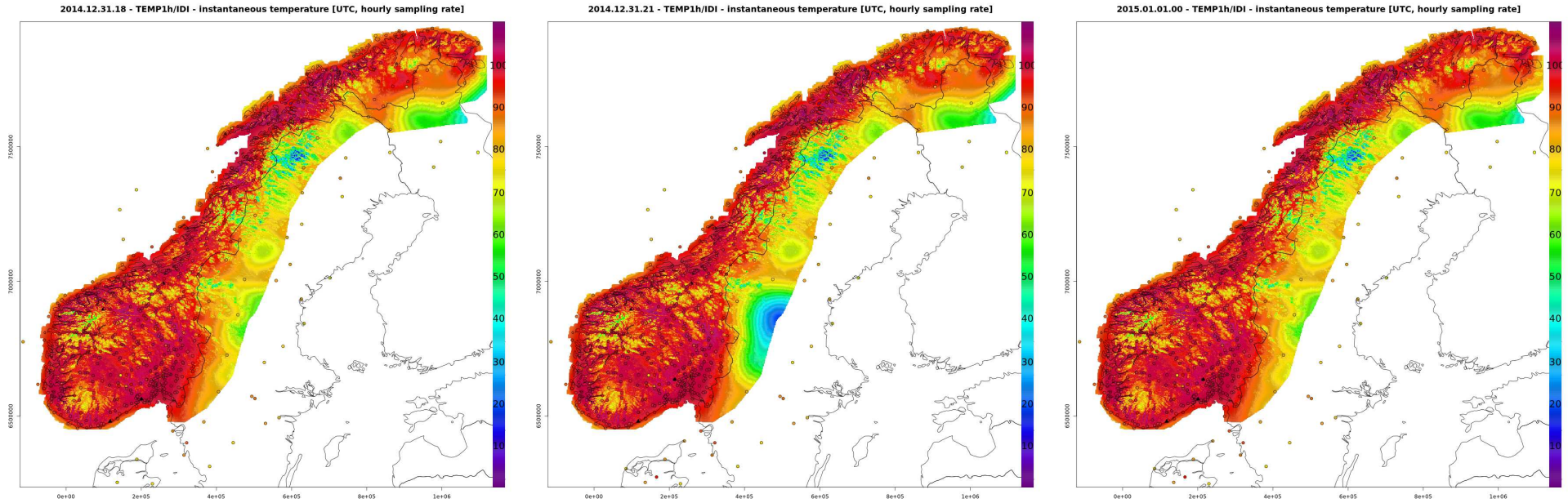

Figure 18: *TEMP1h* IDI field. Left panel: 2014/12/31 18 UTC. Central panel: 2014/12/31 21 UTC. Right panel: 2015/01/01 00 UTC.

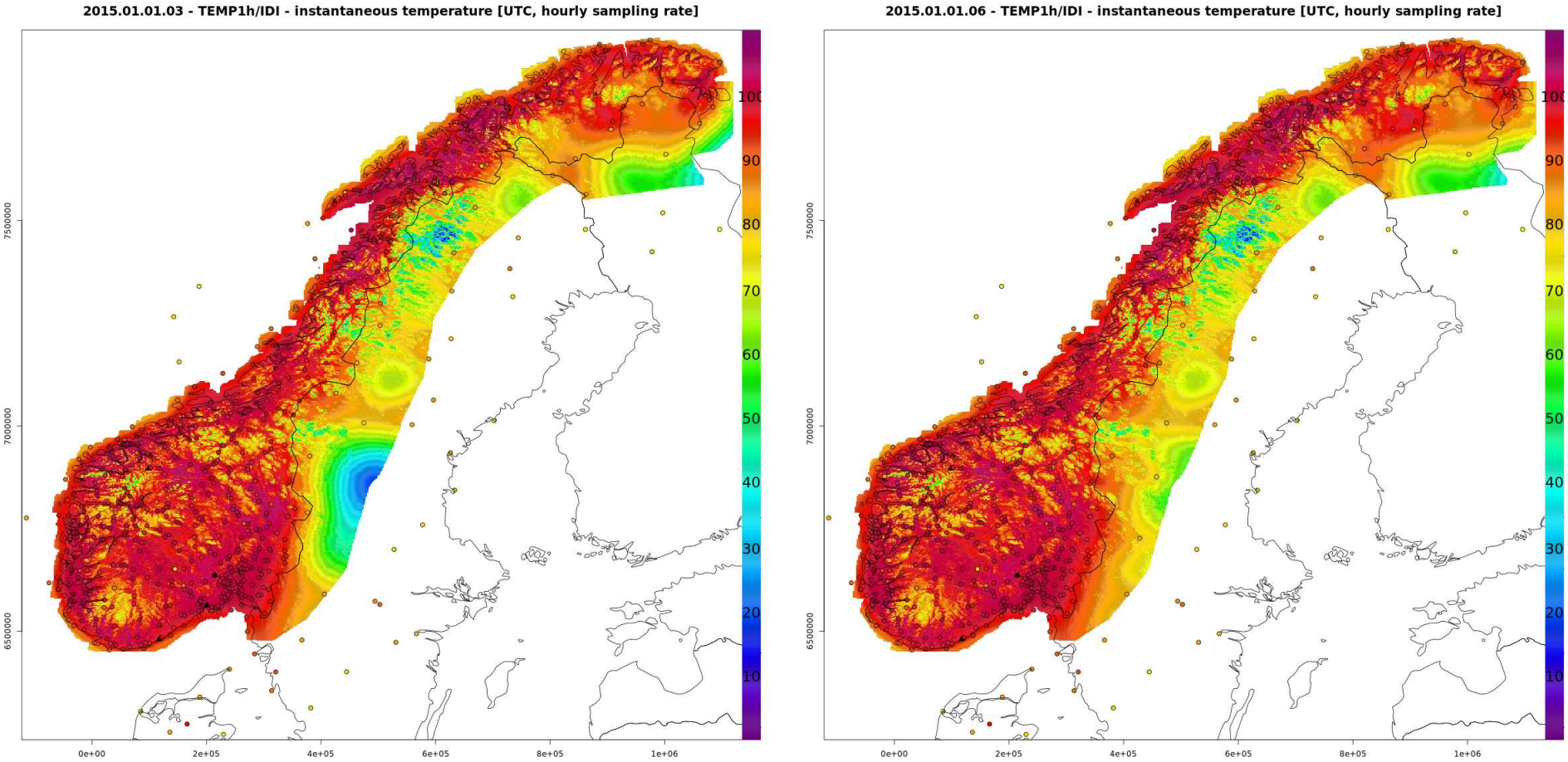

Figure 19: *TEMP1h* IDI field for the day 2015/01/01. Left panel: 03 UTC. Right panel: 06 UTC.

Figure 20: Test case 2015/01/01. *TEMP1d* ensemble of regional pseudo-background domains. station distribution (circles); Y_d set of stations included in the d-th sub-domain (black dots); IDI-based weights used for blending $\mathbf{x}^{Y_d,\mathrm{IDI}} / \sum_{d=1}^{D} \mathbf{x}^{Y_d,\mathrm{IDI}}$ (shaded, see Fig. (51) for the legend).

Figure 21: Test case 2015/01/01. *TEMP1d* ensemble of regional pseudo-background domains. Continue from Fig. (20).

Figure 22: Test case 2015/01/01. *TEMP1d* ensemble of regional pseudo-background domains. Continue from Fig. (20).

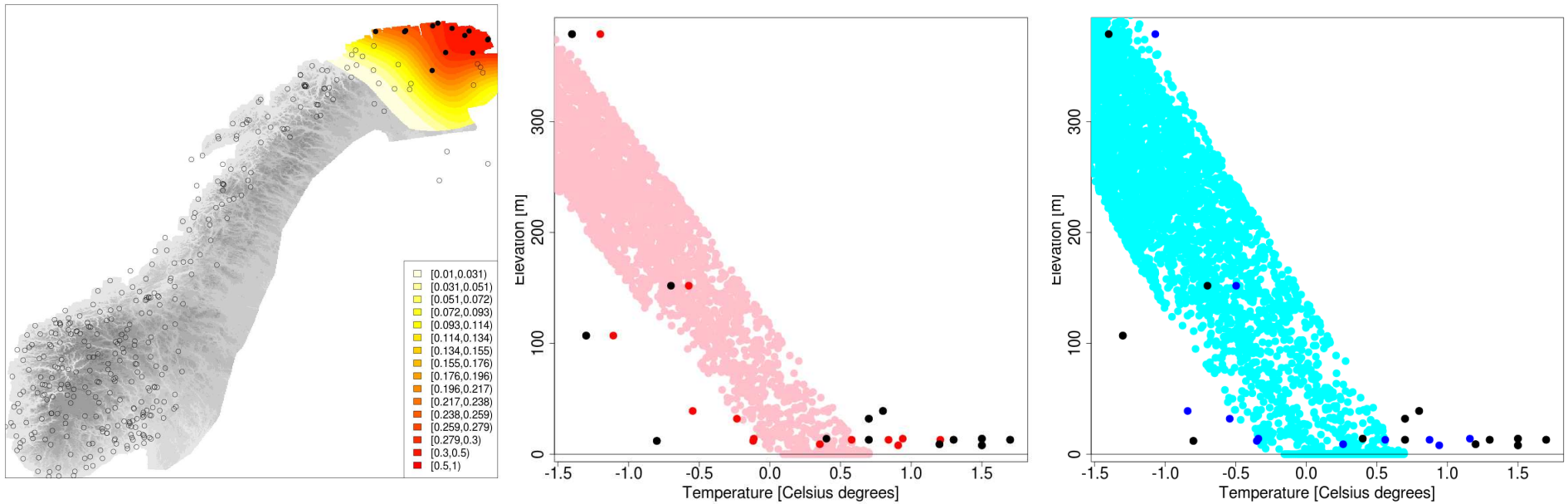

Figure 23: Test case 2015/01/01. *TEMP1d* construction of the pseudo-background. Left panel: station distribution (circles); Y_d stations included in the sub-domain (black dots); $\mathbf{x}^{Y_d,\mathrm{IDI}} / \sum_{d=1}^{D} \mathbf{x}^{Y_d,\mathrm{IDI}}$ (shaded). Central panel: regional pseudo-background temperature vs Elevation a.m.s.l.: observed values (black dots); $\mathbf{y}_d^{\mathrm{b}}$ (red dots); $\mathbf{x}_d^{\mathrm{b}}$ (pink dots, only the 1% grid points more influenced by the Y_d stations are shown). Right panel: blended pseudo-background temperature vs Elevation a.m.s.l.: observed values (black dots); $\mathbf{y}^{\mathrm{b}}$ (blue dots); $\mathbf{x}^{\mathrm{b}}$ (cyan dots, only the 1% grid points more influenced by the Y_d stations are shown)

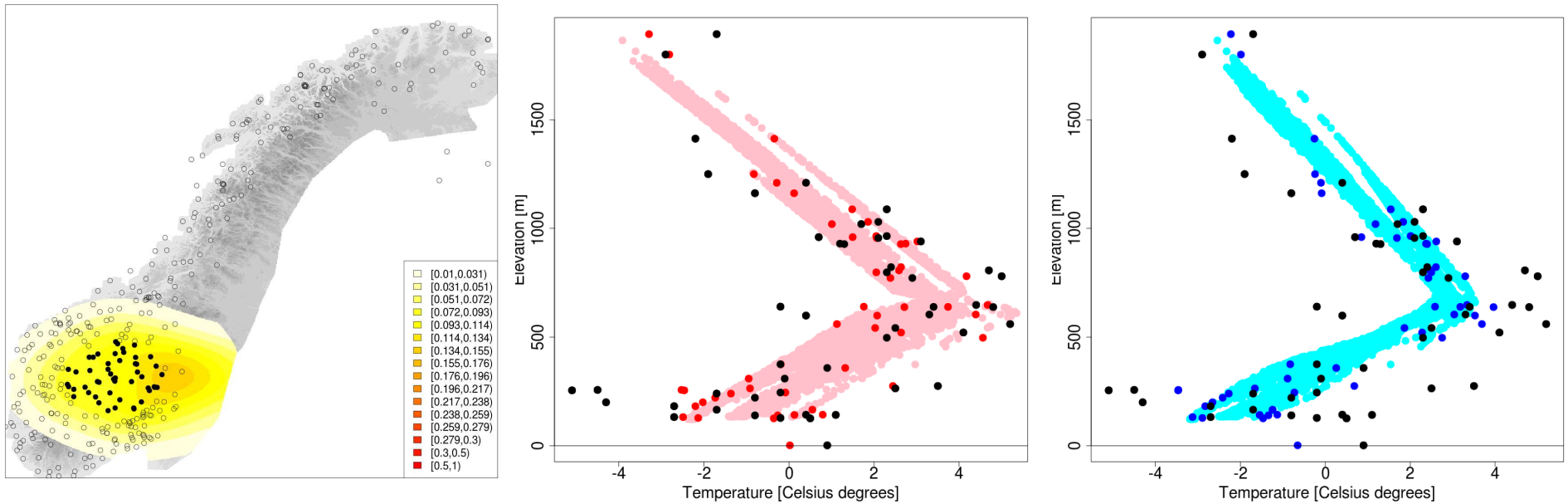

Figure 24: Test case 2015/01/01. *TEMP1d* construction of the pseudo-background. Left panel: station distribution (circles); Y_d stations included in the sub-domain (black dots); $\mathbf{x}^{Y_d,\mathrm{IDI}} / \sum_{d=1}^{D} \mathbf{x}^{Y_d,\mathrm{IDI}}$ (shaded). Central panel: regional pseudo-background temperature vs Elevation a.m.s.l.: observed values (black dots); $\mathbf{y}_d^{\mathrm{b}}$ (red dots); $\mathbf{x}_d^{\mathrm{b}}$ (pink dots, only the 1% grid points more influenced by the Y_d stations are shown). Right panel: blended pseudo-background temperature vs Elevation a.m.s.l.: observed values (black dots); $\mathbf{y}^{\mathrm{b}}$ (blue dots); $\mathbf{x}^{\mathrm{b}}$ (cyan dots, only the 1% grid points more influenced by the Y_d stations are shown)

5 Evaluation

The performances of the spatial interpolation procedure are evaluated both at station locations and at grid points.

Consider the following variables, which are commonly used in data assimilation for the evaluation of an analysis procedure:

- CV-residuals O-CVA $y^{\mathrm{o}} - \check{y}^{\mathrm{a}}$: observation minus CV-analysis (see Sec. 3.3.1).
- analysis residual O-A $y^{\mathrm{o}} - y^{\mathrm{a}}$: observation minus analysis (see Sec. 3.1).
- innovation O-B $y^{\mathrm{o}} - y^{\mathrm{b}}$: observation minus pseudo-background (see Sec. 3.2).

By means of the CV-analysis the quality assessment done for station locations with the analysis is extended to the grid points, where the observed values are not available.

Given the j-th station, the assessment of a specific variable, for instance $y^{\mathrm{o}} - y^{\mathrm{b}}$, is based on the set of N_j values $\left\{ \left([\mathbf{y}^{\mathrm{o}}]_j - [\mathbf{y}^{\mathrm{b}}]_j \right)_{t_i} \right\}_{i=1,\ldots,N_j}$, where t_i is the time index. Note that the number of available observations N_j is station dependent. In the following we would often refer to accuracy and precision, which are related to the statistical bias and the root mean square error:

$$\mathrm{bias}_j = \frac{1}{N_j} \sum_i \left([\mathbf{y}^{\mathrm{o}}]_j - \left[\mathbf{y}^{\mathrm{b}}\right]_j \right)_{t_i} \tag{27}$$

$$\mathrm{rmse}_j = \sqrt{\frac{1}{N_j} \sum_i \left([\mathbf{y}^{\mathrm{o}}]_j - [\mathbf{y}^{\mathrm{b}}]_j \right)^2_{t_i}} \tag{28}$$

In particular: the accuracy is related to the presence of systematic errors and it is quantified by means of the bias value; the precision is a description of random errors, a measure of statistical variability, and it is quantified through the root mean square error.

For all the quantities, the bias should be close to zero because both the observations and the pseudo-background are assumed to be unbiased estimates of the true atmospheric state and no bias is introduced by the OI. However, it is worth remarking that the presence of systematic errors in either the observations or the pseudo-background field can influence the parameter estimation, typically leading to an overestimation of the error variances.

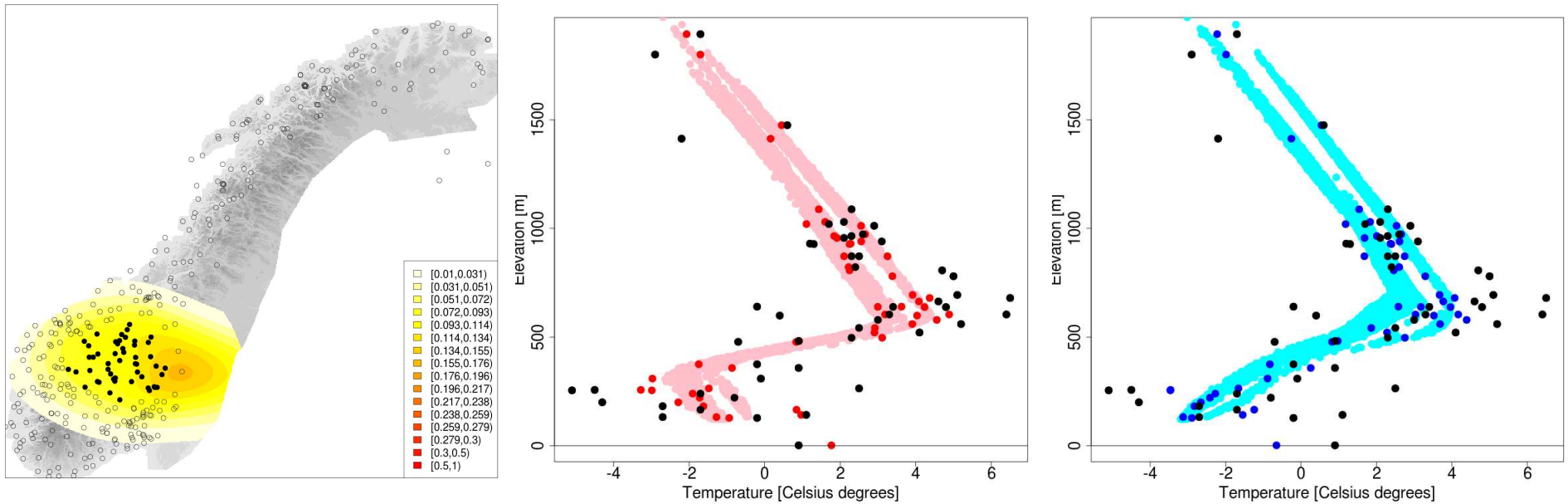

Figure 25: Test case 2015/01/01. *TEMP1d* construction of the pseudo-background. Left panel: station distribution (circles); Y_d stations included in the sub-domain (black dots); $\mathbf{x}^{Y_d,\mathrm{IDI}} / \sum_{d=1}^{D} \mathbf{x}^{Y_d,\mathrm{IDI}}$ (shaded). Central panel: regional pseudo-background temperature vs Elevation a.m.s.l.: observed values (black dots); $\mathbf{y}_d^{\mathrm{b}}$ (red dots); $\mathbf{x}_d^{\mathrm{b}}$ (pink dots, only the 1% grid points more influenced by the Y_d stations are shown). Right panel: blended pseudo-background temperature vs Elevation a.m.s.l.: observed values (black dots); $\mathbf{y}^{\mathrm{b}}$ (blue dots); $\mathbf{x}^{\mathrm{b}}$ (cyan dots, only the 1% grid points more influenced by the Y_d stations are shown)

5.1 Density plots

The density plots in Figs. (26)-(28) show the distribution of values of: CV-analysis, analysis and background at station locations as a function of the observed value. The range of values of both the observation and the dependent variable has been divided in bins of 1°C width and the number of pairs falling in each 1°C by 1°C cell (i.e. the collocations) is shown in the figures.

About the density plots in Figs. (26)-(28), it is worth mentioning that the numbers defining the intervals reported in the legends are the sample percentiles of the set of collocation values, such that: the first interval span the range of collocation values up to the first quartile; the upper limit for the second interval is the median of the distribution; the upper limit for the third interval is the third quartile; the upper limit for the fourth interval is the ninth decile; the last interval includes the higher collocation values up to the maximum value, which is reported as the largest value in the legend.

Consider the analysis. If we define the event O as having observed a value of temperature between o and $o + \mathrm{d}o$ and the event A as our spatial interpolation procedure having estimated an analysis value between a and $a + \mathrm{d}a$, then the density plots are related to $P(O \cap A)$, which is the probability of the joint event O and A.

In addition, because the conditional probability of A given O can be written as $P(A|O) = P(O \cap A)/P(O)$ then it is possible to extract the conditional probability densities from the density plots by normalizing the collocations in the plot corresponding to $P(O \cap A)$ for the total number of collocations involving the occurrence of event O.

Similarly, we proceed for the background and the CV-analysis by defining the events B and CVA, respectively.

The empirical conditional probability density functions (PDFs) for CVA and A given O are shown in Figs. (29) and (30) for several observed values.

To quantify the uncertainty and the systematic error of the empirical conditional PDFs show in the Figures, the Normal PDF which better approximate each conditional PDF has been computed and its parameters are reported in Tables 1 and 2.

As expected, Figs. (26)-(28) systematically show that $P(O \cap B)$ is characterized by the higher dispersion around the 1:1 line, that is the background is a less precise estimate of the observations because we wanted it to be representative of an area rather than of a point observation.

The analysis results in a far more precise estimate of the observed value compared

to the background. In this case, the spread around the 1:1 line is indicative of the observation representativity error, which is the component of an observed value due to small scales that the spatial interpolation scheme, with the prescribed error covariance models, is unable to resolve.

By means of the CV-analysis it is shown that also for grid points the spatial interpolation do provide a significant improvement over the background.

Perhaps, the improvement is less evident in the case of *TEMP1d24h*: in Fig. (27) the density plots for *CVA* and *B* are more similar than for the other products. This fact is pointed out by several evaluation scores and we'll discuss it in the following.

A second relevant common feature of both hourly and daily aggregated temperature, as shown in Figs. (26)-(28), is that CV-analysis, analysis and background provide a more accurate and precise representation of the truth for positive temperature values than for negative values.

The accuracy of the results is rather stable across the range of climatological values, except for the most extreme negative values (values below $-30\,^{\circ}$C) where the Figures suggest the presence of a systematic warm bias in all the variables. We think that extreme negative values of temperature result from atmospheric phenomena characterized by length scales lower or comparable to the local station density, which makes these situation particularly challenging to represent.

For the CV-analysis and the analysis these effects are quantified in Tables 1 and 2, respectively.

In the case of *TEMP1h*, from Tables 1 and 2 it is possible to recognize a warm bias in $P(A|O)$ below $-20\,^{\circ}$C while for $P(CVA|O)$ the value is $-15\,^{\circ}$C. The uncertainty, as quantified in the tables by the standard deviation σ, both for $P(A|O)$ and $P(CVA|O)$ follows the shape of an "hourglass" across the possible range of observed values: higher uncertainties for the most extreme negative temperature values (e.g. $\sigma = 2.4\,^{\circ}$C for $P(CVA|O)$ when $O = -30\,^{\circ}$); then, it decreases gradually and the narrow part of the "hourglass" is located for temperatures between $0\,^{\circ}$C and $15\,^{\circ}$C; finally, it rises again for the higher observed temperatures, yet reaching only half of the uncertainty associated with the negative temperatures. It is worth remarking that the interval where the estimates are more precise is probably the most relevant for hydrological applications.

In the cases of *TEMP1d* and *TEMP1d24h*, the analysis has almost no bias except for the most negative temperatures. The uncertainty follows the shape of a "funnel", with the higher uncertainties for negative temperatures (e.g. $\sigma = 2.3\,^{\circ}$C for $P(CVA|O)$ when

$O = -20\,^{\circ}\mathrm{C}$, in the case of *TEMP1d*), then the analysis gradually becomes more precise as the temperature increases.

	$P(CVA\|O) \sim N(\mu, \sigma^2)$					
	TEMP1d		TEMP1d24h		TEMP1h	
$O\,[^\circ\mathrm{C}]$	$\mu\,[^\circ\mathrm{C}]$	$\sigma\,[^\circ\mathrm{C}]$	$\mu\,[^\circ\mathrm{C}]$	$\sigma\,[^\circ\mathrm{C}]$	$\mu\,[^\circ\mathrm{C}]$	$\sigma\,[^\circ\mathrm{C}]$
-30	–	–	–	–	-27	2.4
-25	–	–	–	–	-23	2.4
-20	-19	2.3	-19	2.6	-19	2.3
-15	-14	1.7	-15	1.7	-14	2.0
-10	-10	1.4	-10	1.2	-10	1.5
-5	-5	1.0	-5	0.9	-5	1.1
0	0	0.8	0	0.7	0	0.9
5	5	0.7	5	0.6	5	0.9
10	10	0.7	10	0.6	10	0.9
15	15	0.7	15	0.6	15	0.9
20	20	0.8	20	0.7	20	1.1
25	–	–	–	–	24	1.2
30	–	–	–	–	29	1.3

Table 1: Normal probability density function (μ is the expected value and σ^2 is the variance) obtained by fitting to the empirical conditional probability density function for the CV-analysis given the observed value *O*, for years 2010-2015 (see also Fig. 29).

	$P(A\|O) \sim N(\mu, \sigma^2)$					
	TEMP1d		TEMP1d24h		TEMP1h	
O [°C]	μ [°C]	σ [°C]	μ [°C]	σ [°C]	μ [°C]	σ [°C]
−30	–	–	–	–	−29	1.3
−25	–	–	–	–	−24	1.5
−20	−19	1.5	−19	1.6	−19	1.5
−15	−15	1.1	−15	1.1	−15	1.3
−10	−10	0.9	−10	0.8	−10	1.1
−5	−5	0.7	−5	0.7	−5	0.8
0	0	0.6	0	0.6	0	0.7
5	5	0.5	5	0.5	5	0.7
10	10	0.6	10	0.5	10	0.7
15	15	0.5	15	0.5	15	0.7
20	20	0.6	20	0.6	20	0.9
25	–	–	–	–	24	0.9
30	–	–	–	–	29	1.1

Table 2: Normal probability density function (μ is the expected value and σ^2 is the variance) obtained by fitting to the empirical conditional probability density function for the analysis given the observed value O, for years 2010-2015 (see also Fig. 30).

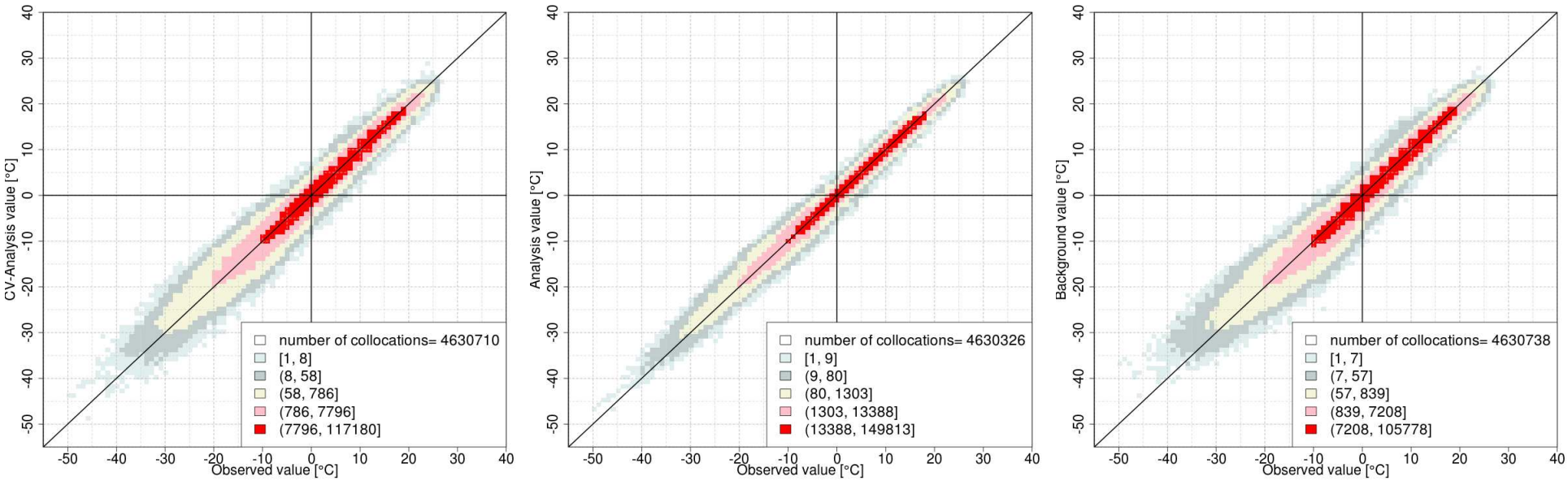

Figure 26: *TEMP1d*. Density plots of: (left) CV-analysis *vs* observations; (central) analysis *vs* observations; (right) background *vs* observations, for years 1957-2015. The shading indicates the number of pairs (or collocations) within each 1°C by 1°C cell and the total number of collocations is reported in the legend.

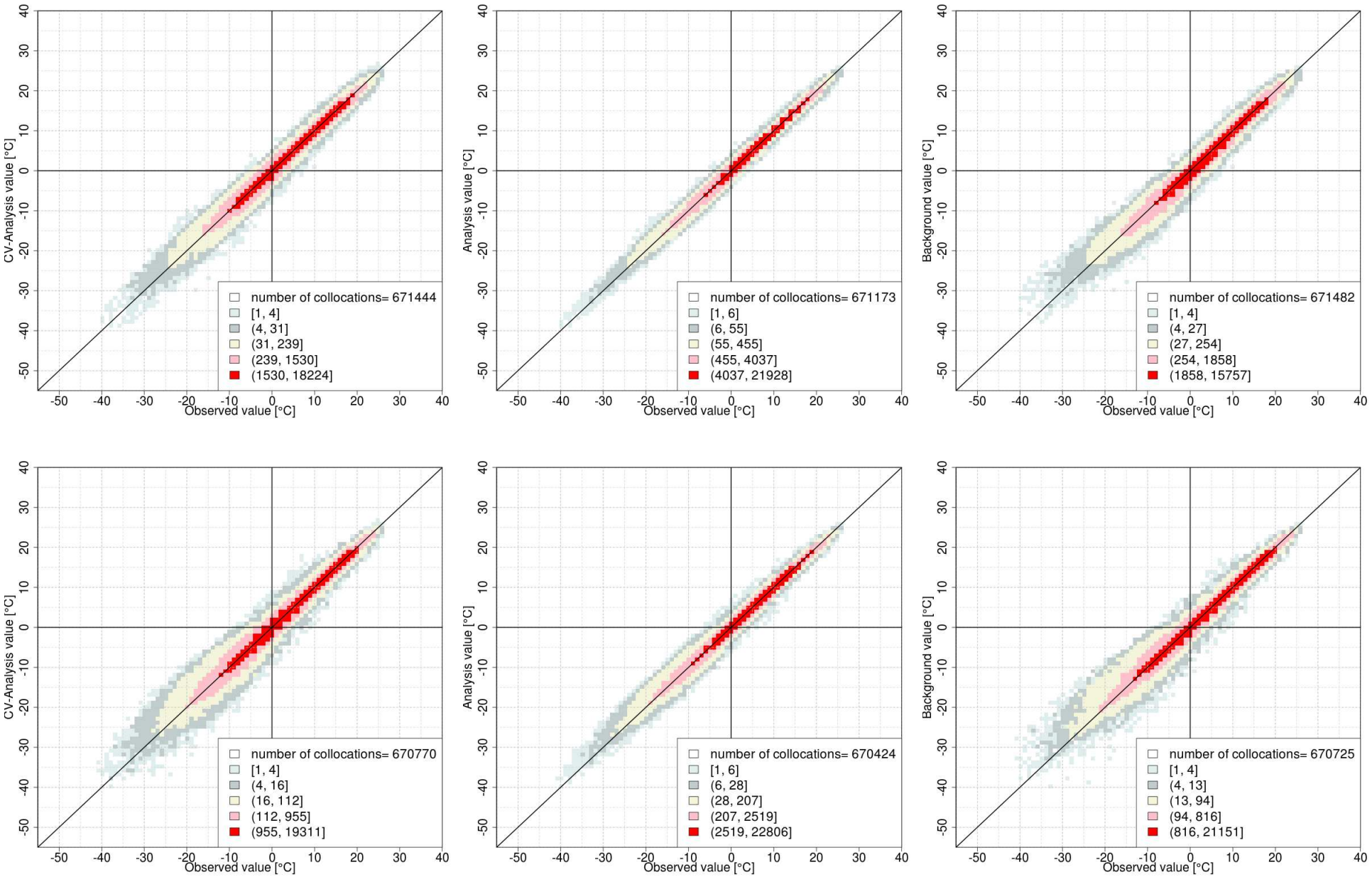

Figure 27: *TEMP1d* (top row) and *TEMP1d24h* (bottom row). Density plots of: (left) CV-analysis *vs* observations; (central) analysis *vs* observations; (right) background *vs* observations, for years 2010-2015. The shading indicates the number of pairs (or collocations) within each 1°C by 1°C cell and the total number of collocations is reported in the legend.

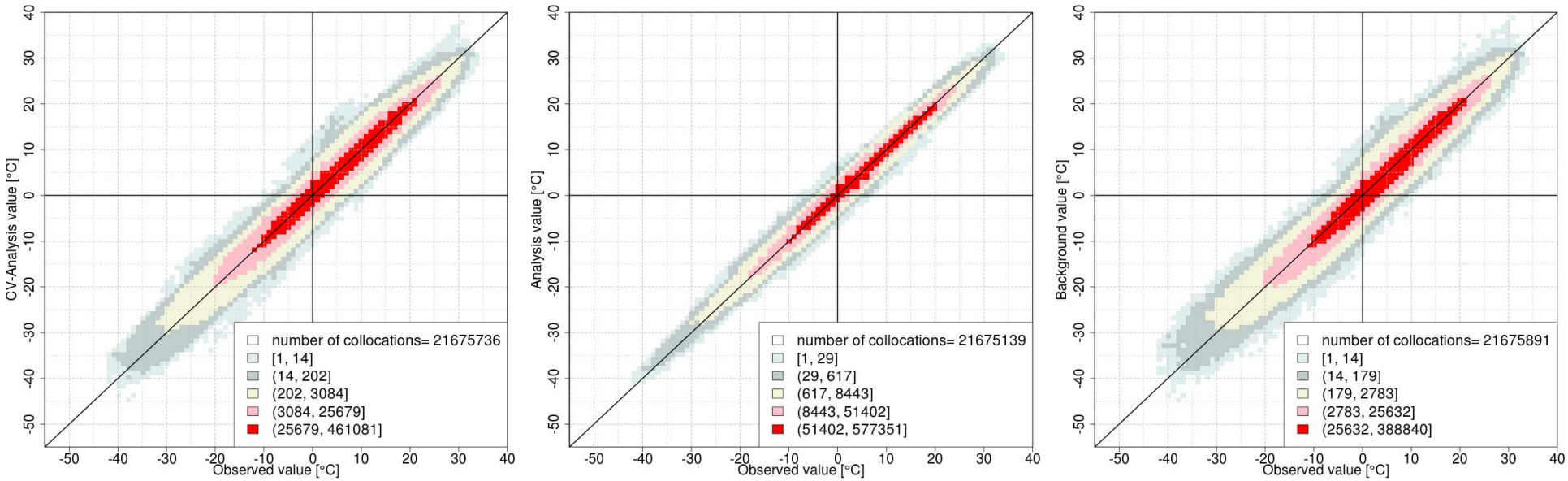

Figure 28: *TEMP1h*. Density plots of: (left) CV-analysis *vs* observations; (central) analysis *vs* observations; (right) background *vs* observations, for years 2010-2015. The shading indicates the number of pairs (or collocations) within each 1°C by 1°C cell and the total number of collocations is reported in the legend.

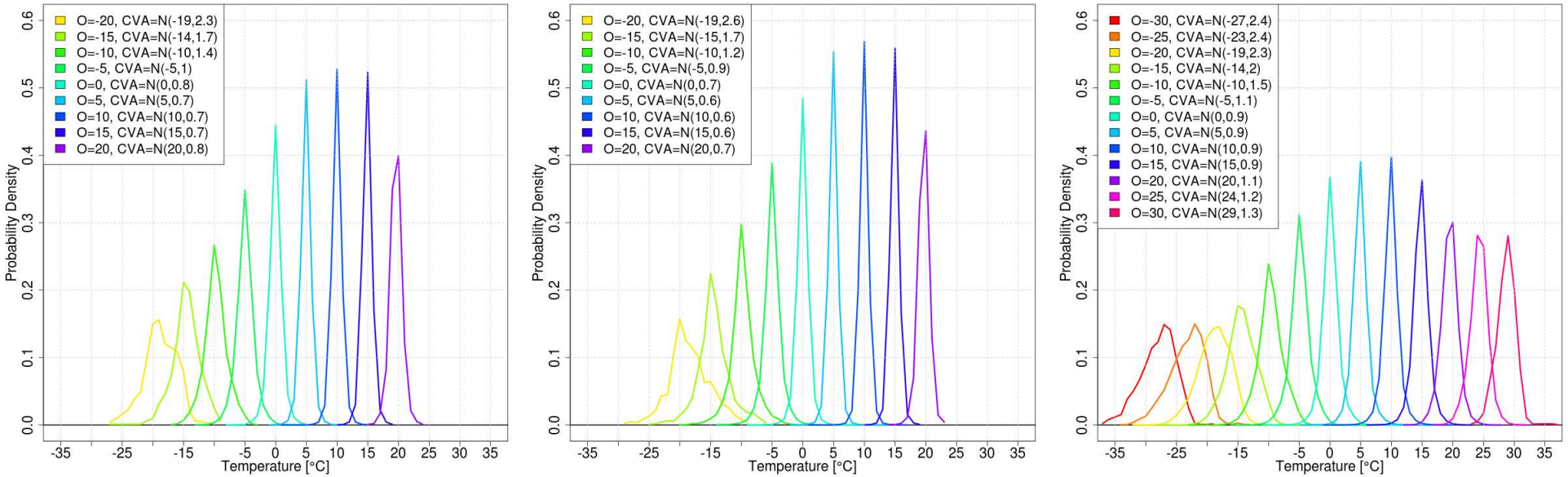

Figure 29: *TEMP1d* (left), *TEMP1d24h* (central) and *TEMP1h* (right). Empirical conditional probability density function for the CV-analysis given the observed value *O*, for years 2010-2015.

5.2 Variations of accuracy and precision of the analysis in time

The evolution in time of the accuracy and precision of the different products *TEMP1d*, *TEMP1d24h* and *TEMP1h* is illustrated in Figs. (31)-(36).

The accuracy of CV-analysis, analysis and background as estimates of the true temperature state is shown by the time series of the bias of the diagnostic variables: O-CVA, O-A and O-B. The corresponding precision of the estimates is given by the root mean square deviations of the diagnostic variables (see the introduction of Sec. 5).

The results are consistent with the outcomes of the evaluation based on the density plots. For *TEMP1d* and *TEMP1h*, the spatial interpolation provide up to ten times more accurate estimates of the true atmospheric state compared to the background, as can be seen from Figs. (31) and (33) by comparing the O-CVA bias with the O-B bias.

Basically, both the CV-analysis and the analysis can be assumed as unbiased estimates of the true temperature.

The CV-analysis and analysis precisions are shown in Figs. (34)- (36): for the *TEMP1h* analysis (CV-analysis) it is around $1\,^{\circ}$C ($1.5\,^{\circ}$C); for the *TEMP1d* analysis (CV-analysis) it is around $0.8\,^{\circ}$C ($1.1\,^{\circ}$C). The analysis precision depends on the season: in winter, when local weather phenomena play a more important role than in other seasons, the analysis is on average a less precise estimate than in summer.

Our choice of keeping constant values for the OI parameters of all the products and for the entire period under examination yields a rather stable precision for analysis, CV-analysis and background estimates throughout the whole period.

In the case of *TEMP1d*, the time series for the bias shown in Fig. (31) is remarkably stable for all the diagnostic variables from year 1957 to years 2005-2006, then there is a general reduction in the bias values. Because of this reduction is present in the background too, the increase in the accuracy of the estimates is most likely the effect of a variation in the MET Norway network management or in the quality control system. The precision of the *TEMP1d* estimates as shown in Fig. (34) is stable for the whole period and it seems to be more influenced by climatic conditions than other factors. In fact, the higher values of the root mean square deviations, which are reported for years around 1980, are in correspondence with the occurrence of rather cold winter seasons.

In the case of *TEMP1h*, the gradual increase in the number of stations reporting hourly measurements results in: a more accurate analysis and CV-analysis estimates, as can be seen in Fig. (33); a slightly more precise analysis and CV-analysis estimates, as can be

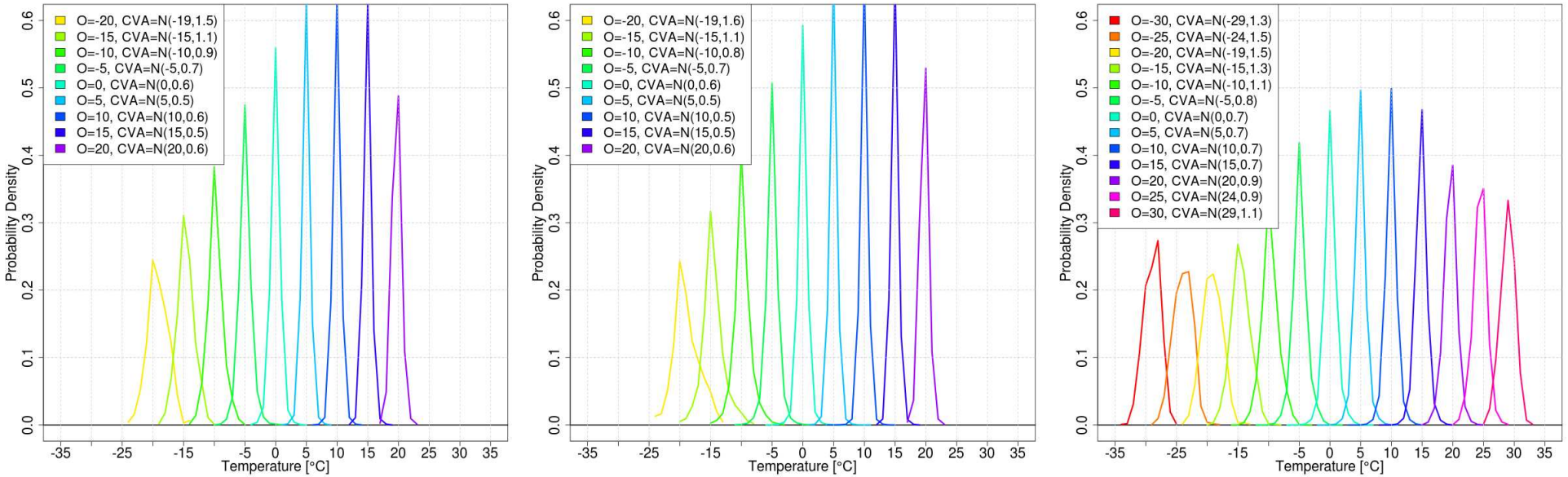

Figure 30: *TEMP1d* (left), *TEMP1d24h* (central) and *TEMP1h* (right). Empirical conditional probability density function for the analysis given the observed value *O*, for years 2010-2015.

seen in Fig. (36) from the reduction in the amplitude for the seasonal cycle of the root mean square deviations.

The case of *TEMP1d24h* deserves a separate discussion. The O-CVA bias appears to be higher than the innovation bias, which in turn is rather small compared to the case of *TEMP1d*, as can be seen in Fig. (31) where *TEMP1d* and the *TEMP1d24h* are compared. To sum up, for *TEMP1d24h* the spatial interpolation rely on a more accurate background compared to the one available for *TEMP1d*, however we're not able to take advantage of it as demonstrated by our evaluation showing a comparable precision between *TEMP1d* and *TEMP1d24h* analysis. The OI configuration for *TEMP1d24h* must be modified. In fact, the background available for *TEMP1d24h* refers to the same fine scale of the analysis, as opposed to the background of *TEMP1d* which refers to a coarse scale than the analysis, as a consequence the OI decorrelation length scales used in the specification of the background error covariance matrices should be set to smaller values compared to the ones used for *TEMP1d*. Otherwise, the filter properties of the spatial interpolation scheme would regionalize the local signal present in the background resulting in an analysis very similar to the average of the *TEMP1h* fields (i.e. the background, for which the decorrelation length scales are actually optimized).

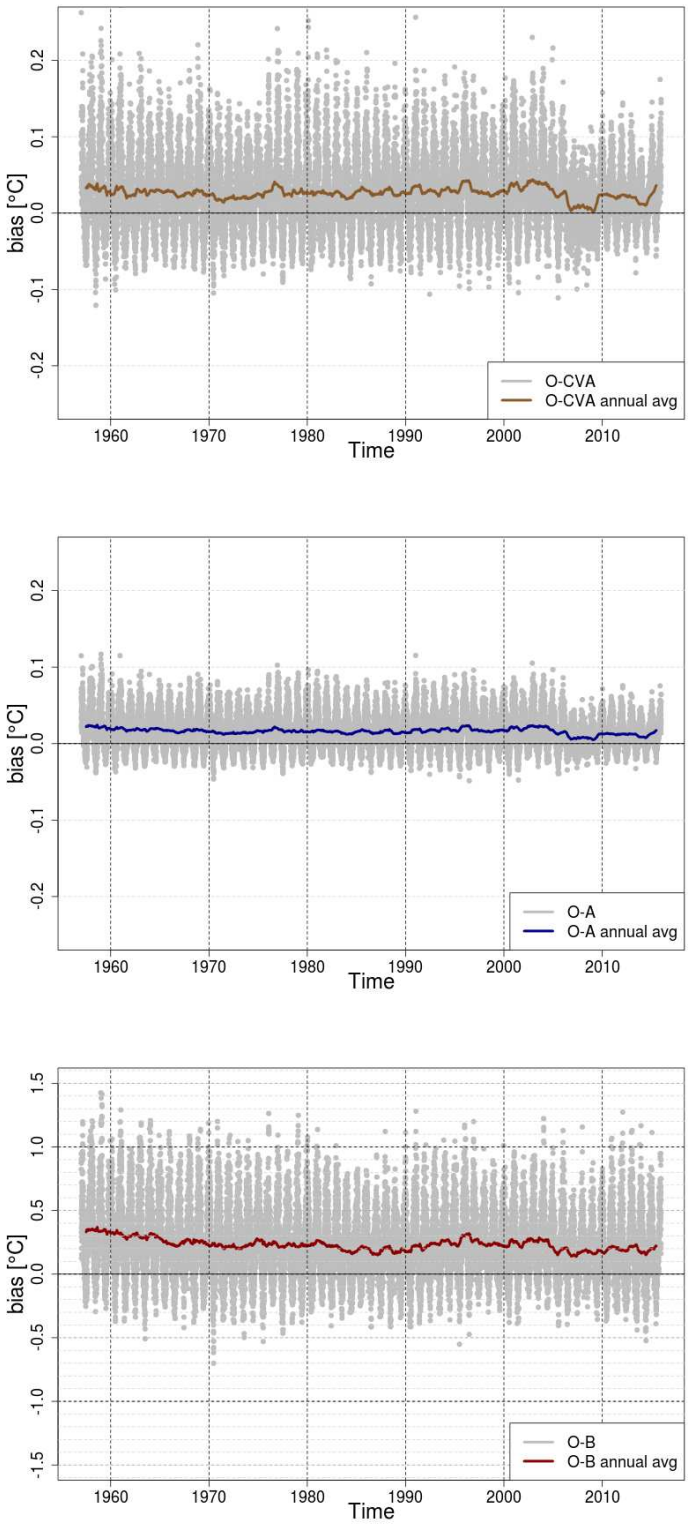

Figure 31: *TEMP1d.* time series of the daily bias of: (top) CV residual; (middle) analysis residual; (bottom) innovation, for years 1957-2015. Thick lines show the annual centered moving average.

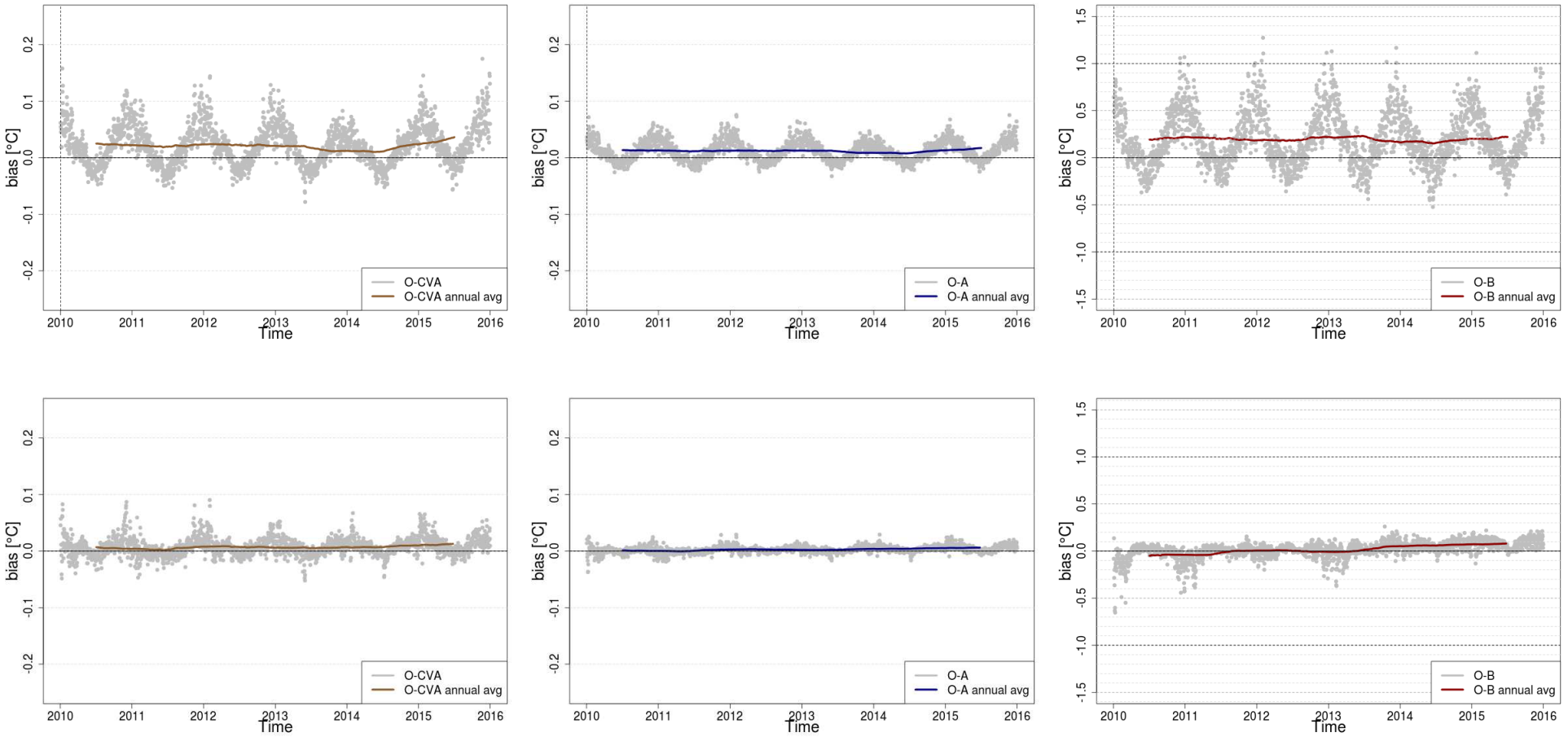

Figure 32: *TEMP1d* (top row) and *TEMP1d24h* (bottom row). time series of the daily bias of: (left) CV residual; (central) analysis residual; (left) innovation, for years 2010-2015. Thick lines show the annual centered moving average.

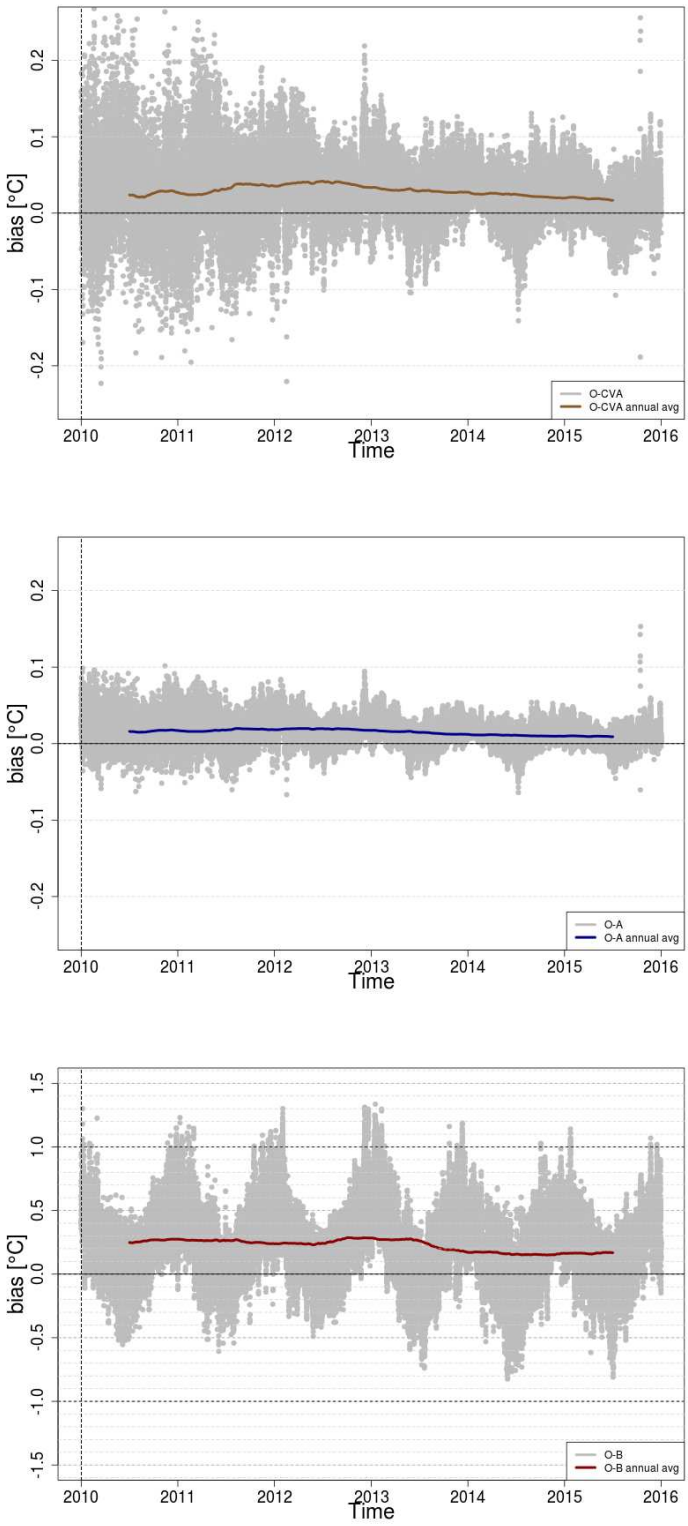

Figure 33: *TEMP1h.* time series of the hourly bias of: (top) CV residual; (middle) analysis residual; (bottom) innovation, for years 2010-2015. Thick lines show the annual centered moving average.

5.3 Typical year and seasonal variability

As reported in the previous Section, the analysis is an accurate estimate of the true temperature state. In this Section, we focus on the study of the seasonal variability for the precision of the analysis and background estimates by computing the typical year for O-CVA, O-A and O-B. The daily time series for bias and RMSE are shown in Figs. (31)-(36). The typical year for a diagnostic variable is obtained by averaging the corresponding daily values and it is shown in Figs. (37) and (38).

As stated previously in our evaluation: the analysis precision is higher in the summer and up to two-three times smaller in winter both for grid points and station locations. Once again, it is quite evident that we have some problem in *TEMP1d24h*, because the background at grid points is a more precise estimate of the true temperature than the CV-analysis (i.e. the root mean square deviation for O-CVA is greater than for O-B).

The average difference between daily and hourly precision in the analysis estimates is illustrated in Fig. (37). In particular, it appears that the precision for hourly analysis shows a reduced annual variability compared to the daily analysis: during the summer it is possible to recognize a drop in the root mean square deviation values in the daily analysis, which is less evident in the hourly analysis; during the winter, on average the hourly and daily analysis precisions are rather similar, except for extremely cold temperatures when the hourly analysis precision can reach $2.4\,^{\circ}$C while for the daily values the upper limit in the worst cases is about $2.\,^{\circ}$C.

Given the availability of the sub-daily temperature analysis *TEMP1h*, it is possible to compute the daily cycle for the accuracy and the precision of the analysis and background estimates as shown in Figs. (39)-(40). The winter season and the summer seasons are considered separately. The average bias is shown in Fig. (39) and it is very close to $0.\,^{\circ}$C, nonetheless it is interesting to register the different behaviour in the background bias between winter and summer.

The average root mean square deviation for each hour of a typical day in shown in Fig. (40). First, we found a further confirmation that the analysis scheme yields more precise estimates for the summer than for the winter. Second, for the winter the analysis precision is higher during daytime and smaller during nighttime, most likely because of the occurrence of ground-based temperature inversions in the vertical profile of temperature, which are more frequent during the night and in general more difficult to represent in the analysis. In the summer season, it is quite interesting to note that the analysis is

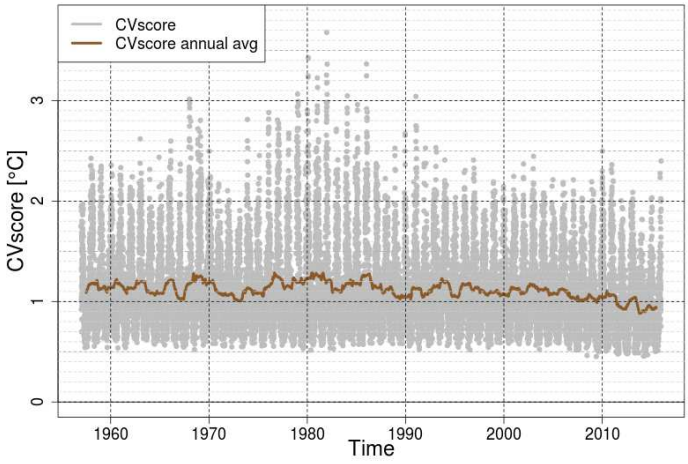

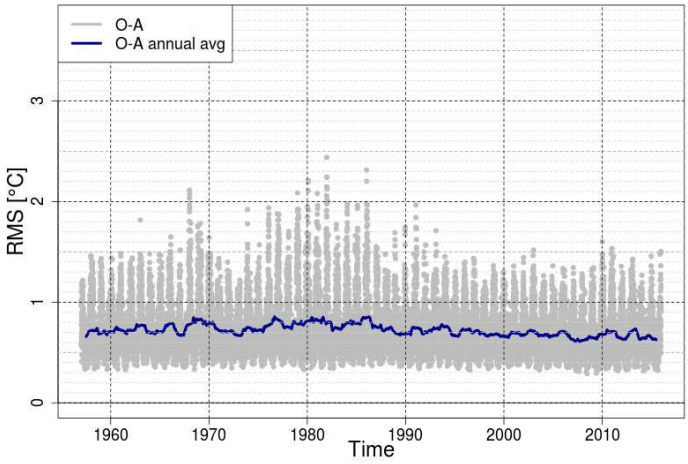

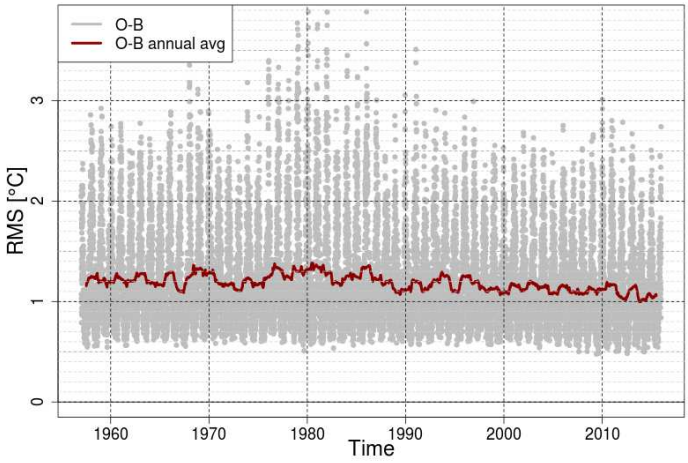

Figure 34: *TEMP1d*. time series of the daily root mean square deviations of: (top) CV residual; (middle) analysis residual; (bottom) innovation, for years 1957-2015. Thick lines show the annual centered moving average.

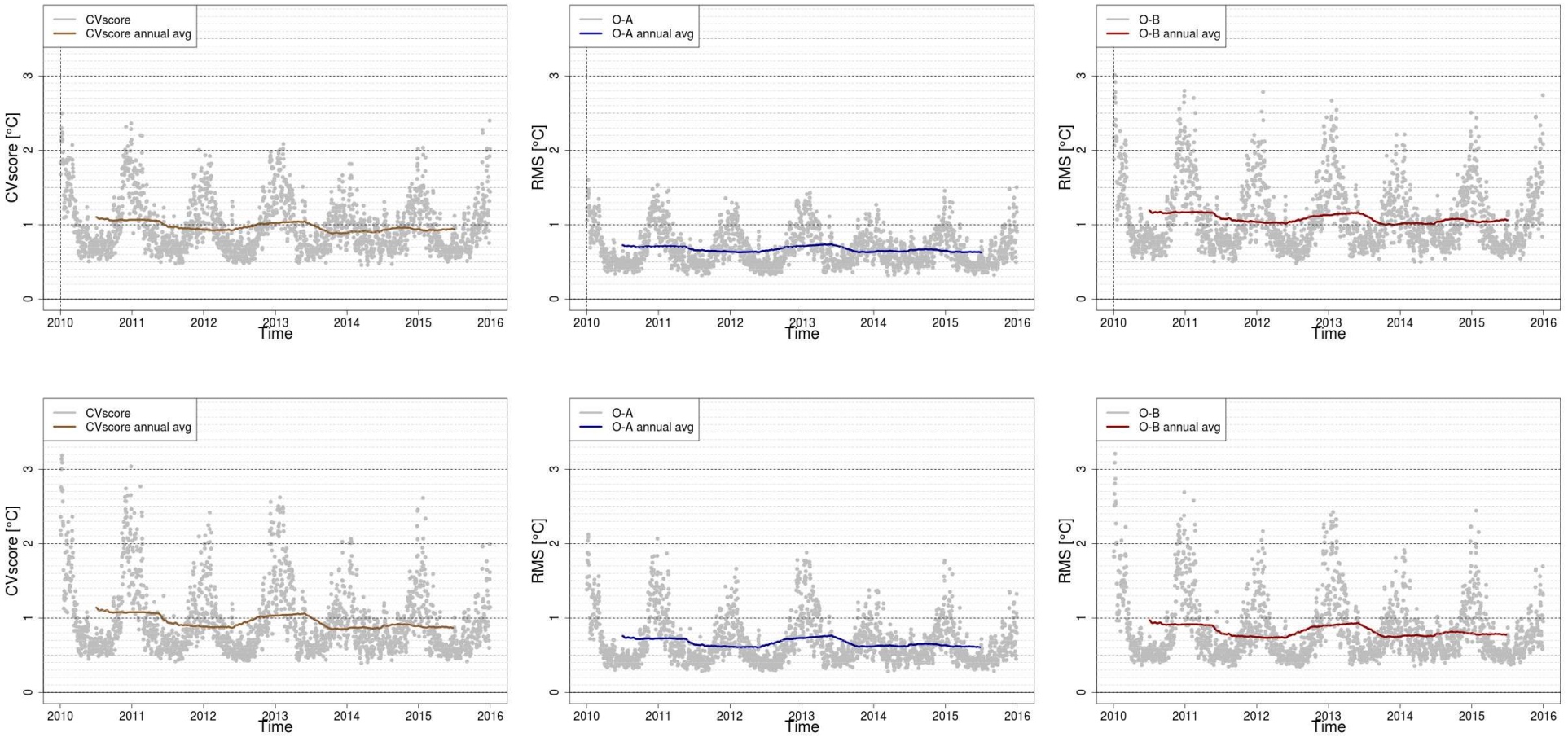

Figure 35: *TEMP1d* (top row) and *TEMP1d24h* (bottom row). time series of the daily root mean square deviations of: (left) CV residual; (central) analysis residual; (left) innovation, for years 2010-2015. Thick lines show the annual centered moving average.

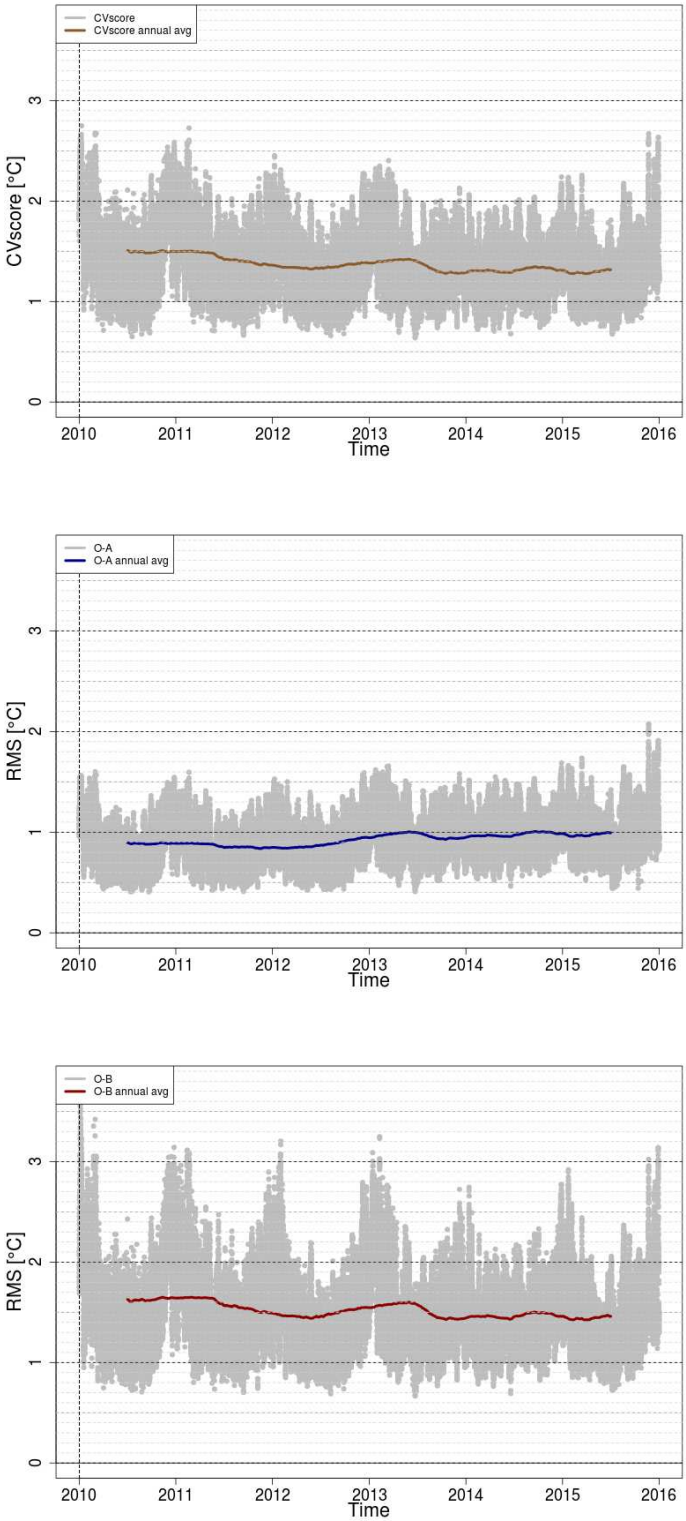

Figure 36: *TEMP1h*. time series of the hourly root mean square deviations of: (top) CV residual; (middle) analysis residual; (bottom) innovation, for years 2010-2015. Thick lines show the annual centered moving average.

more precise during sunset and sunrise hours when on average the atmosphere is more stable (i.e. energy exchanges due the turbulent motions are less intense).

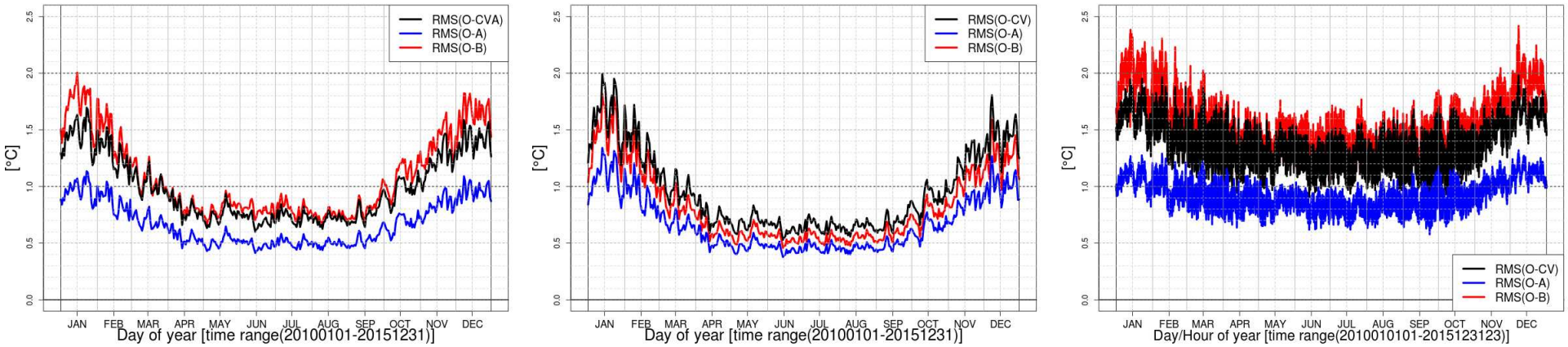

Figure 37: *TEMP1d* (left), *TEMP1d24* (central), *TEMP1h* (right). average root mean square for each day (hour for *TEMP1h*) of the year of: CV residual (black); analysis residual (blue); innovation (red), for years 2010-2015.

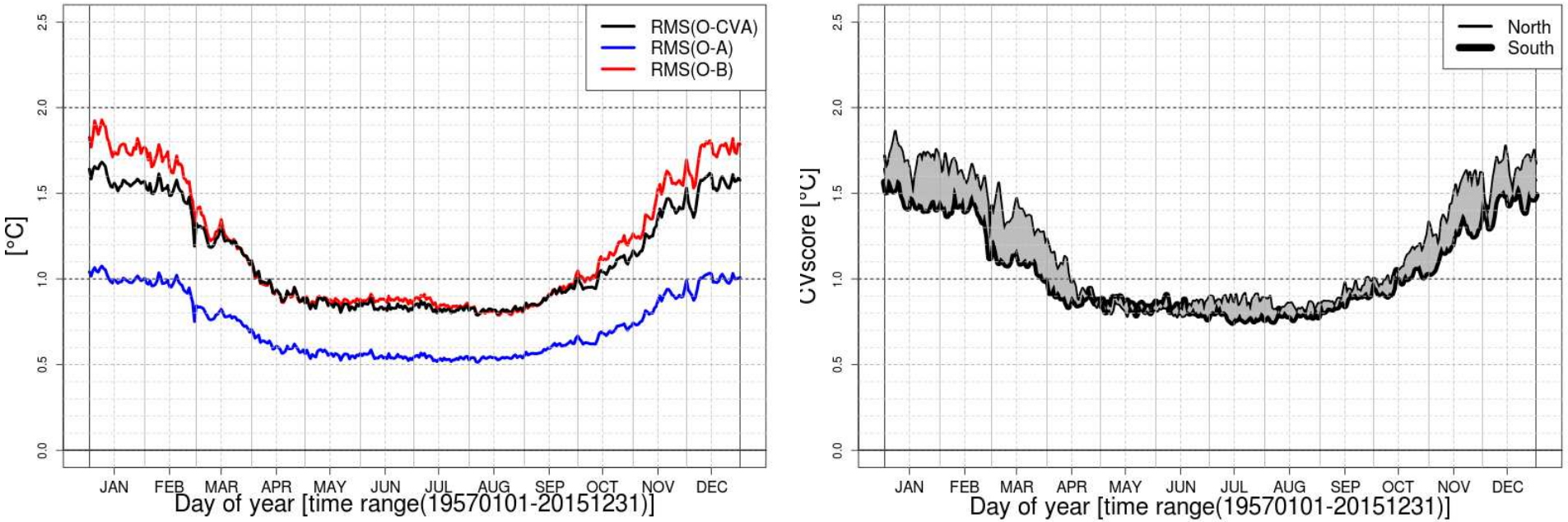

Figure 38: *TEMP1d*. average root mean square for each day of the year of: CV residual (black); analysis residual (blue); innovation (red), for years 1957-2015. In the right panel, Northern and Southern Norway have been considered separately.

5.4 The effects of station density variations in time and space

In this Section we focus on the impact that the variations in time and in space of the station network collecting the observations have on the analysis quality.

In Figs. (1), (3) and (5), the variation in time of the number of observations used for each analysis step is illustrated. The Integral Data Influence (IDI) has been used to investigate the impact of the variation in the station network, prescribed our fixed OI configuration, on the analysis quality both at grid points and at station locations. Remember that a point having an IDI value close to 1 would be influenced in the OI by the neighbouring innovation values. On the other hand, a point having an IDI value significantly less than 1, or in other words a CVIDI close to 0, would result in an analysis value equal to the background value (see Sec. 3.3.2).

The IDI and CVIDI are shown in Figs. (41)-(43) and (45) for the different products. The $\overline{CVIDI}$ time series is shown in Fig. (41) for *TEMP1d*, which is valid also for *TEMP1d24h* because both products are based on the same set of daily observations, and for *TEMP1h*. The variations in the $\overline{CVIDI}$ follow the station network evolution in time and its average value over the whole domain are at acceptable values. For *TEMP1d*, on average the $\overline{CVIDI}$ value is between 0.85 and 0.90, with a sharp increase for recent years. For *TEMP1h*, the $\overline{CVIDI}$ is gradually increasing from 0.8 to a value between 0.90 and 0.95 in 2015.

The IDI spatial distribution is illustrated for *TEMP1h* in Fig. (43), as an average over one year together with the corresponding standard deviation, and for *TEMP1d* in Fig. (45) only as an average over one year because the standard deviation was not significant.

In general, the Norwegian areas where the analysis values would remain closer to the background values without any particular benefit from the spatial interpolation procedure are: the mountain areas, and the highest peaks specifically; the areas along the borders especially for years where the station density results to be lower than its average value (i.e., for *TEMP1d* around 2005; for *TEMP1h* in 2010-2011).

Consider the availability of data from stations located outside Norway. In the case of *TEMP1d*, the data has not been used for the years previous to 2015 for it becomes available in KDVH after our evaluation. In the case of *TEMP1h*, the data is included from year 2010 onwards but its availability in KDVH is less stable in time than for the Norwegian data, as it can be seen from the higher standard deviations in Fig. (43).

The impact of station density on the analysis quality is reported in Fig. (42) by means

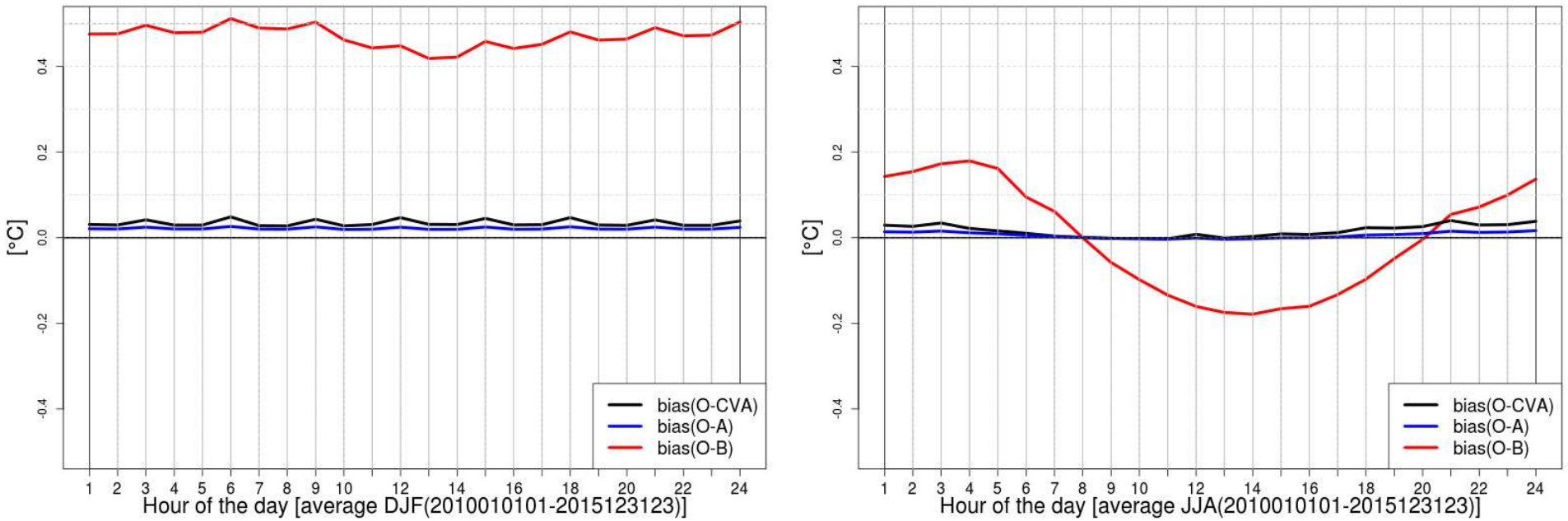

Figure 39: *TEMP1h*. average bias for each hour of the day of: CV residual (black); analysis residual (blue); innovation (red), for years 2010-2015: Winter (December-January-February, left); Summer (June-July-August, right).

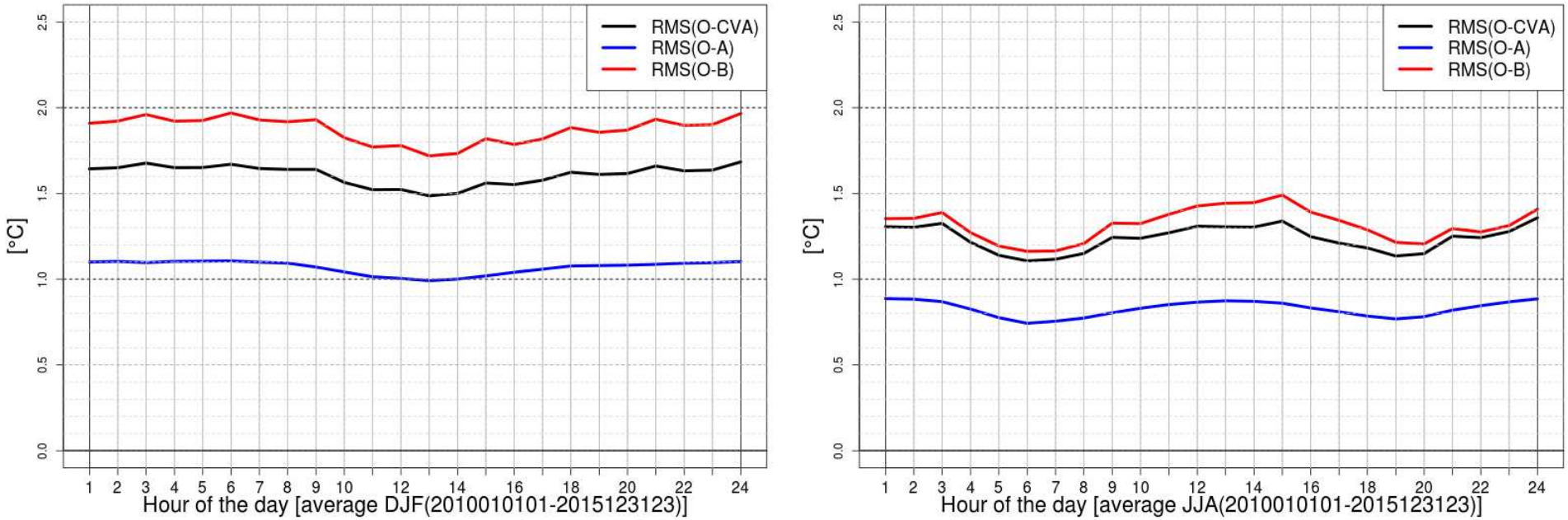

Figure 40: *TEMP1h*. average root mean square for each hour of the day of: CV residual (black); analysis residual (blue); innovation (red), for years 2010-2015: Winter (December-January-February, left); Summer (June-July-August, right).

of boxplots of the absolute value of the CV-residuals *vs* CVIDI for the winter and the summer seasons, which are considered separately, for years 2014-2015. Given that we're considering CVIDI and CV-residuals, our evaluation is valid for grid points even thought it has been conducted at station locations. The local station density in the surroundings of a grid point is represented by the CVIDI, which has been divided in three classes: $CVIDI < 0.45$ indicates isolated grid points, $CVIDI > 0.85$ includes the vast majority of the grid points which are strongly influenced by spatial interpolation, then an intermediate transition class in present between those two classes. In the case of *TEMP1d*, in general the precision of the analysis at grid points increases with the increase in station density and for grid points having $IDI < 0.45$ we should expect the median of the distribution for the absolute value of the CV-residuals to be around $0.5\,^{\circ}\mathrm{C}$ both in winter and in summer, when in addition the distribution is less disperse. In the case of *TEMP1h*, the situation is similar to *TEMP1d* with the difference that *TEMP1h* is characterized by a smaller precision, especially for isolated grid points. Once again, *TEMP1d24h* stands out for its peculiar performances: the two classes representing the denser station density areas behave like the equivalent classes for *TEMP1d*, instead for isolated grid points the best precision is achieved. That is, the background is indeed a good approximation of the true temperature state even for isolated areas whereas the spatial interpolation scheme would be revised for this product.

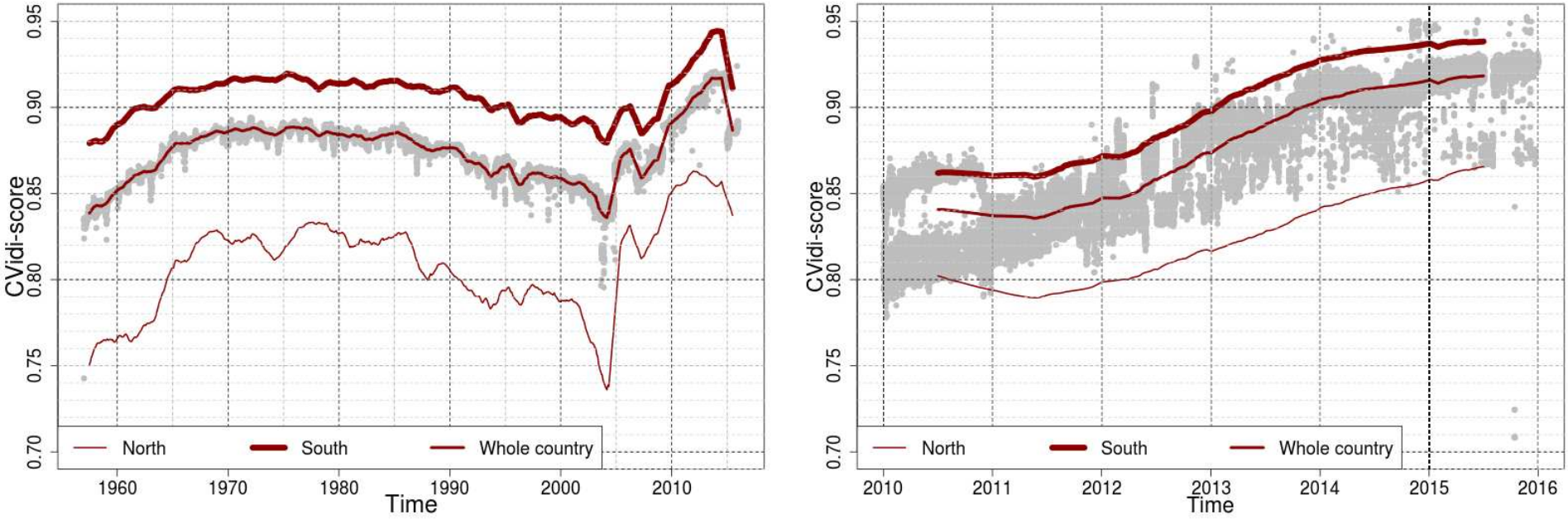

Figure 41: *TEMP1d* (left), *TEMP1h* (right). $\overline{CVIDI}$ time series.

5.5 Analysis increments

Our study of the analysis increments (i.e. analysis minus background) aims at investigating the effects on the analysis of using our global pseudo-background field. In fact, the analysis increment averaged over a long time period should be everywhere close to zero. However, any violation of our assumption on the background being an unbiased estimate of the true temperature state would result either in the presence in the analysis increment averaged field of areas showing positive/negative values (i.e. corresponding to positive/negative systematic corrections of the analysis field) or in areas exhibiting an unusually high/low variability in the sequence of the analysis increment fields.

In Figs. (44),(46)-(49) and (50), the analysis increment field is shown for the different products as an average either over a single year or over the winter months within a single year. The winter season is considered independently because of the presence of inversions in the vertical profile of temperature, which introduce important local features thus making the blending of regional pseudo-background fields more problematic.

The years 2011 and 2015 have been chosen to perform an inter-comparison between *TEMP1h*, *TEMP1d* and *TEMP1d24h*. In the case of *TEMP1d*, in addition to years 2011 and 2015 we considered also: 1957 as the beginning of the time period; 1979 as one of the coldest year, especially in winter; 1990 is representative of a typical year; 2003 as a year characterized by a decrease in the observation availability.

The fields of the analysis increment averaged over one year are in general rather uniform and they don't show the presence of significant systematic corrections.

In winter, when the atmospheric situation is much more challenging for the pseudo-background blending procedure, the analysis increment averaged field become "patchy" showing an alternation of areas characterized by positive and negative systematic corrections; the size of each area being compatible with the size of a single regional pseudo-background field.

However, the overall effect on the analysis is in general limited between $-1.5\,^{\circ}$C and $1.5\,^{\circ}$C, especially for *TEMP1h* and *TEMP1d24h*. For *TEMP1d*, during the cold winters -such as the in 1979- we have areas where the systematic corrections reach the absolute value of $2.5\,^{\circ}$C.

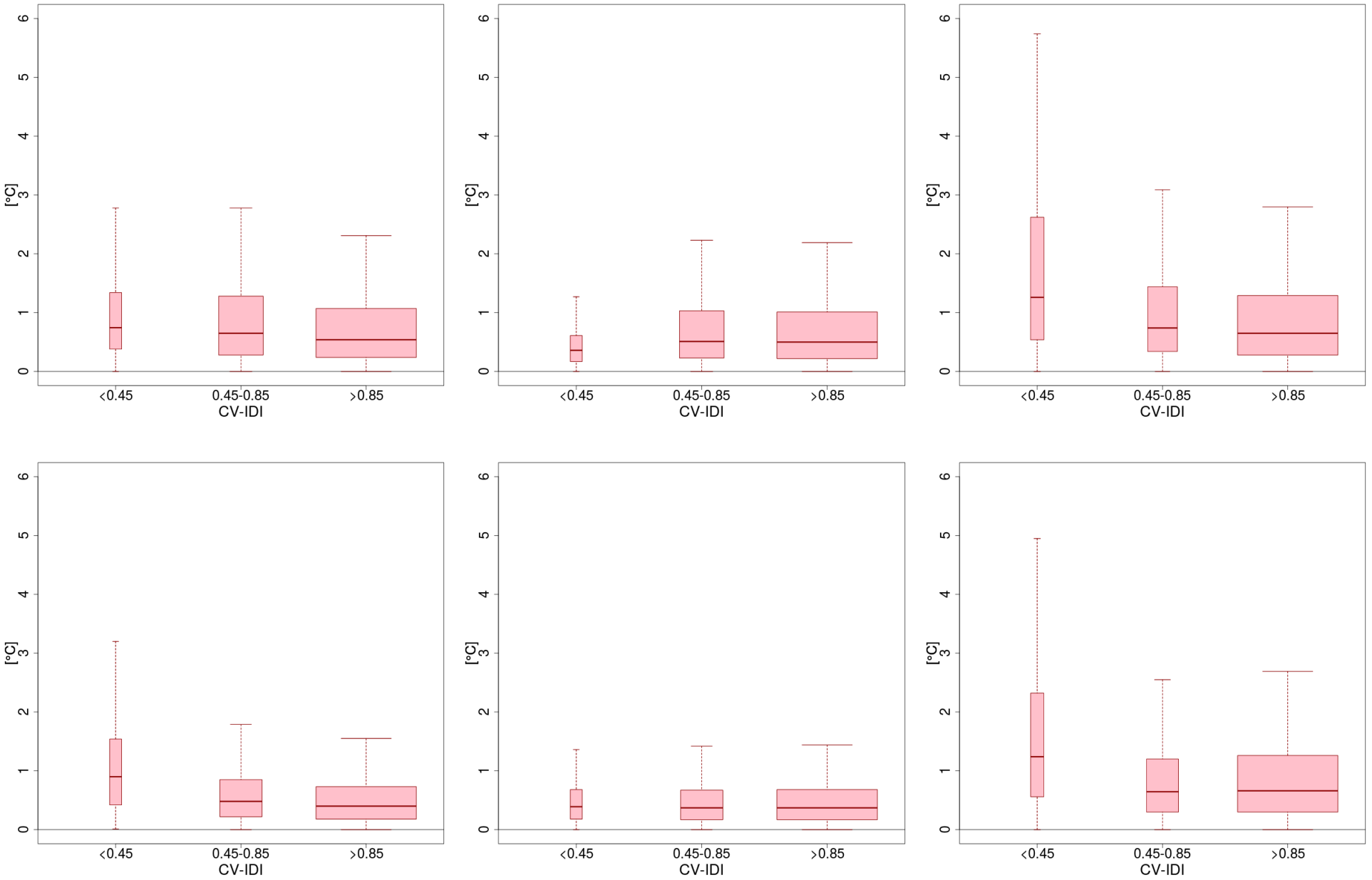

Figure 42: *TEMP1d* (left), *TEMP1d24h* (central) and *TEMP1h* (right). Box-plot of absolute values of CV residuals versus CV-IDI, for 2014-2015: Winter (top), Summer(bottom).

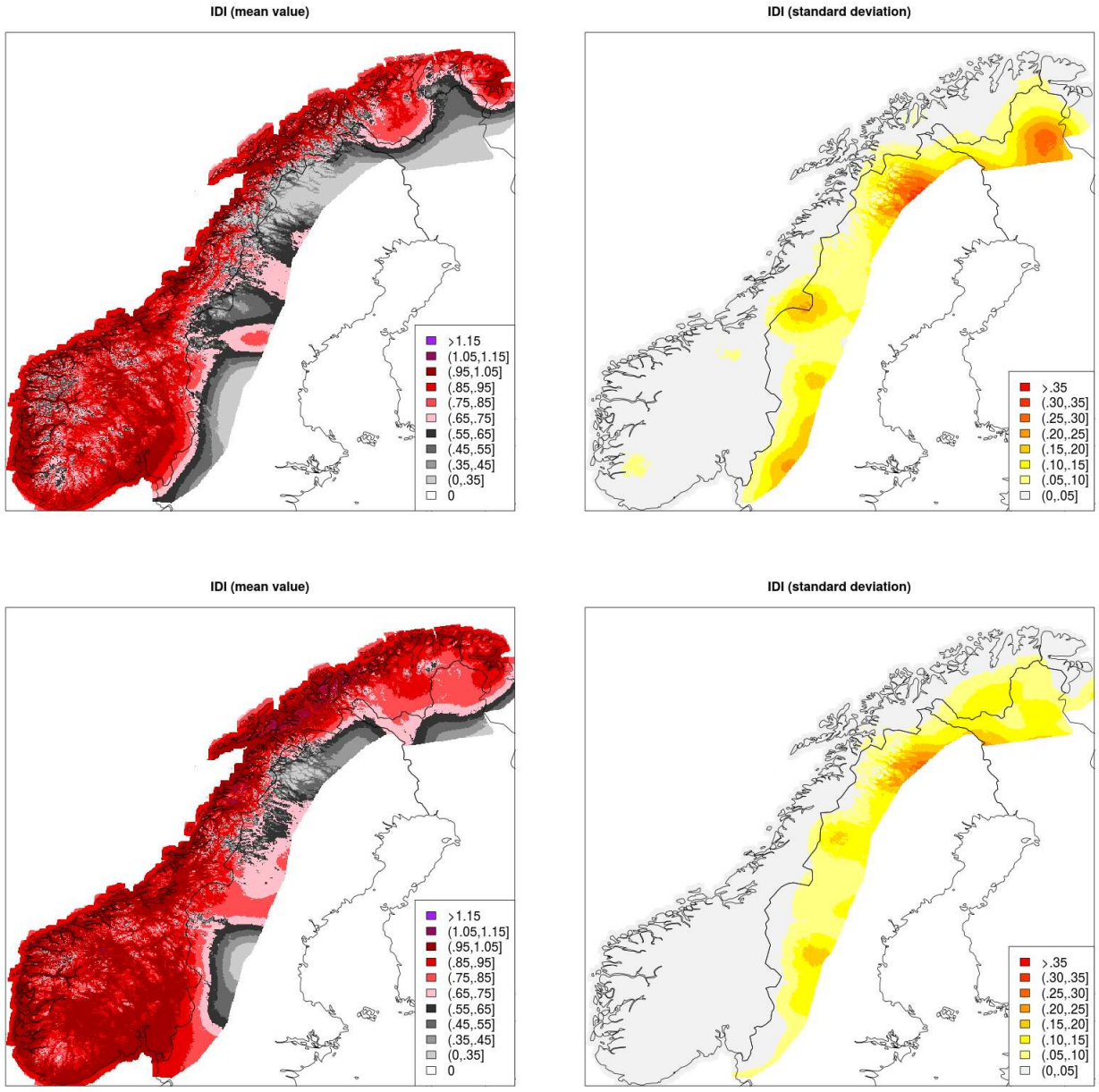

Figure 43: *TEMP1h* IDI. (top-left) annual mean field and (top-right) annual standard deviation field for year 2011. (bottom-left) annual mean field and (bottom-right) annual standard deviation field for year 2015.

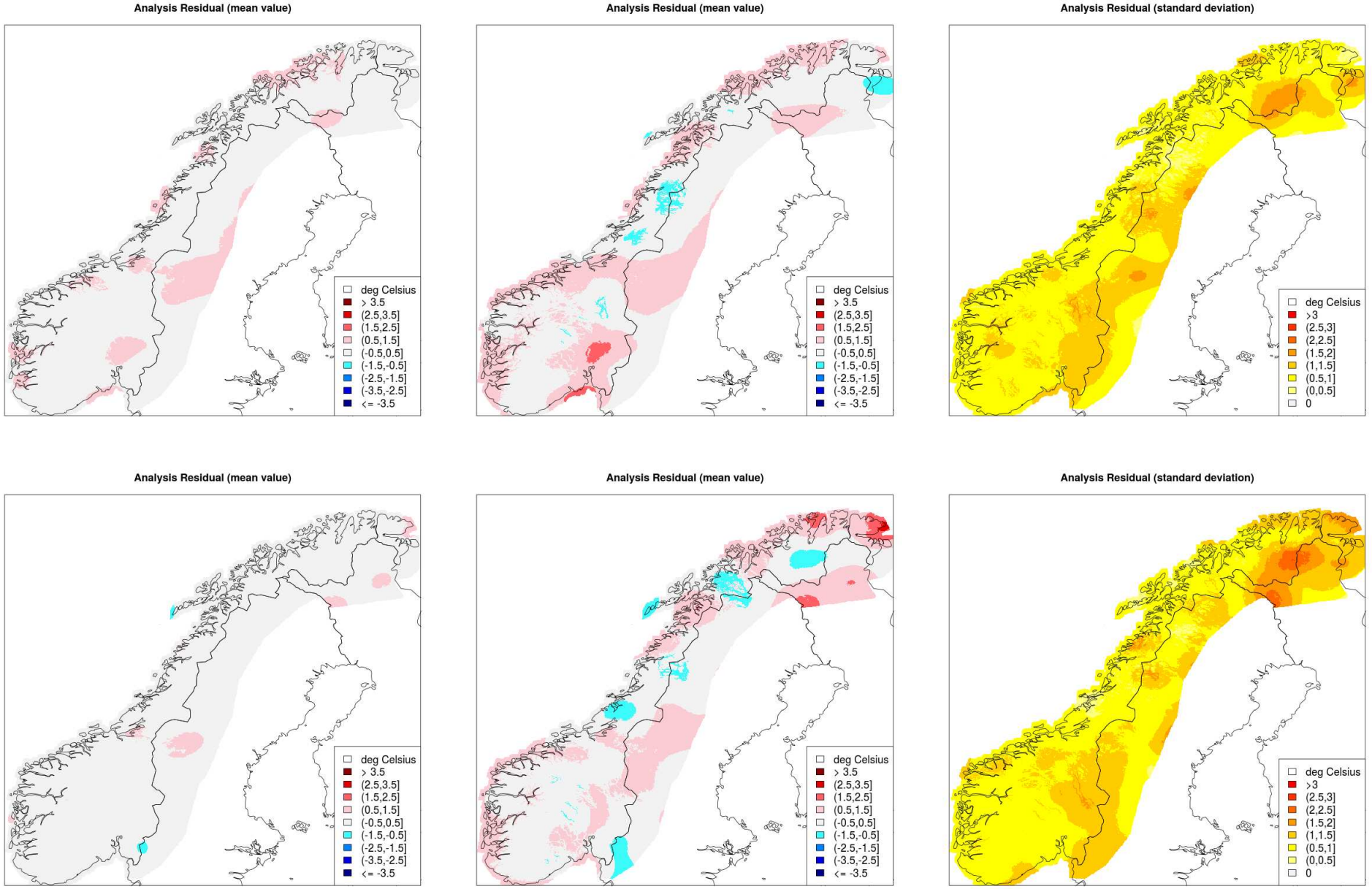

Figure 44: *TEMP1h* analysis increment. (top-left) annual mean field for year 2011; (top-central) mean field for January-February-December 2011; (top-right) standard deviation field for January-February-December 2011. (bottom-left) annual mean field for year 2015; (bottom-central) mean field for January-February-December 2015; (bottom-right) standard deviation field for January-February-December 2015.

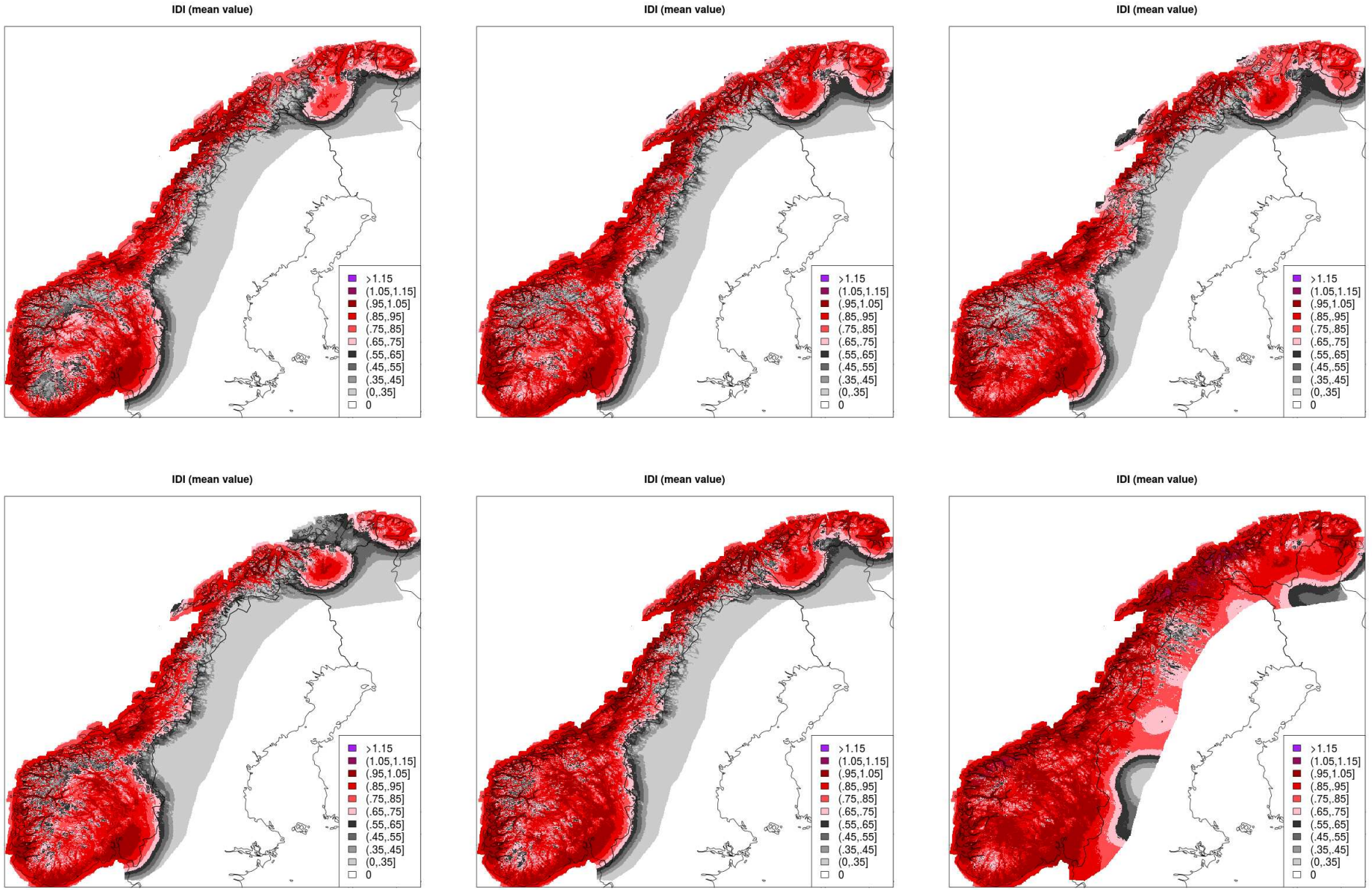

Figure 45: *TEMP1d* IDI. Annual mean field for years: 1957-1979-1990 (top row, left to right); 2003-2011-2015 (bottom row, left to right).

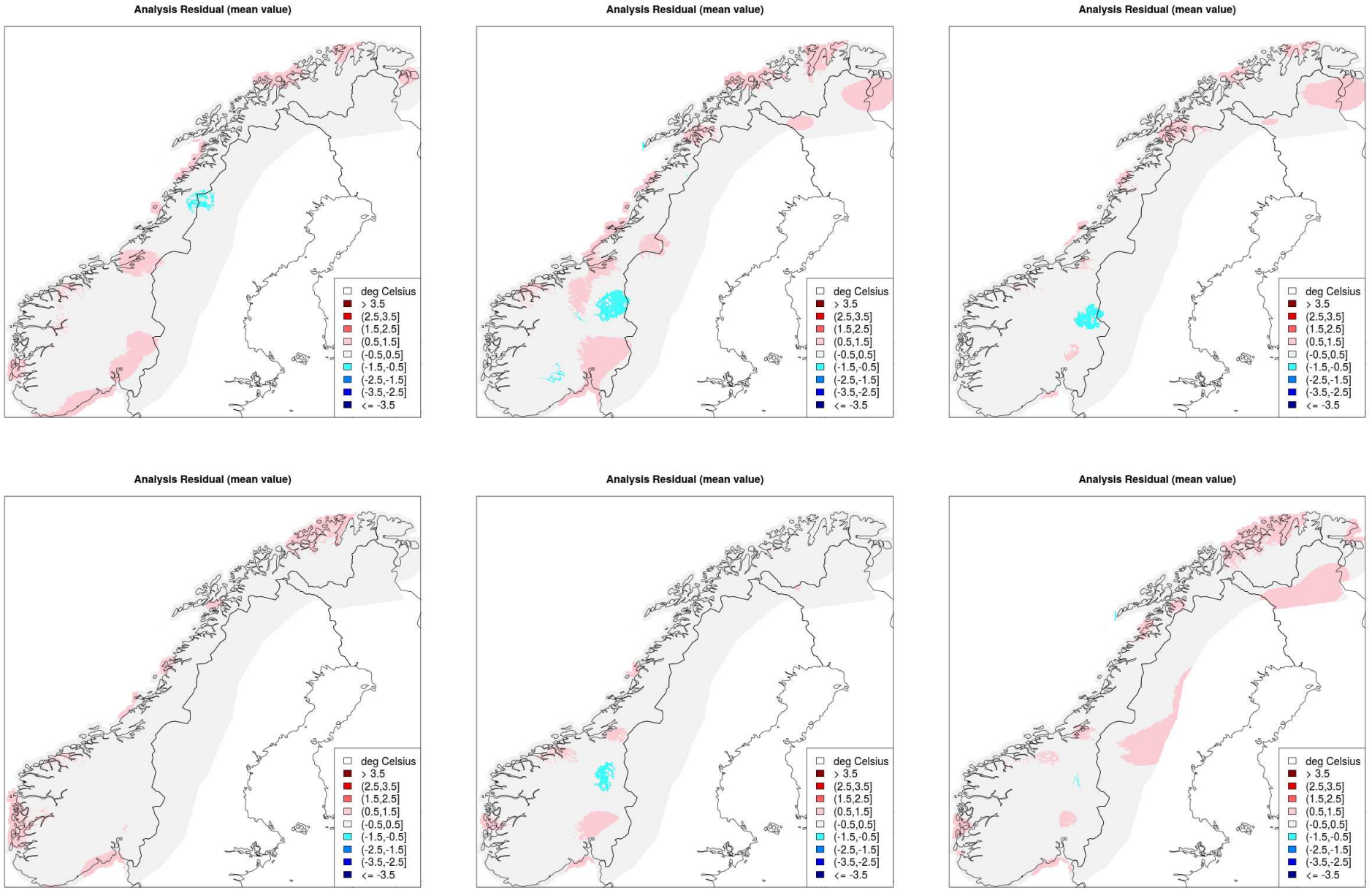

Figure 46: *TEMP1d* analysis increment. Annual mean field for years: 1957-1979-1990 (top row, left to right); 2003-2011-2015 (bottom row, left to right).

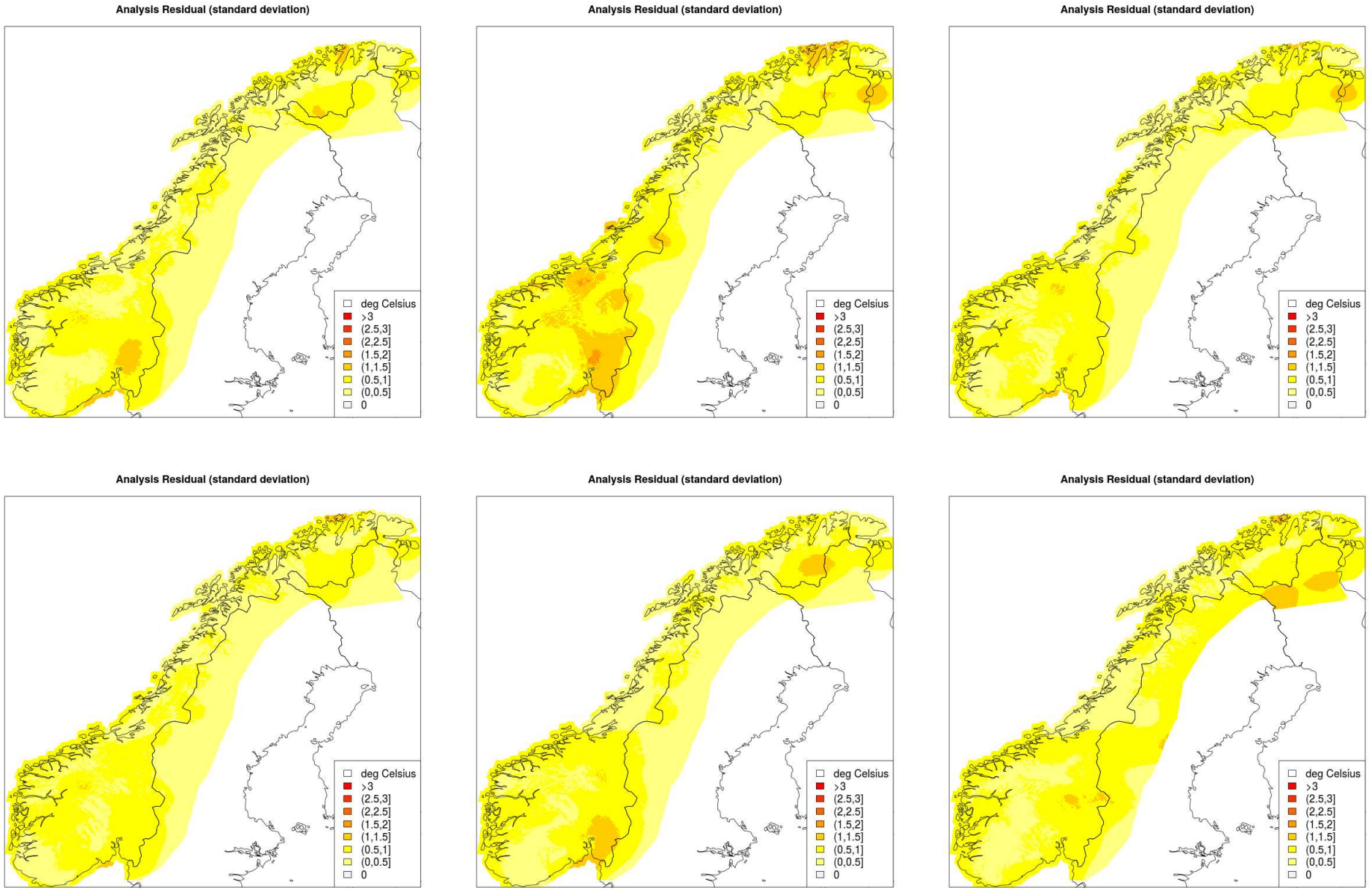

Figure 47: *TEMP1d* analysis increment. Annual standar deviation field for years: 1957-1979-1990 (top row, left to right); 2003-2011-2015 (bottom row, left to right).

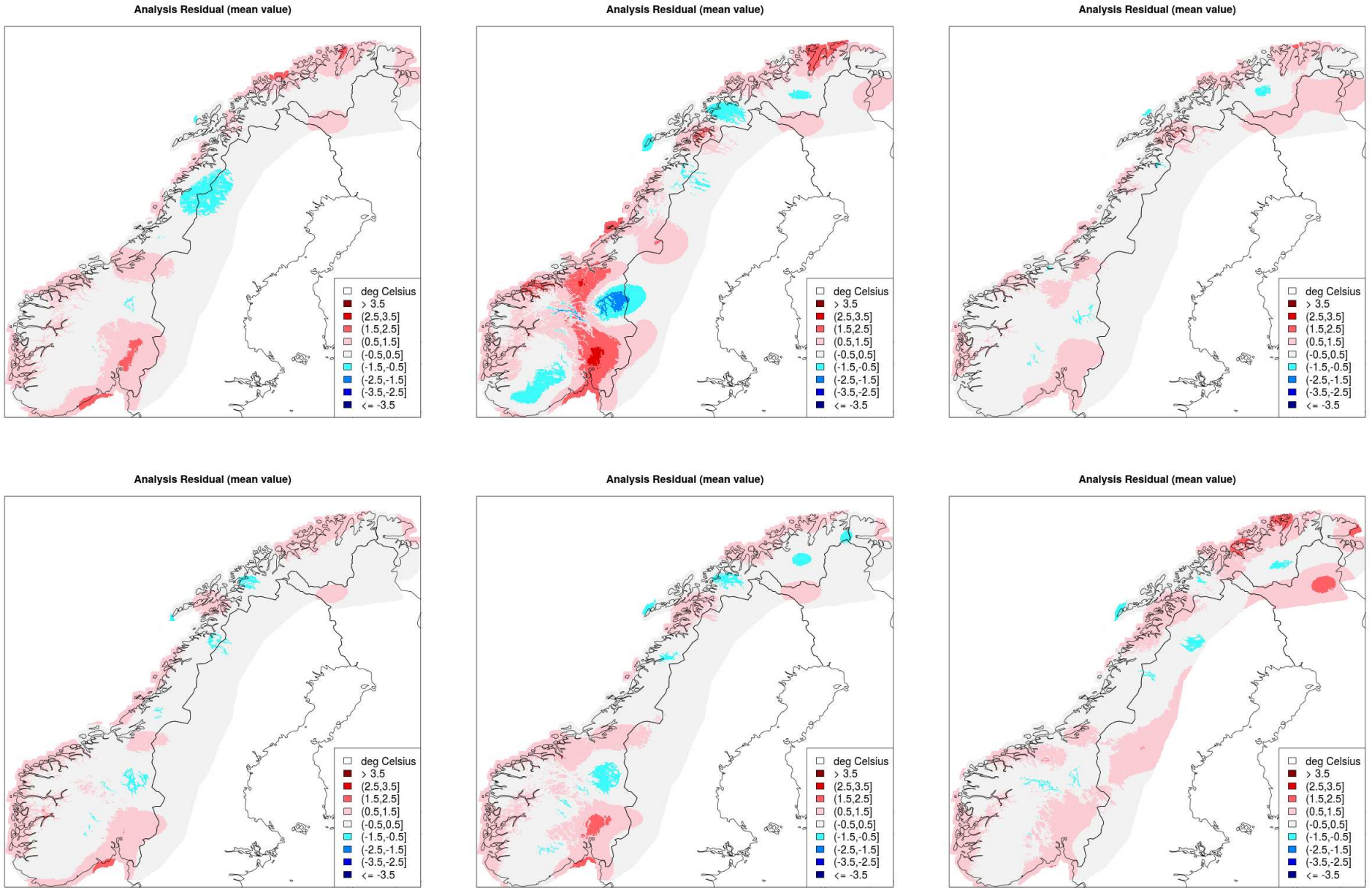

Figure 48: *TEMP1d* analysis increment. Mean field for January-February-December: 1957-1979-1990 (top row, left to right); 2003-2011-2015 (bottom row, left to right).

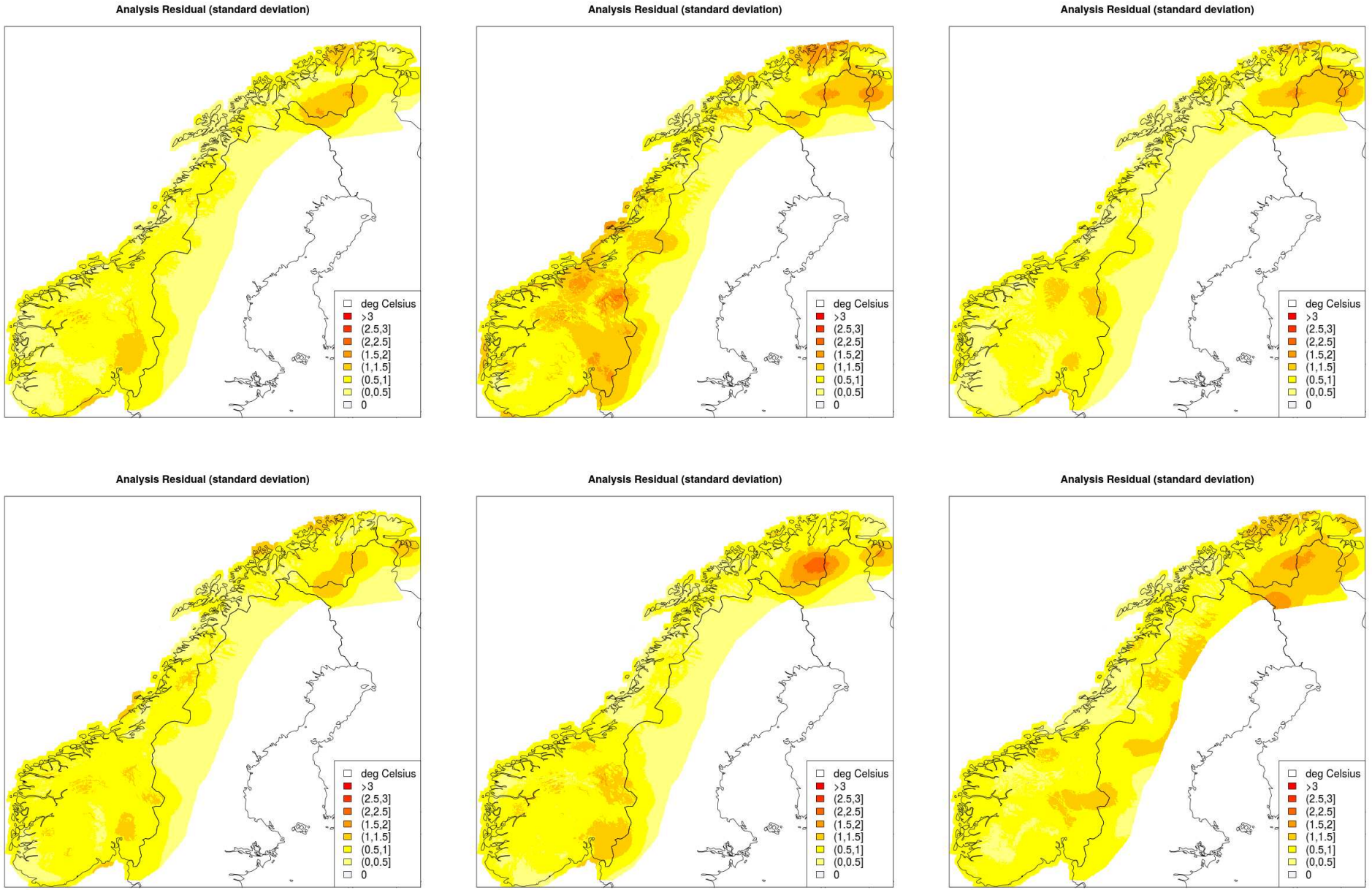

Figure 49: *TEMP1d* analysis increment. Standar deviation field for January-February-December: 1957-1979-1990 (top row, left to right); 2003-2011-2015 (bottom row, left to right).

6 Conclusions

The *seNorge2* observational gridded dataset for hourly and daily temperature includes the two main products: *TEMP1h*, *TEMP1d* and the experimental product *TEMP1d24h*.

The observations used for *seNorge2* are stored in the MET Norway's Climate Databases (KDVH) and both the station network density and the quality control system implemented at MET Norway are sufficient to provide the final user with spatial interpolation products of reasonable quality all over the Norwegian mainland for the time range: from 2010 onwards for *TEMP1h*; from 1957 onwards for *TEMP1d*. The products are regularly updated.

A spatial interpolation procedure for hourly and daily temperature values based on Bayesian concepts and relying on observations only has been implemented at MET Norway. The spatial interpolation method is based on statistical interpolation: the classical Optimal Interpolation (OI) scheme has been modified taking into account a scale-separation approach. In particular, a global pseudo-background field is introduced in the OI. The global pseudo-background field is obtained by blending several regional pseudo-background fields, each of them derived by observation de-trending. The presence of (small) discontinuities in the global pseudo-background field introduced by the blending procedure field has a limited impact on the analysis quality. By construction, the OI configuration is fixed in time and we used the same parameter values for *TEMP1h*, *TEMP1d* and *TEMP1d24h* because the analysis statistics is required to be as much stable as possible over time and to facilitate the intercomparison between different products.

Several diagnostics variables have been computed to monitor the statistical interpolation performances and to assess the quality of the final analysis fields. In particular, the concepts of: leave-one-out cross-validation and Integral Data Influence have been introduced.

The analysis can be regarded as an unbiased estimate of the true temperature both at grid points and at station locations. Only for the most extreme negative values (values below $-30\,^{\circ}$C) the evaluation suggests the presence of a systematic warm bias in all the products. The analysis is a more precise representation of the truth for positive temperature values than for negative values. The analysis statistics are reported in Tables 1 and 2, for grid points and station locations respectively.

A Spatial Consistency Test (SCT) has been included in the OI scheme to prevent observations affected by gross-measurements errors from entering the spatial interpolation procedure. The SCT is a key component of the spatial interpolation procedure, because it

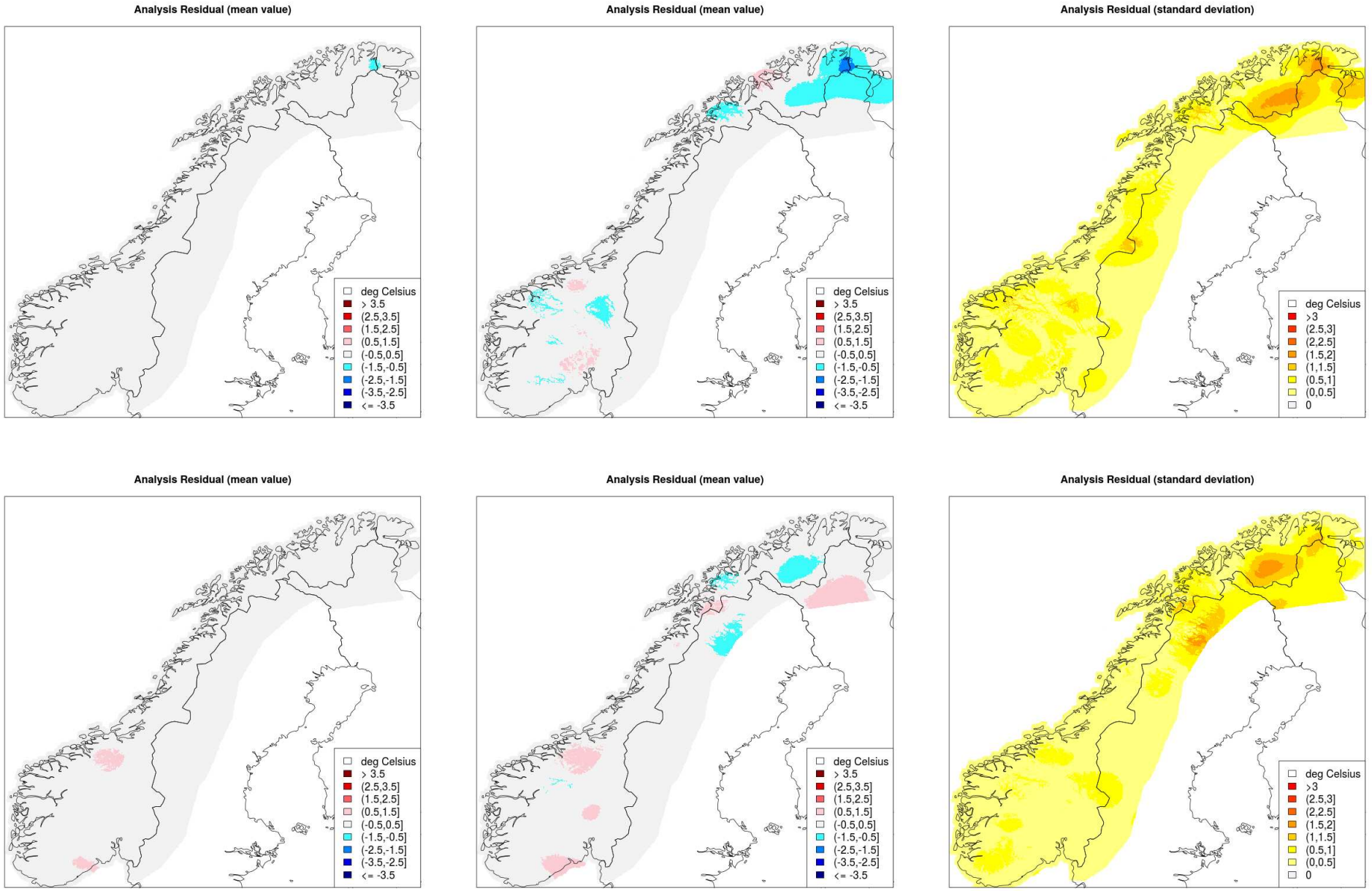

Figure 50: *TEMP1d24h* analysis increment. (top-left) annual mean field for year 2011; (top-central) mean field for January-February-December 2011; (top-right) standard deviation field for January-February-December 2011. (bottom-left) annual mean field for year 2015; (bottom-central) mean field for January-February-December 2015; (bottom-right) standard deviation field for January-February-December 2015.

guarantees the quality of analysis products in real-time applications especially.

In the future, the uncertainties in the analysis should be reduced through an objective estimation of the OI parameters, which at the moment are estimated with an heuristic procedure. Analogously, the spatial consistency test thresholds should be estimated in an objective way instead of the current trial-and-fail procedure. Furthermore, possible substantial improvements are the inclusion of non-euclidean distances in the computations of OI error covariance matrices and the use of numerical atmospheric model fields as background.

A

Appendix: Examples of regional pseudo-background

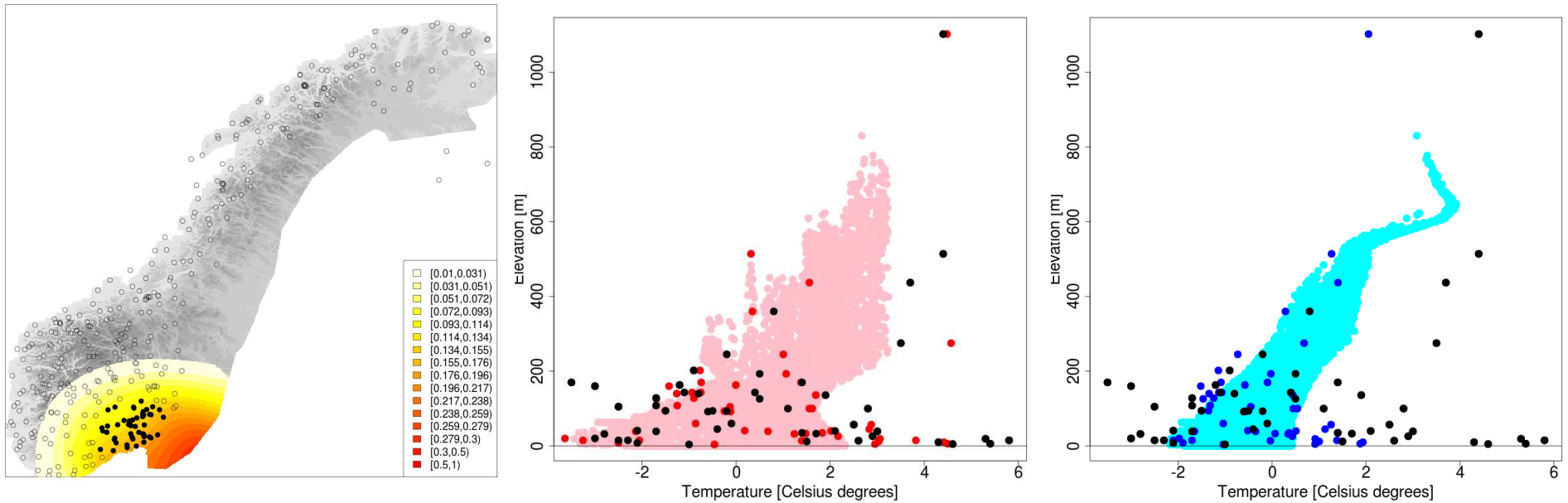

Figure 51: Test case 2015/01/01. *TEMP1d* construction of the pseudo-background. Left panel: station distribution (circles); Y_d stations included in the sub-domain (black dots); $\mathbf{x}^{Y_d,\mathrm{IDI}} / \sum_{d=1}^{D} \mathbf{x}^{Y_d,\mathrm{IDI}}$ (shaded). Central panel: regional pseudo-background temperature vs Elevation a.m.s.l.: observed values (black dots); $\mathbf{y}_d^{\mathrm{b}}$ (red dots); $\mathbf{x}_d^{\mathrm{b}}$ (pink dots, only the 1% grid points more influenced by the Y_d stations are shown). Right panel: blended pseudo-background temperature vs Elevation a.m.s.l.: observed values (black dots); $\mathbf{y}^{\mathrm{b}}$ (blue dots); $\mathbf{x}^{\mathrm{b}}$ (cyan dots, only the 1% grid points more influenced by the Y_d stations are shown)

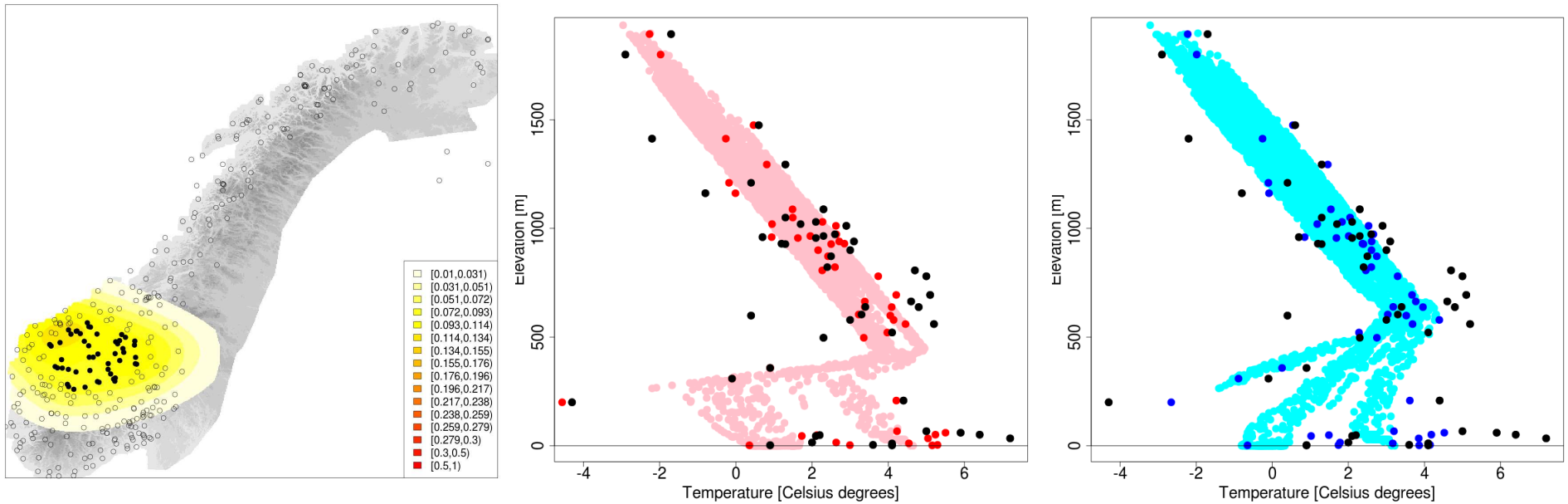

Figure 52: Test case 2015/01/01. *TEMP1d* construction of the pseudo-background. Left panel: station distribution (circles); Y_d stations included in the sub-domain (black dots); $\mathbf{x}^{Y_d,\mathrm{IDI}} / \sum_{d=1}^{D} \mathbf{x}^{Y_d,\mathrm{IDI}}$ (shaded). Central panel: regional pseudo-background temperature vs Elevation a.m.s.l.: observed values (black dots); $\mathbf{y}_d^{\mathrm{b}}$ (red dots); $\mathbf{x}_d^{\mathrm{b}}$ (pink dots, only the 1% grid points more influenced by the Y_d stations are shown). Right panel: blended pseudo-background temperature vs Elevation a.m.s.l.: observed values (black dots); $\mathbf{y}^{\mathrm{b}}$ (blue dots); $\mathbf{x}^{\mathrm{b}}$ (cyan dots, only the 1% grid points more influenced by the Y_d stations are shown)

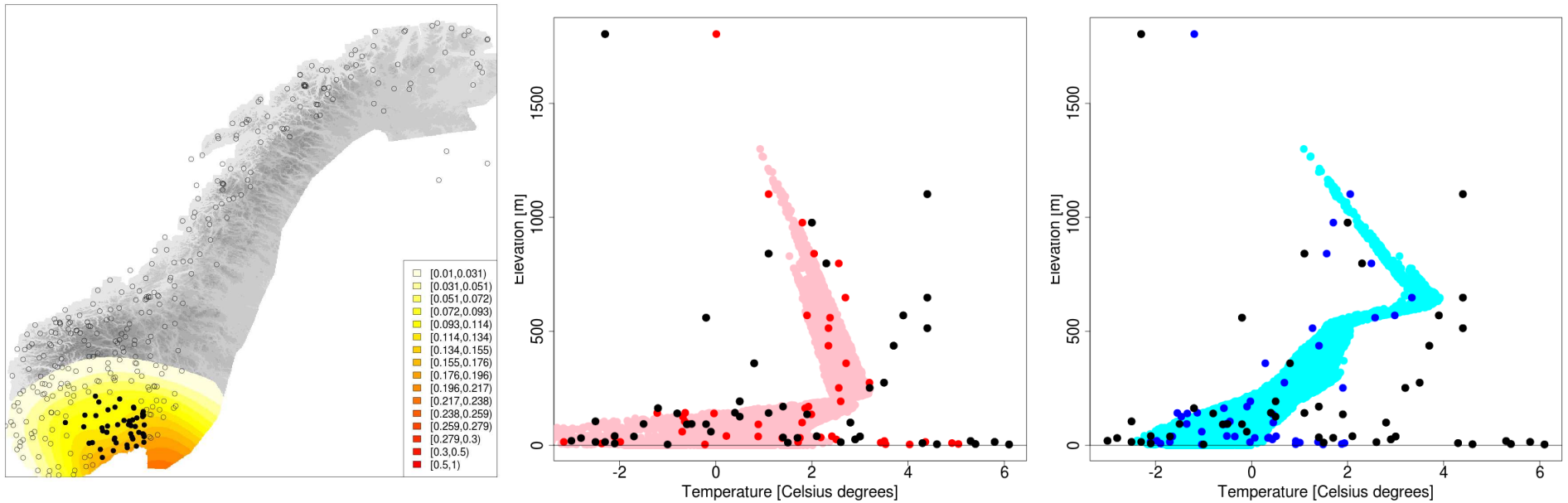

Figure 53: Test case 2015/01/01. *TEMP1d* construction of the pseudo-background. Left panel: station distribution (circles); Y_d stations included in the sub-domain (black dots); $\mathbf{x}^{Y_d,\mathrm{IDI}} / \sum_{d=1}^{D} \mathbf{x}^{Y_d,\mathrm{IDI}}$ (shaded). Central panel: regional pseudo-background temperature vs Elevation a.m.s.l.: observed values (black dots); $\mathbf{y}_d^{\mathrm{b}}$ (red dots); $\mathbf{x}_d^{\mathrm{b}}$ (pink dots, only the 1% grid points more influenced by the Y_d stations are shown). Right panel: blended pseudo-background temperature vs Elevation a.m.s.l.: observed values (black dots); $\mathbf{y}^{\mathrm{b}}$ (blue dots); $\mathbf{x}^{\mathrm{b}}$ (cyan dots, only the 1% grid points more influenced by the Y_d stations are shown)

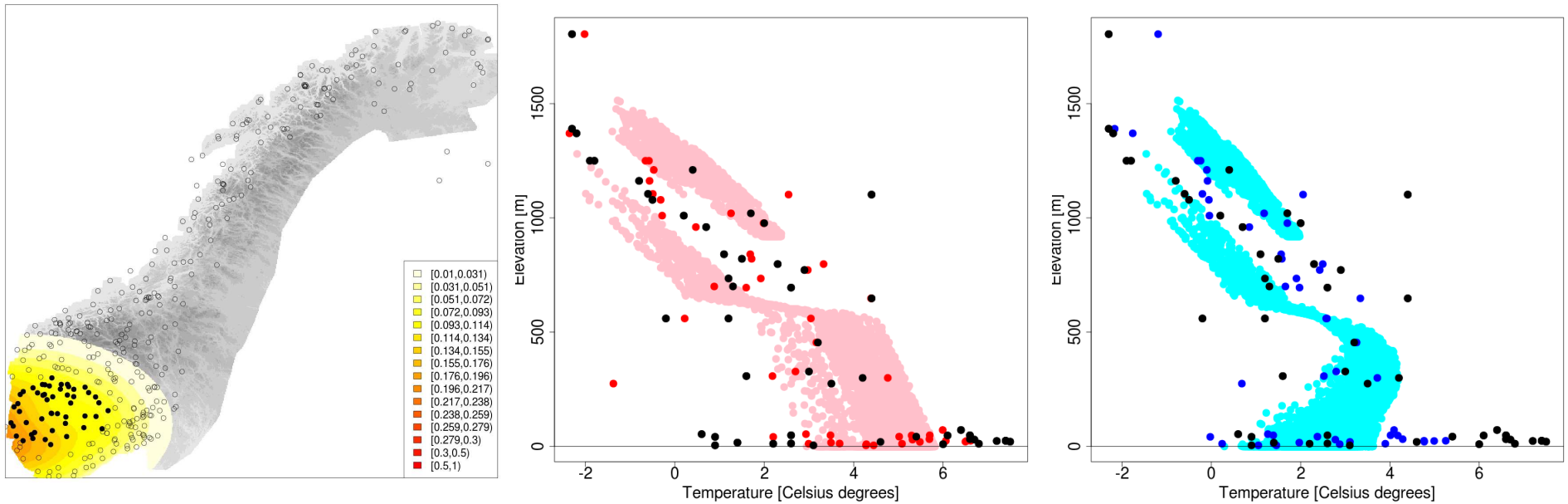

Figure 54: Test case 2015/01/01. *TEMP1d* construction of the pseudo-background. Left panel: station distribution (circles); Y_d stations included in the sub-domain (black dots); $\mathbf{x}^{Y_d,\mathrm{IDI}} / \sum_{d=1}^{D} \mathbf{x}^{Y_d,\mathrm{IDI}}$ (shaded). Central panel: regional pseudo-background temperature vs Elevation a.m.s.l.: observed values (black dots); $\mathbf{y}_d^{\mathrm{b}}$ (red dots); $\mathbf{x}_d^{\mathrm{b}}$ (pink dots, only the 1% grid points more influenced by the Y_d stations are shown). Right panel: blended pseudo-background temperature vs Elevation a.m.s.l.: observed values (black dots); $\mathbf{y}^{\mathrm{b}}$ (blue dots); $\mathbf{x}^{\mathrm{b}}$ (cyan dots, only the 1% grid points more influenced by the Y_d stations are shown)

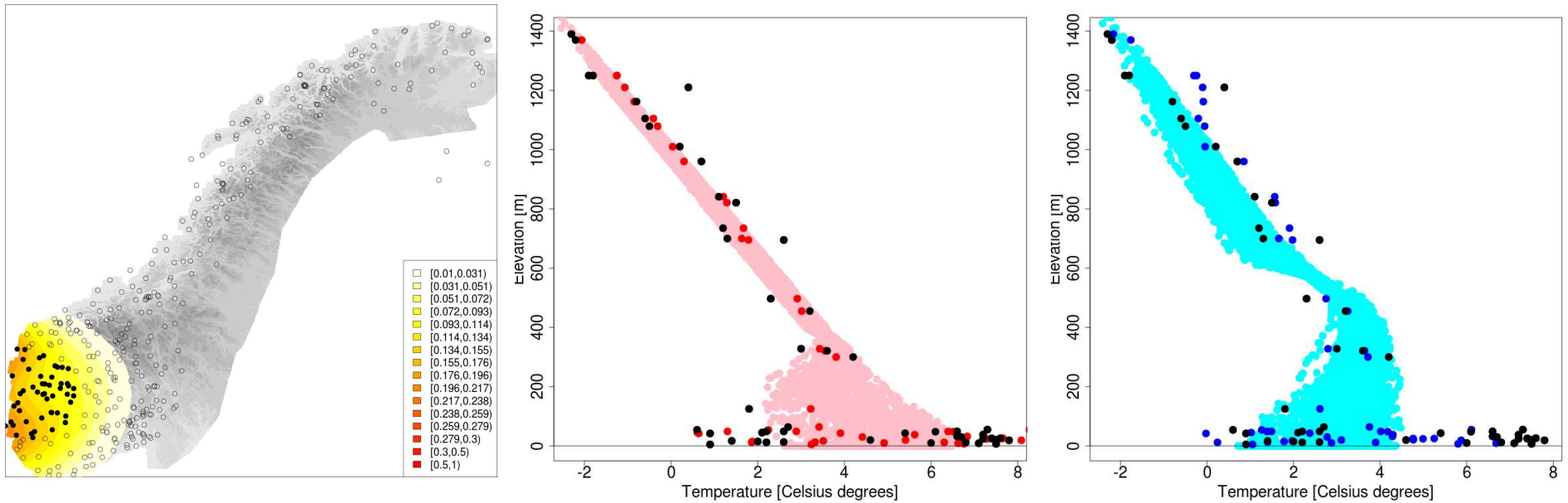

Figure 55: Test case 2015/01/01. *TEMP1d* construction of the pseudo-background. Left panel: station distribution (circles); Y_d stations included in the sub-domain (black dots); $\mathbf{x}^{Y_d,\mathrm{IDI}} / \sum_{d=1}^{D} \mathbf{x}^{Y_d,\mathrm{IDI}}$ (shaded). Central panel: regional pseudo-background temperature vs Elevation a.m.s.l.: observed values (black dots); $\mathbf{y}_d^{\mathrm{b}}$ (red dots); $\mathbf{x}_d^{\mathrm{b}}$ (pink dots, only the 1% grid points more influenced by the Y_d stations are shown). Right panel: blended pseudo-background temperature vs Elevation a.m.s.l.: observed values (black dots); $\mathbf{y}^{\mathrm{b}}$ (blue dots); $\mathbf{x}^{\mathrm{b}}$ (cyan dots, only the 1% grid points more influenced by the Y_d stations are shown)

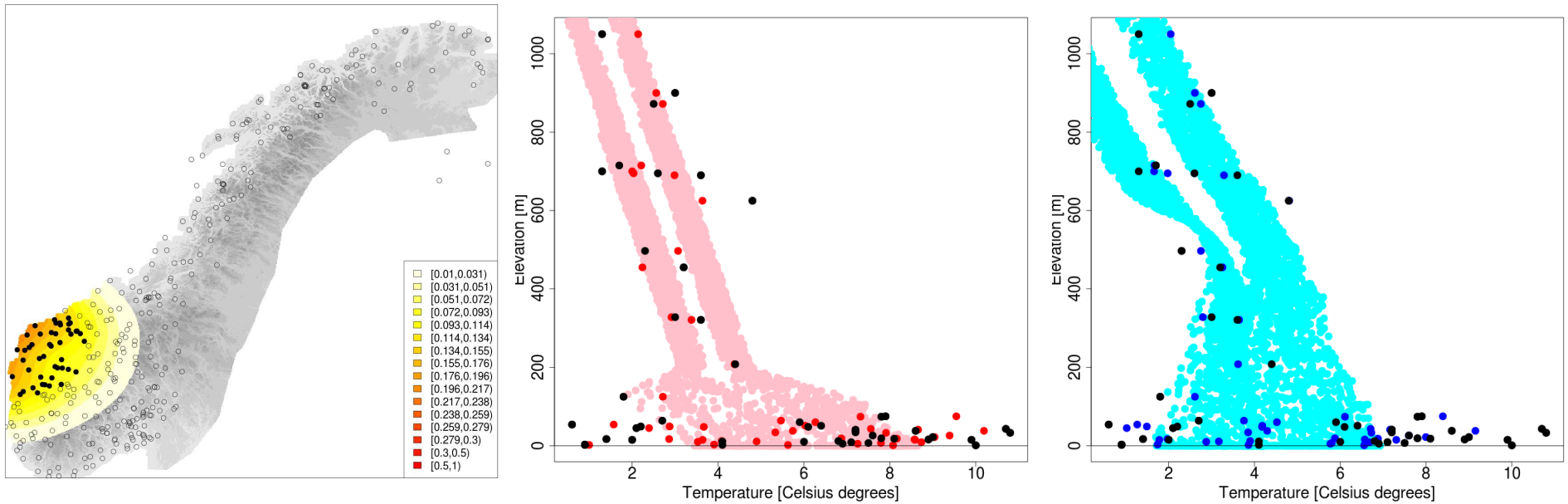

Figure 56: Test case 2015/01/01. *TEMP1d* construction of the pseudo-background. Left panel: station distribution (circles); Y_d stations included in the sub-domain (black dots); $\mathbf{x}^{Y_d,\mathrm{IDI}} / \sum_{d=1}^{D} \mathbf{x}^{Y_d,\mathrm{IDI}}$ (shaded). Central panel: regional pseudo-background temperature vs Elevation a.m.s.l.: observed values (black dots); $\mathbf{y}_d^{\mathrm{b}}$ (red dots); $\mathbf{x}_d^{\mathrm{b}}$ (pink dots, only the 1% grid points more influenced by the Y_d stations are shown). Right panel: blended pseudo-background temperature vs Elevation a.m.s.l.: observed values (black dots); $\mathbf{y}^{\mathrm{b}}$ (blue dots); $\mathbf{x}^{\mathrm{b}}$ (cyan dots, only the 1% grid points more influenced by the Y_d stations are shown)

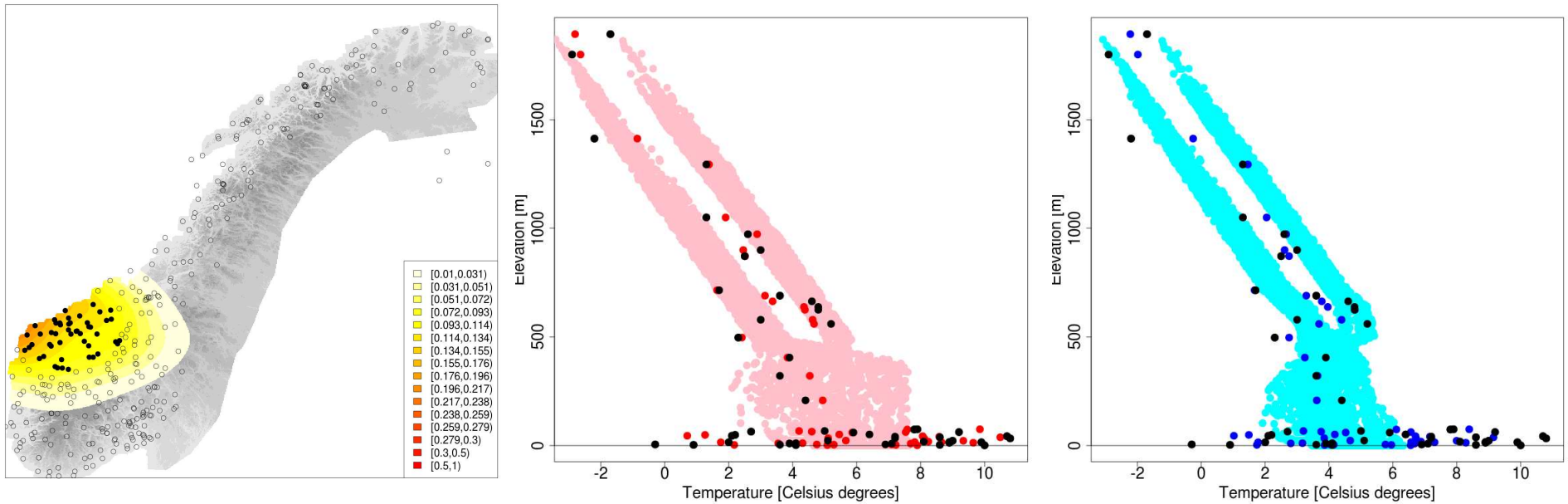

Figure 57: Test case 2015/01/01. *TEMP1d* construction of the pseudo-background. Left panel: station distribution (circles); Y_d stations included in the sub-domain (black dots); $\mathbf{x}^{Y_d,\mathrm{IDI}} / \sum_{d=1}^{D} \mathbf{x}^{Y_d,\mathrm{IDI}}$ (shaded). Central panel: regional pseudo-background temperature vs Elevation a.m.s.l.: observed values (black dots); $\mathbf{y}_d^{\mathrm{b}}$ (red dots); $\mathbf{x}_d^{\mathrm{b}}$ (pink dots, only the 1% grid points more influenced by the Y_d stations are shown). Right panel: blended pseudo-background temperature vs Elevation a.m.s.l.: observed values (black dots); $\mathbf{y}^{\mathrm{b}}$ (blue dots); $\mathbf{x}^{\mathrm{b}}$ (cyan dots, only the 1% grid points more influenced by the Y_d stations are shown)

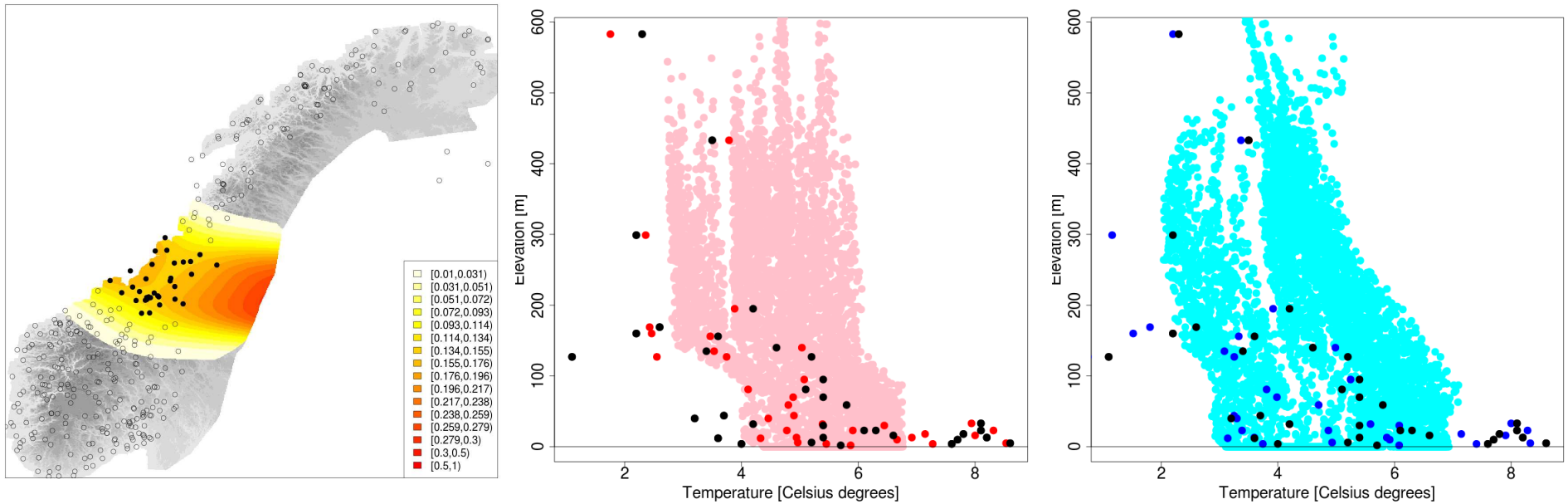

Figure 58: Test case 2015/01/01. *TEMP1d* construction of the pseudo-background. Left panel: station distribution (circles); Y_d stations included in the sub-domain (black dots); $\mathbf{x}^{Y_d,\mathrm{IDI}} / \sum_{d=1}^{D} \mathbf{x}^{Y_d,\mathrm{IDI}}$ (shaded). Central panel: regional pseudo-background temperature vs Elevation a.m.s.l.: observed values (black dots); $\mathbf{y}_d^{\mathrm{b}}$ (red dots); $\mathbf{x}_d^{\mathrm{b}}$ (pink dots, only the 1% grid points more influenced by the Y_d stations are shown). Right panel: blended pseudo-background temperature vs Elevation a.m.s.l.: observed values (black dots); $\mathbf{y}^{\mathrm{b}}$ (blue dots); $\mathbf{x}^{\mathrm{b}}$ (cyan dots, only the 1% grid points more influenced by the Y_d stations are shown)

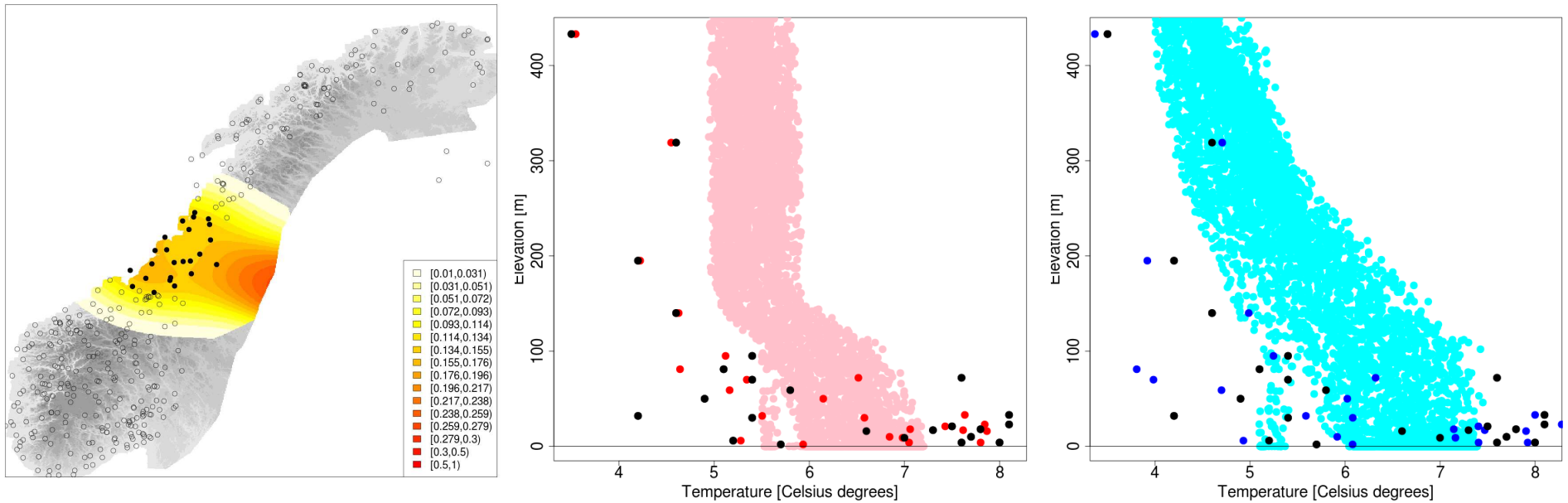

Figure 59: Test case 2015/01/01. *TEMP1d* construction of the pseudo-background. Left panel: station distribution (circles); Y_d stations included in the sub-domain (black dots); $\mathbf{x}^{Y_d,\mathrm{IDI}} / \sum_{d=1}^{D} \mathbf{x}^{Y_d,\mathrm{IDI}}$ (shaded). Central panel: regional pseudo-background temperature vs Elevation a.m.s.l.: observed values (black dots); $\mathbf{y}_d^{\mathrm{b}}$ (red dots); $\mathbf{x}_d^{\mathrm{b}}$ (pink dots, only the 1% grid points more influenced by the Y_d stations are shown). Right panel: blended pseudo-background temperature vs Elevation a.m.s.l.: observed values (black dots); $\mathbf{y}^{\mathrm{b}}$ (blue dots); $\mathbf{x}^{\mathrm{b}}$ (cyan dots, only the 1% grid points more influenced by the Y_d stations are shown)

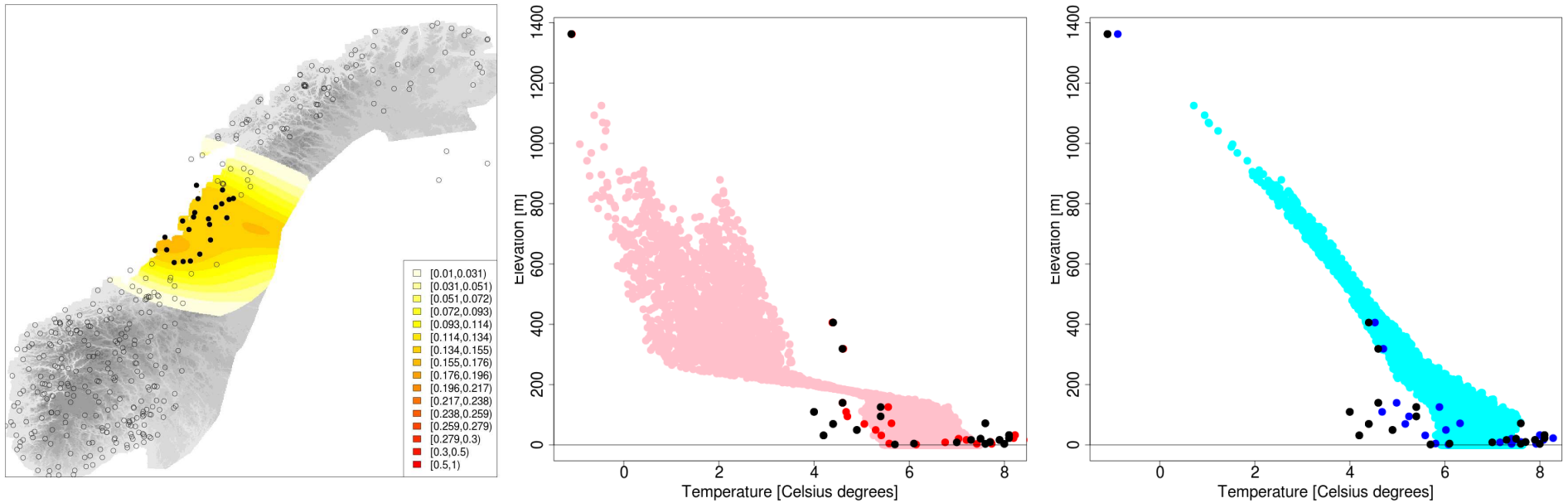

Figure 60: Test case 2015/01/01. *TEMP1d* construction of the pseudo-background. Left panel: station distribution (circles); Y_d stations included in the sub-domain (black dots); $\mathbf{x}^{Y_d,\mathrm{IDI}} / \sum_{d=1}^{D} \mathbf{x}^{Y_d,\mathrm{IDI}}$ (shaded). Central panel: regional pseudo-background temperature vs Elevation a.m.s.l.: observed values (black dots); $\mathbf{y}_d^{\mathrm{b}}$ (red dots); $\mathbf{x}_d^{\mathrm{b}}$ (pink dots, only the 1% grid points more influenced by the Y_d stations are shown). Right panel: blended pseudo-background temperature vs Elevation a.m.s.l.: observed values (black dots); $\mathbf{y}^{\mathrm{b}}$ (blue dots); $\mathbf{x}^{\mathrm{b}}$ (cyan dots, only the 1% grid points more influenced by the Y_d stations are shown)

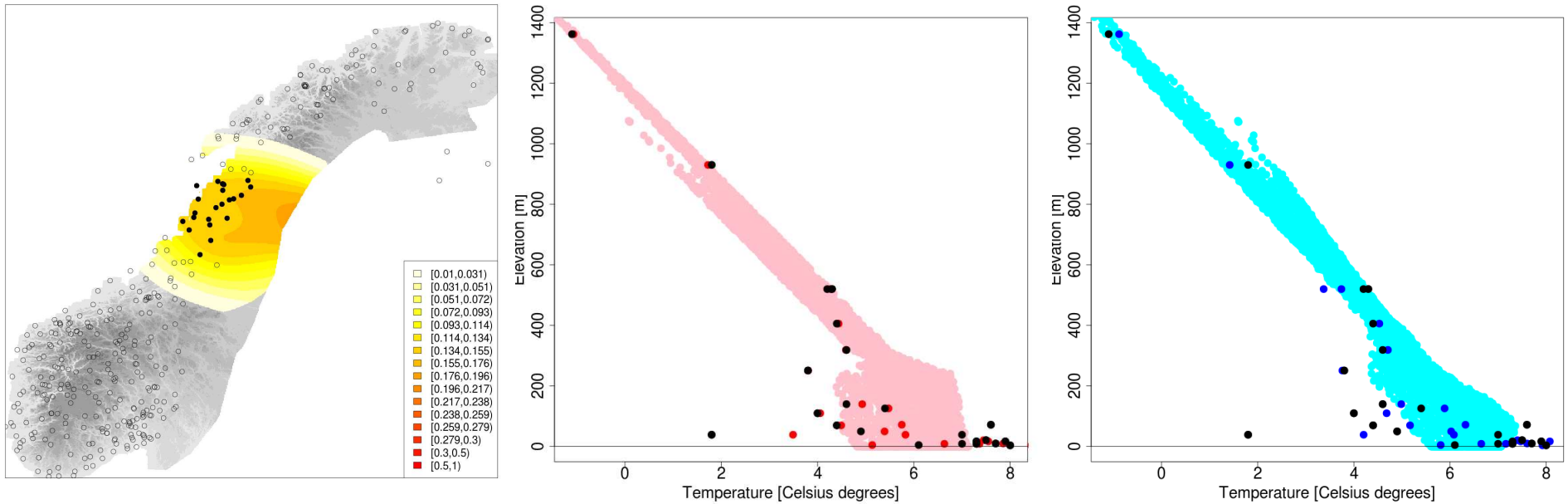

Figure 61: Test case 2015/01/01. *TEMP1d* construction of the pseudo-background. Left panel: station distribution (circles); Y_d stations included in the sub-domain (black dots); $\mathbf{x}^{Y_d,\mathrm{IDI}} / \sum_{d=1}^{D} \mathbf{x}^{Y_d,\mathrm{IDI}}$ (shaded). Central panel: regional pseudo-background temperature vs Elevation a.m.s.l.: observed values (black dots); $\mathbf{y}_d^{\mathrm{b}}$ (red dots); $\mathbf{x}_d^{\mathrm{b}}$ (pink dots, only the 1% grid points more influenced by the Y_d stations are shown). Right panel: blended pseudo-background temperature vs Elevation a.m.s.l.: observed values (black dots); $\mathbf{y}^{\mathrm{b}}$ (blue dots); $\mathbf{x}^{\mathrm{b}}$ (cyan dots, only the 1% grid points more influenced by the Y_d stations are shown)

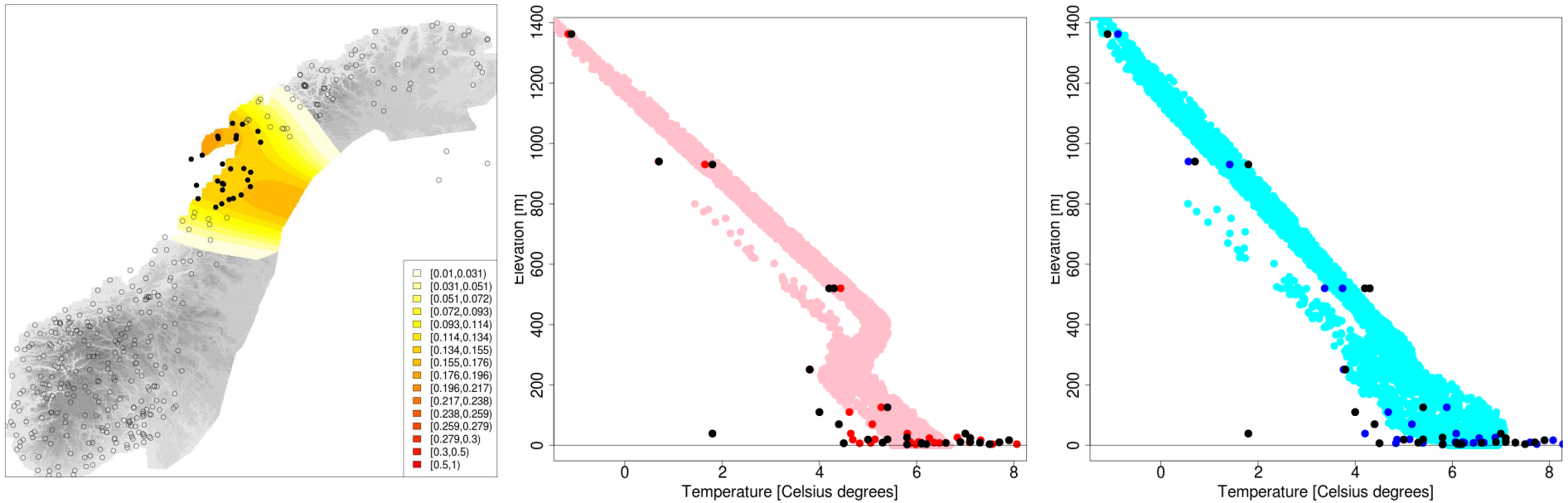

Figure 62: Test case 2015/01/01. *TEMP1d* construction of the pseudo-background. Left panel: station distribution (circles); Y_d stations included in the sub-domain (black dots); $\mathbf{x}^{Y_d,\mathrm{IDI}} / \sum_{d=1}^{D} \mathbf{x}^{Y_d,\mathrm{IDI}}$ (shaded). Central panel: regional pseudo-background temperature vs Elevation a.m.s.l.: observed values (black dots); $\mathbf{y}_d^{\mathrm{b}}$ (red dots); $\mathbf{x}_d^{\mathrm{b}}$ (pink dots, only the 1% grid points more influenced by the Y_d stations are shown). Right panel: blended pseudo-background temperature vs Elevation a.m.s.l.: observed values (black dots); $\mathbf{y}^{\mathrm{b}}$ (blue dots); $\mathbf{x}^{\mathrm{b}}$ (cyan dots, only the 1% grid points more influenced by the Y_d stations are shown)

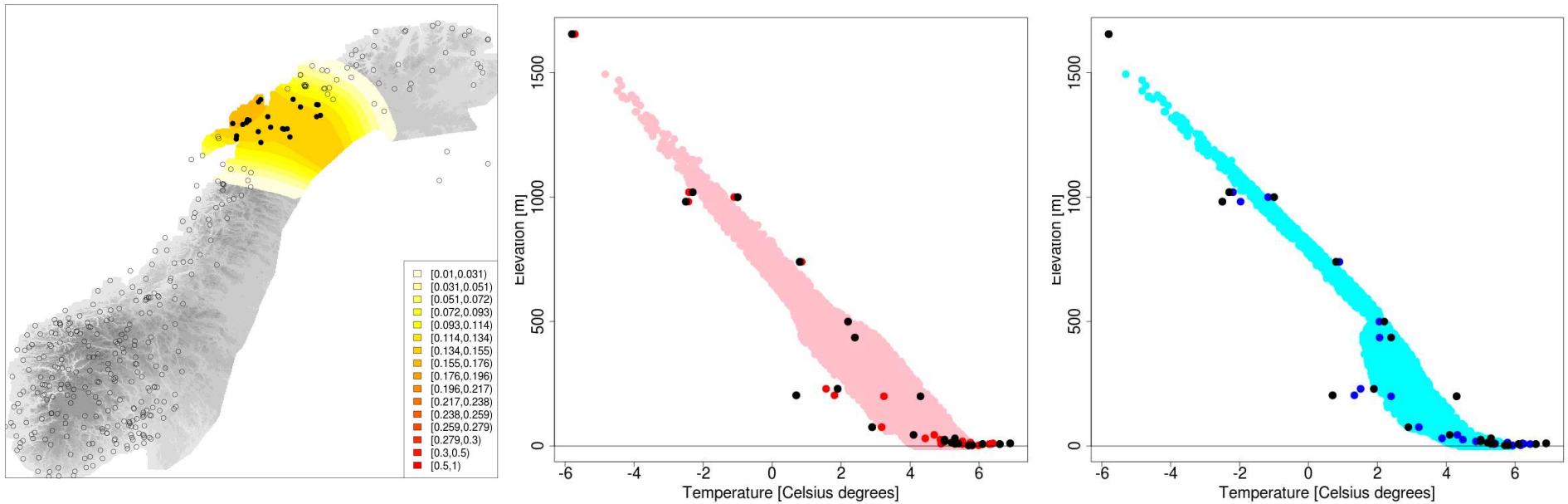

Figure 63: Test case 2015/01/01. *TEMP1d* construction of the pseudo-background. Left panel: station distribution (circles); Y_d stations included in the sub-domain (black dots); $\mathbf{x}^{Y_d,\mathrm{IDI}} / \sum_{d=1}^{D} \mathbf{x}^{Y_d,\mathrm{IDI}}$ (shaded). Central panel: regional pseudo-background temperature vs Elevation a.m.s.l.: observed values (black dots); $\mathbf{y}_d^{\mathrm{b}}$ (red dots); $\mathbf{x}_d^{\mathrm{b}}$ (pink dots, only the 1% grid points more influenced by the Y_d stations are shown). Right panel: blended pseudo-background temperature vs Elevation a.m.s.l.: observed values (black dots); $\mathbf{y}^{\mathrm{b}}$ (blue dots); $\mathbf{x}^{\mathrm{b}}$ (cyan dots, only the 1% grid points more influenced by the Y_d stations are shown)

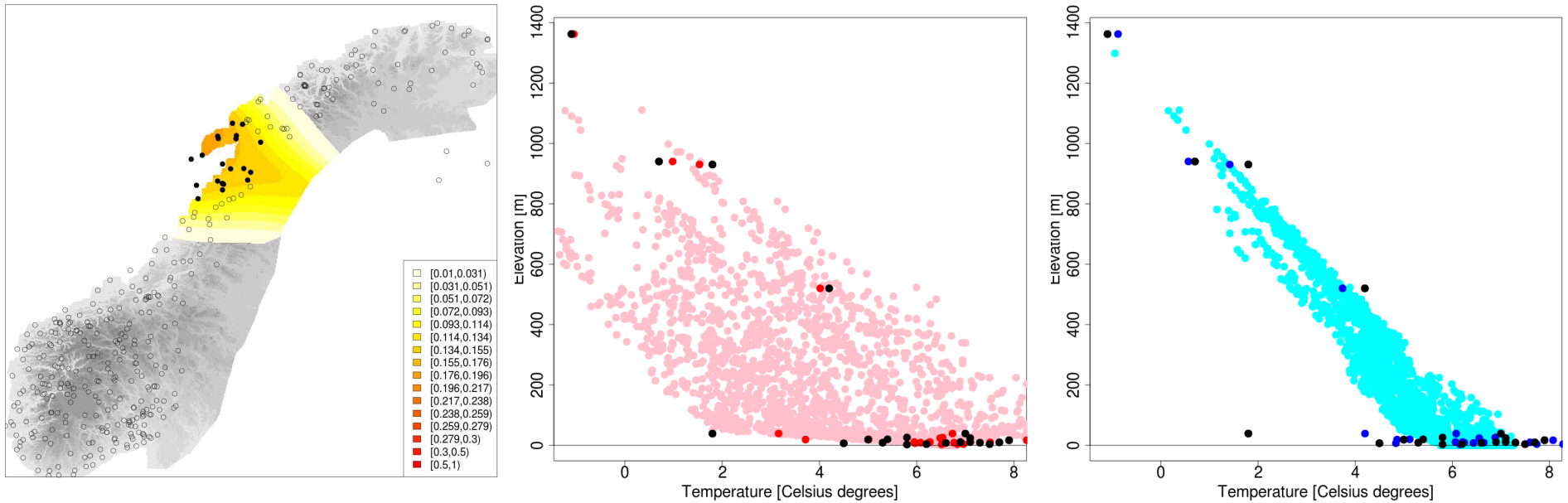

Figure 64: Test case 2015/01/01. *TEMP1d* construction of the pseudo-background. Left panel: station distribution (circles); Y_d stations included in the sub-domain (black dots); $\mathbf{x}^{Y_d,\mathrm{IDI}} / \sum_{d=1}^{D} \mathbf{x}^{Y_d,\mathrm{IDI}}$ (shaded). Central panel: regional pseudo-background temperature vs Elevation a.m.s.l.: observed values (black dots); $\mathbf{y}_d^{\mathrm{b}}$ (red dots); $\mathbf{x}_d^{\mathrm{b}}$ (pink dots, only the 1% grid points more influenced by the Y_d stations are shown). Right panel: blended pseudo-background temperature vs Elevation a.m.s.l.: observed values (black dots); $\mathbf{y}^{\mathrm{b}}$ (blue dots); $\mathbf{x}^{\mathrm{b}}$ (cyan dots, only the 1% grid points more influenced by the Y_d stations are shown)

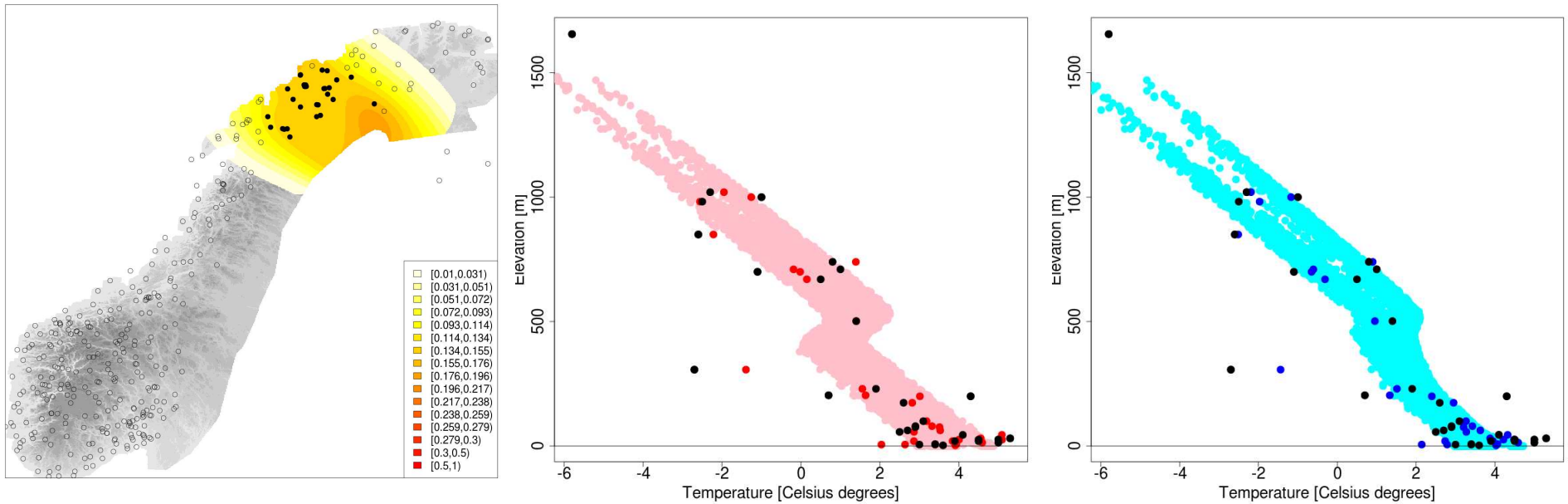

Figure 65: Test case 2015/01/01. *TEMP1d* construction of the pseudo-background. Left panel: station distribution (circles); Y_d stations included in the sub-domain (black dots); $\mathbf{x}^{Y_d,\mathrm{IDI}} / \sum_{d=1}^{D} \mathbf{x}^{Y_d,\mathrm{IDI}}$ (shaded). Central panel: regional pseudo-background temperature vs Elevation a.m.s.l.: observed values (black dots); $\mathbf{y}_d^{\mathrm{b}}$ (red dots); $\mathbf{x}_d^{\mathrm{b}}$ (pink dots, only the 1% grid points more influenced by the Y_d stations are shown). Right panel: blended pseudo-background temperature vs Elevation a.m.s.l.: observed values (black dots); $\mathbf{y}^{\mathrm{b}}$ (blue dots); $\mathbf{x}^{\mathrm{b}}$ (cyan dots, only the 1% grid points more influenced by the Y_d stations are shown)

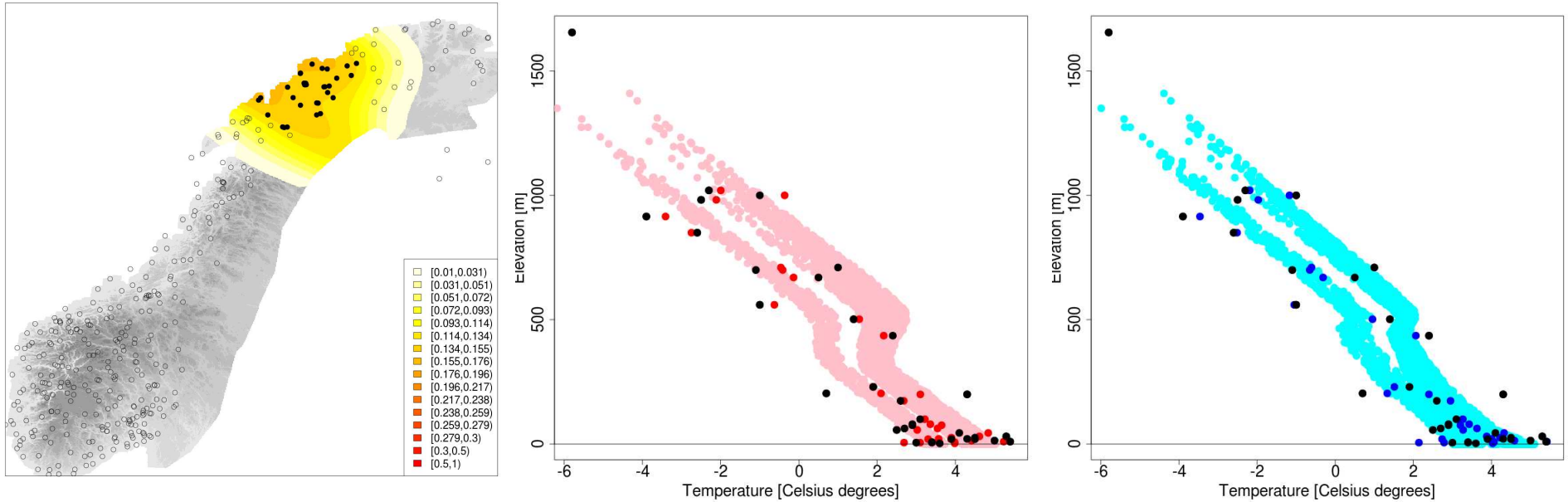

Figure 66: Test case 2015/01/01. *TEMP1d* construction of the pseudo-background. Left panel: station distribution (circles); Y_d stations included in the sub-domain (black dots); $\mathbf{x}^{Y_d,\mathrm{IDI}} / \sum_{d=1}^{D} \mathbf{x}^{Y_d,\mathrm{IDI}}$ (shaded). Central panel: regional pseudo-background temperature vs Elevation a.m.s.l.: observed values (black dots); $\mathbf{y}_d^{\mathrm{b}}$ (red dots); $\mathbf{x}_d^{\mathrm{b}}$ (pink dots, only the 1% grid points more influenced by the Y_d stations are shown). Right panel: blended pseudo-background temperature vs Elevation a.m.s.l.: observed values (black dots); $\mathbf{y}^{\mathrm{b}}$ (blue dots); $\mathbf{x}^{\mathrm{b}}$ (cyan dots, only the 1% grid points more influenced by the Y_d stations are shown)

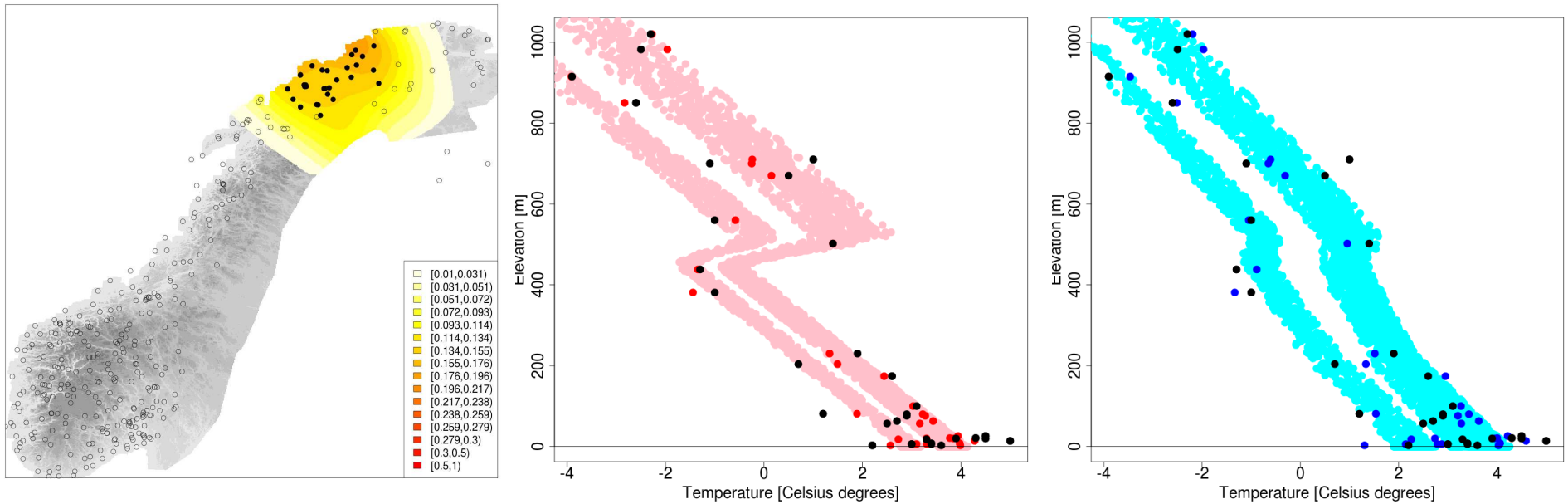

Figure 67: Test case 2015/01/01. *TEMP1d* construction of the pseudo-background. Left panel: station distribution (circles); Y_d stations included in the sub-domain (black dots); $\mathbf{x}^{Y_d,\mathrm{IDI}} / \sum_{d=1}^{D} \mathbf{x}^{Y_d,\mathrm{IDI}}$ (shaded). Central panel: regional pseudo-background temperature vs Elevation a.m.s.l.: observed values (black dots); $\mathbf{y}_d^{\mathrm{b}}$ (red dots); $\mathbf{x}_d^{\mathrm{b}}$ (pink dots, only the 1% grid points more influenced by the Y_d stations are shown). Right panel: blended pseudo-background temperature vs Elevation a.m.s.l.: observed values (black dots); $\mathbf{y}^{\mathrm{b}}$ (blue dots); $\mathbf{x}^{\mathrm{b}}$ (cyan dots, only the 1% grid points more influenced by the Y_d stations are shown)

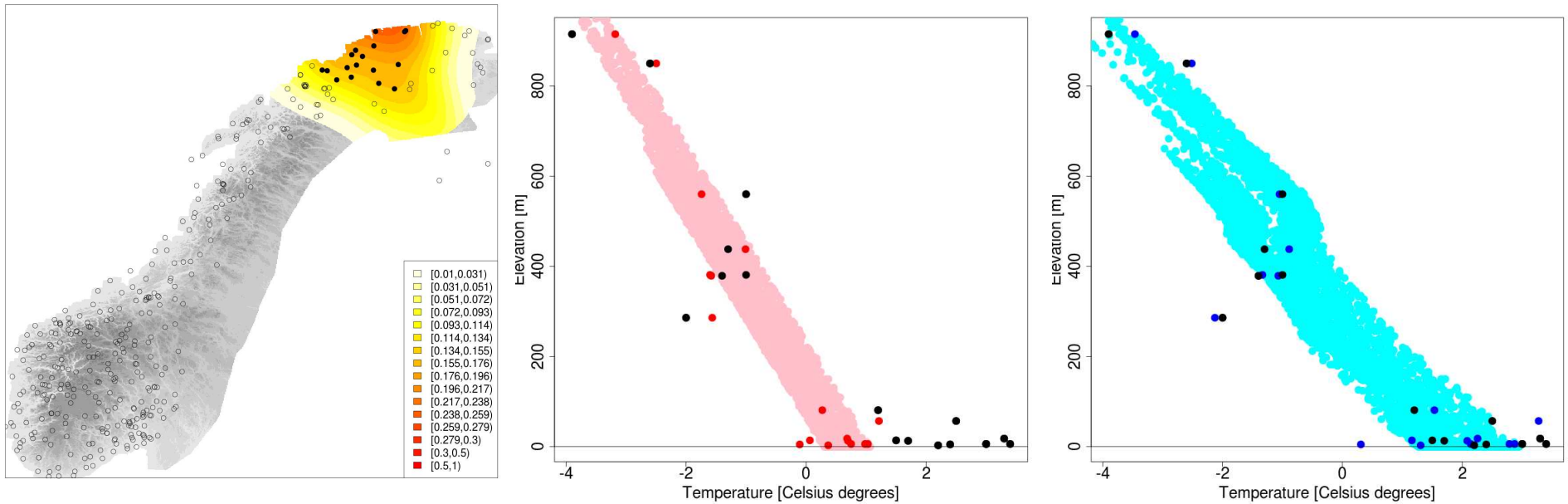

Figure 68: Test case 2015/01/01. *TEMP1d* construction of the pseudo-background. Left panel: station distribution (circles); Y_d stations included in the sub-domain (black dots); $\mathbf{x}^{Y_d,\mathrm{IDI}} / \sum_{d=1}^{D} \mathbf{x}^{Y_d,\mathrm{IDI}}$ (shaded). Central panel: regional pseudo-background temperature vs Elevation a.m.s.l.: observed values (black dots); $\mathbf{y}_d^{\mathrm{b}}$ (red dots); $\mathbf{x}_d^{\mathrm{b}}$ (pink dots, only the 1% grid points more influenced by the Y_d stations are shown). Right panel: blended pseudo-background temperature vs Elevation a.m.s.l.: observed values (black dots); $\mathbf{y}^{\mathrm{b}}$ (blue dots); $\mathbf{x}^{\mathrm{b}}$ (cyan dots, only the 1% grid points more influenced by the Y_d stations are shown)

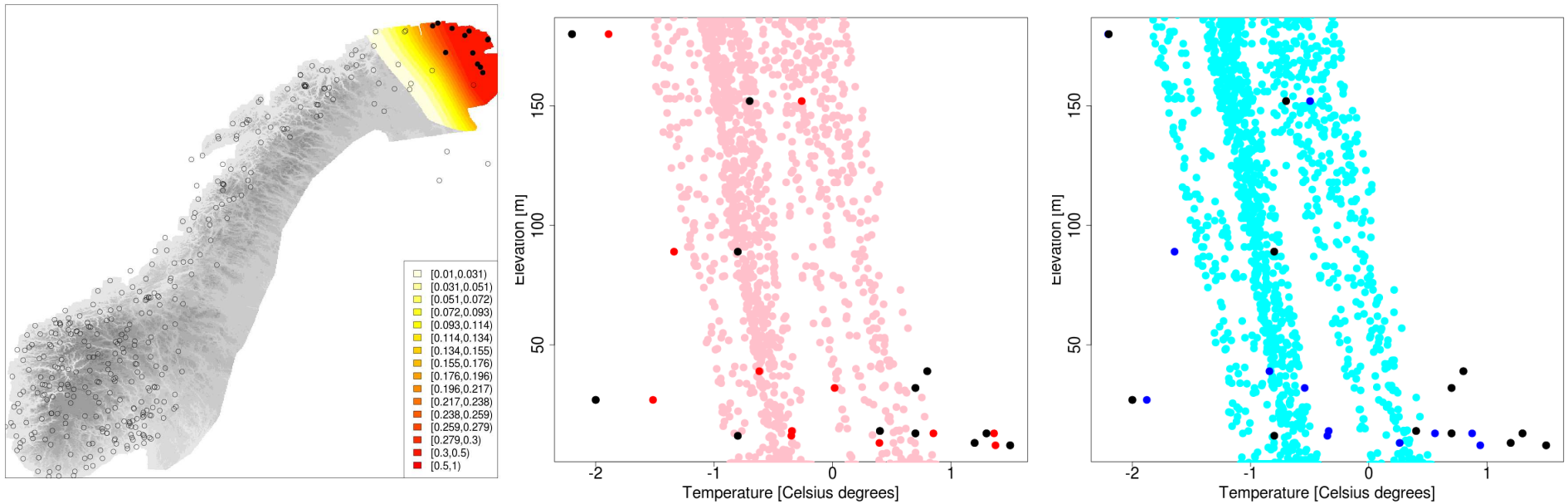

Figure 69: Test case 2015/01/01. *TEMP1d* construction of the pseudo-background. Left panel: station distribution (circles); Y_d stations included in the sub-domain (black dots); $\mathbf{x}^{Y_d,\mathrm{IDI}} / \sum_{d=1}^{D} \mathbf{x}^{Y_d,\mathrm{IDI}}$ (shaded). Central panel: regional pseudo-background temperature vs Elevation a.m.s.l.: observed values (black dots); $\mathbf{y}_d^{\mathrm{b}}$ (red dots); $\mathbf{x}_d^{\mathrm{b}}$ (pink dots, only the 1% grid points more influenced by the Y_d stations are shown). Right panel: blended pseudo-background temperature vs Elevation a.m.s.l.: observed values (black dots); $\mathbf{y}^{\mathrm{b}}$ (blue dots); $\mathbf{x}^{\mathrm{b}}$ (cyan dots, only the 1% grid points more influenced by the Y_d stations are shown)

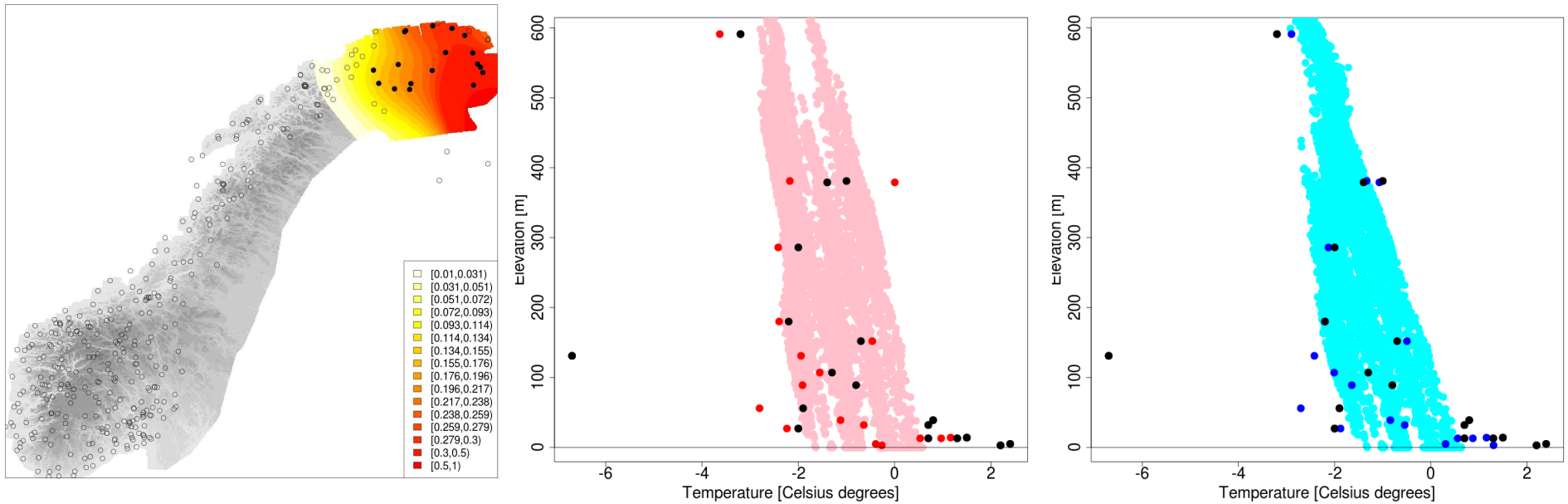

Figure 70: Test case 2015/01/01. *TEMP1d* construction of the pseudo-background. Left panel: station distribution (circles); Y_d stations included in the sub-domain (black dots); $\mathbf{x}^{Y_d,\mathrm{IDI}} / \sum_{d=1}^{D} \mathbf{x}^{Y_d,\mathrm{IDI}}$ (shaded). Central panel: regional pseudo-background temperature vs Elevation a.m.s.l.: observed values (black dots); $\mathbf{y}_d^{\mathrm{b}}$ (red dots); $\mathbf{x}_d^{\mathrm{b}}$ (pink dots, only the 1% grid points more influenced by the Y_d stations are shown). Right panel: blended pseudo-background temperature vs Elevation a.m.s.l.: observed values (black dots); $\mathbf{y}^{\mathrm{b}}$ (blue dots); $\mathbf{x}^{\mathrm{b}}$ (cyan dots, only the 1% grid points more influenced by the Y_d stations are shown)

References

Frei, C. (2014), Interpolation of temperature in a mountainous region using nonlinear profiles and non-euclidean distances, *International Journal of Climatology*, *34*(5), 1585–1605.

Gandin, L. S., and R. Hardin (1965), *Objective analysis of meteorological fields*, vol. 242, Israel program for scientific translations Jerusalem.

Ide, K., P. Courtier, M. Ghil, and A. Lorenc (1997), Unified notation for data assimilation: operational, sequential and variational, *Practice*, *75*(1B), 181–189.

Jazwinski, A. H. (2007), *Stochastic processes and filtering theory*, Courier Dover Publications.

Lussana, C., F. Uboldi, and M. R. Salvati (2010), A spatial consistency test for surface observations from mesoscale meteorological networks, *Quarterly Journal of the Royal Meteorological Society*, *136*(649), 1075–1088.

Mohr, M. (2008), New routines for gridding of temperature and precipitation observations for "senorge. no", *Met. no Report*, *8*, 2008.

Parrish, D., and J. Derber (1992), The national meteorological centre's spectral statistical-interpolation analysis system, *Mon. Weather Rev.*, *120*, 1747–1763.

Tveito, O., E. Førland, R. Heino, I. Hanssen-Bauer, H. Alexandersson, B. Dahlström, A. Drebs, C. Kern-Hansen, T. Jónsson, E. Vaarby Laursen, et al. (2000), Nordic temperature maps, *DNMI report*, *9*(00).

Tveito, O. E., and E. J. Førland (1999), Mapping temperatures in norway applying terrain information, geostatistics and gis, *Norsk Geografisk Tidsskrift-Norwegian Journal of Geography*, *53*(4), 202–212.

Uboldi, F., C. Lussana, and M. Salvati (2008), Three-dimensional spatial interpolation of surface meteorological observations from high-resolution local networks, *Meteorological Applications*, *15*(3), 331–345.